

Utrecht University and ETH Zürich

Partial melting and localisation as functions of composition and strain rate in metapelites

MSc Thesis

Tessa Sophia van der Voort

Bsc. University of Utrecht, Earth Sciences, 2011

30/05/2013

University of Utrecht, MSc program Earth, Structure and Dynamics.

ETH

Eidgenössische Technische Hochschule Zürich
Swiss Federal Institute of Technology Zurich



Universiteit Utrecht

Abstract

The understanding of deformation-induced partial melting and localisation in metapelitic rocks is of importance for the mechanical behaviour and chemical differentiation of the continental crust. Regions of intense deformation and shear localisation are the major sources of melt in the crust. The process of partial melting is directly related to shear localisation and migration pathways for the melt. Existing experimental studies have not fully established the dependence of several main factors that may have a large impact on localisation. In this study the focus will lie on the effect of (1) composition, (2) strain rate and (3) finite strain on melting and localisation in sheared metapelites. This creates a larger framework for and a better understanding of deformation-induced features in metapelites. These features have been studied by deforming samples in a high pressure and temperature tri-axial torsion apparatus. The quartz-content is respectively positively and twice negatively dependent on shear strength, localisation and melt production. Rate-strengthening viscous creep occurred: indicating a strong dependence of localisation on strain rate. Deformation accommodation behaviour was found to change radically with increased finite strain. Weakening occurred mostly because of the increase of available gliding planes with increased strain. A novel approach with the FIB-SEM analysis was used to establish the 3D structure of melt zones. This method has proven to be promising but also challenging. Results only allowed tentative interpretations of the 3D melt distribution. This study has provided a better understanding of localisation and partial melt in deformed metapelites and has also provided insights into the potential of a Focused Ion Beam–Scanning Electron Microscope (FIB-SEM) as a tool for geology.

Preface

This MSc thesis is the result of a collaboration between the Experimental Rock Reformation lab (ERDL) of the ETH Zurich and the High Pressure and Temperature Lab (HPT-lab) of the University of Utrecht. The supervision of the ETH was provided by Dr. Santanu Misra and Dr. Karsten Kunze and the supervision of the University of Utrecht was provided by Prof. Dr. Chris Spiers.

The rock deformation experiments were performed in the ERDL under the direct supervision of Dr. Santanu Misra. The Image Analysis with the SEM and FIB-SEM took place at the Electron Microscopy center of the ETH Zurich (EMEZ) under the supervision of Dr. Karsten Kunze. The writing took place in Utrecht under the supervision of Prof. Dr. Chris Spiers.

Table of Contents

| | |
|---|----|
| Abstract..... | 1 |
| Preface | 2 |
| Table of Contents..... | 3 |
| List of Figures | 5 |
| List of Tables | 7 |
| Chapter 1. Introduction | 8 |
| 1.1 Current state of research..... | 8 |
| 1.2 Goal and research questions..... | 19 |
| Chapter 2. Materials and Methods..... | 20 |
| 2.1 Sample preparation and characterization | 20 |
| 2.2 Deformation apparatus (Paterson Rig) | 21 |
| 2.3 Post-deformation analysis | 28 |
| Chapter 3. Results | 34 |
| 3.1 General overview both compositions..... | 34 |
| 3.2 Deformation and analysis of quartz-rich samples | 37 |
| 3.3 Deformation and analysis of muscovite-rich samples | 50 |
| Chapter 4. Discussion..... | 67 |
| 4.1 General characteristics deformation experiments | 67 |
| 4.2 Static vs. Dynamic systems: impact on melt transport..... | 72 |
| 4.3 Effect of chemical composition..... | 77 |
| 4.4 Effect of strain rate ($\dot{\gamma}$)..... | 80 |
| 4.4 Effect of finite strain (γ) | 81 |
| 4.5 Application in Geological context | 82 |
| 4.6 Errors and deviations in experiments | 84 |
| Chapter 5. Conclusions | 85 |
| Chapter 6. Recommendations and outlook..... | 87 |
| References | 88 |
| Acknowledgements..... | 92 |

| | |
|---|-----|
| Appendix A XRD plots | 93 |
| Appendix B FIB-SEM..... | 100 |
| Appendix C Stepping Strain Rate (SSR) Experiments | 101 |
| C.1 SSR of Sample 14 Quartz:Muscovite 70:30..... | 101 |
| C.2 SSR of Sample 16 Quartz:Muscovite 30:70..... | 103 |
| Appendix D Microprobe..... | 105 |
| D.1 Quartz-rich, high strain rate high finite strain (P1672) | 105 |
| D.2 Muscovite-rich, high strain rate, high finite strain (P1129)..... | 107 |
| D.3 Melt measurements Microprobe | 108 |

List of Figures

| | |
|--|----|
| Figure 1.1 Metapelite under progressive strain (Misra <i>et al.</i> , 2009)..... | 13 |
| Figure 1.2 Metamorphic facies diagram for metapelites and metabasites (Bousquet <i>et al.</i> , 2008) | 14 |
| Figure 1.3 Three dimensional images of partial melt in basalt-olivine aggregates (Zhu <i>et al.</i> , 2011)..... | 16 |
| Figure 1.4 Recurring structures in porous sheared rocks (Logan, 2007). | 17 |
| Figure 1.5 Differential stress vs. displacement curve (Logan, 2007). | 17 |
| Figure 2.1 Schematic overview of the Deformation apparatus | 23 |
| Figure 2.2 Representative assembly experiments | 23 |
| Figure 2.3 Torsion mechanism and sample geometry (Paterson and Olgaard, 2000). | 24 |
| Figure 2.4 FIB milling (De Winter <i>et al.</i> , 2009)..... | 30 |
| Figure 2.5 Set-up of the FIB-SEM tomography (De Winter <i>et al.</i> , 2011). | 30 |
| Figure 2.6 FIB-SEM milled section on sample P1129 (a) at an angle and (b) perpendicular to the surface. 31 | |
| Figure 3.1 Undeformed samples, quartz-rich and muscovite-rich | 35 |
| Figure 3.2 representative overview of the deformed samples in SEM BSE..... | 36 |
| Figure 3.3 Deformed samples of the quartz-rich series..... | 38 |
| Figure 3.4 Stepping Strain Rate (SSR) experiments quartz-rich series (Q:M 70:30). | 39 |
| Figure 3.5 Shear Stress vs. Shear Strain of the quartz-rich sample | 41 |
| Figure 3.6 Overview of quartz-rich samples (S14) | 44 |
| Figure 3.7 Overview of zoom-ins quartz-rich samples (S14) | 45 |
| Figure 3.8 TGA Sample 14 Q:M 70:30 and Sample 16 Q:M 30:70. | 48 |
| Figure 3.9 TGA undeformed and deformed quartz-rich samples..... | 49 |
| Figure 3.10 Deformed samples of muscovite-rich composition..... | 50 |
| Figure 3.11 Results of Stepping Strain Rate (SSR) experiments muscovite-rich series (Q:M 30:70)..... | 51 |
| Figure 3.12 Shear Stress vs. Shear Strain of the muscovite-rich sample. | 54 |
| Figure 3.13 Shear Stress vs. Shear Strain in all experiments. | 55 |
| Figure 3.14 Overview of muscovite-rich samples (S16)..... | 57 |

| | |
|--|----|
| Figure 3.15 Overview of zoom-ins muscovite-rich samples (S16). | 58 |
| Figure 3.16 Muscovite-rich (S16) samples with high finite strain (γ) and variable strain rate ($\dot{\gamma}$) | 59 |
| Figure 3.17 XRD plot with minerals P1670 identified using the ICCD database..... | 60 |
| Figure 3.18 Cation abundance Al vs. Si in muscovite measurements P1670. | 61 |
| Figure 3.19 AKF diagram melt composition sample P1670. | 61 |
| Figure 3.20 Elemental mapping melt pocket sample P1670 by the EMPA. | 62 |
| Figure 3.21 TGA muscovite-rich samples:..... | 64 |
| Figure 4.1 Paterson Rig experiments after Tumarkina (2012)..... | 74 |
| Figure 4.2 Model for the mechanical evolution of a shear zone networks under progressive strain (Fusseis <i>et al.</i> , 2009)..... | 84 |

List of Tables

| | |
|---|----|
| Table 3.1 Overview of the deformation experiments | 34 |
| Table 3.2 Different types of shear bands | 37 |
| Table 3.3 Matrix of variable strain rate and finite strain for quartz: muscovite volume ratio 70:30 | 37 |
| Table 3.4 Quartz: muscovite 70:30 (sample 14) and presence of melt-filled shear bands | 46 |
| Table 3.5 Matrix of variable strain rate and finite strain for quartz: muscovite volume ratio 30:70. | 50 |
| Table 4.1 Values power law exponent quartz-rich sample..... | 69 |
| Table 4.2 Values power law exponent muscovite-rich sample. | 69 |
| Table 4.3 Overview static experiments Tumarkina (2012) | 72 |
| Table 4.4 Overview microstructural differences per composition. | 78 |
| Table 4.5 Overview mechanisms behind differences resulting from different composition. | 79 |
| Table 4.6 Variation matrix muscovite-rich experiments | 81 |

Chapter 1. Introduction

Metapelitic rocks are common metamorphic rocks that therefore play an important role in the mechanical and rheological behaviour of the crust. Many experimental and field studies have been undertaken to establish their behaviour in the crust (Vielzeuf and Holloway, 1988; Berger and Kalt, 1999; Connolly *et al.*, 1997; Rushmer, 2001; Bousquet *et al.*, 2008; Misra *et al.*, 2009; Misra *et al.*, 2011; Tumarkina *et al.*, 2011). Partial melting is directly related to shear localisation and migration pathways for the melt (Misra *et al.*, 2009; Kohlstedt and Holtzman, 2009). Therefore it may also dictate the composition of the partial melt that migrates into the upper layers of the crust (Connolly *et al.*, 1997). Shearing occurs when the continental crust experiences tectonic stress as a result of an orogeny or intrusion (Rushmer, 2001). From field based research it is known that melt in the middle to lower crust and upper mantle primarily occurs in high strain zones (Kohlstedt and Hoffman, 2009). To improve and enhance the understanding of these systems it is important to experimentally test and model the behaviour of rocks under high strain, pressure and temperature. Previous research focused on the process of melt formation and the relation between deformation and the formation and segregation of melt (Rushmer, 2001; Misra *et al.*, 2009; Tumarkina *et al.*, 2011). However, questions remain surrounding this topic. It is not clear how the melt formation and shear localisation is related to different compositions, different strain rates ($\dot{\gamma}$) and finite strains (γ). Also, the 3D structure of the localisation features has not been established. This MSc research aims to address and solve these issues. This is achieved by the deformation of metapelites under elevated pressure and temperature and 3D imaging of deformed synthetic metapelites.

This master thesis is the result of a cooperation between the University of Utrecht and the ETH Zürich. Prof. Dr. Chris Spiers of the High Pressure and Temperature (HPT) lab of the Utrecht University and Dr. Santanu Misra and Dr. Karsten Kunze both of the ETH Zürich have supervised this thesis.

1.1 Current state of research

In this section we will digress on the work that has been done previously on this topic. Additionally we will also elaborate on the fundamental processes of shear deformation and localisation.

1.1.1 Partial melting of metapelites

Experiments on the partial melting of metapelites have been done by several authors (Connolly *et al.*, 1997; Rushmer, 2001; Misra *et al.*, 2009; Van Diggelen *et al.*, 2010; Misra *et al.*, 2011; Tumarkina *et al.*, 2011). There have also been field studies focused on partial melting of metapelites (Bousquet *et al.*,

2008). From these papers a framework of the mechanical and chemical behaviour of this material can be established.

1.1.1.1 Stable versus active tectonic settings

It has been noted by several authors (Rushmer, 2001; Misra *et al.*, 2009) that there are considerable differences in behaviour of metapelites in stable versus active tectonic settings. Rushmer (2001) viewed this problem on a large scale and Misra *et al.* (2009) looked at the differences on a sample scale.

When deformation is absent in the lower crust there is static grain growth, there are equilibrium metamorphic textures and there is no clear preferred orientation in the crystals. Melting initiates with the breaking down of mica and amphiboles as water groups are released. Because of the volume increase of the melt, cracks form which create significant permeability. The latter is efficient enough to allow for melt segregation, even in the absence of deformation. However, when water saturated melting occurs in stable tectonic setting the migmatites that form remain close to the source. Whereas if there was deformation the melt could be transported further (Rushmer, 2001). In active tectonic environments the processes are more complicated. Rushmer (2001) describes four steps that take place in these rocks on a large scale. First of all (1), strain partitions into weaker rocks, and (2) then the latter form shear zones. Thirdly (3) this process of weakening is aggravated by partial melting during which the strain partitions into the weak zones. Lastly (4), these shear zones can be used as pathways for melt-assisted granular flow. Altogether, this is a positive feedback system. The efficiency of the melt segregation will increase with increasing strain rate because partial melting enhances cataclasis at temperatures at which normally the material would behave ductilely (Rushmer, 2001).

On the sample scale Misra *et al.* (2009) observe that at a pressure of 300 MPa and a temperature of 750 °C the dynamically deformed sample ($\dot{\gamma} = 3 \cdot 10^{-4} \text{ s}^{-1}$) showed 1.72 times more melt than the static (non-deformed) sample. From this it was concluded that shearing leads to an increase of partial melt. It is important to understand the difference between a dynamic and static system is important because it can explain why melt in active orogenic systems forms and migrate while it does so to a lesser extent in stable continental regions. In order to explain this difference the kinetics of the reaction must be increased. There are four possible reasons explained by Misra *et al.* (2009) and those are analysed and assessed by Tumarkina *et al.* (2011). The factors that can increase the reaction kinetics are (1) surface energy (2) shear heating (3) melt migration and (4) reduction of mean stress. Tumarkina *et al.* (2011)

analysed these factors and found that only shear heating could significantly increase the reaction kinetics.

There has also been incipient work on the role of strain and strain rate on partial melting and crystallization and the geological implication of this process (Misra et al, 2011). In this paper the focus lay on determining the effect of *high* finite strains (γ of 1-15). Variable strain rates were not attained in separate experiments as they will be in our experiments but rather by analysing the sample along the diameter. Going from the outer rim to the inner point of the sample cylinder the finite strain and strain rate decrease to zero. See Chapter 2. Materials and Methods for further details. It was found that deformation strongly affects partial melting. For $\gamma < 5$ partial melting is dominant over crystallization, but this reverses at higher finite strains. An increase in strain rate has a positive influence on crystallization. Altogether these conclusions have an impact of the understanding of large-scale crustal geology. Weaker zones in the crust enable the *decoupling* of a structure from a previously *coupled* larger structures on the lithosphere-scale. These weaker zones can be caused by the accumulation of melt along planar zones (shear zones) (Misra *et al.*, 2011).

From this enquiry into the role of deformation it has become apparent that the development of partial melt is important in active tectonic settings and also that the behaviour is markedly different than in stable tectonics. How the effect of deformation co-varies with other variable geological factors (composition, strain rate, finite strain) has not been explored fully.

1.1.1.2 Petrology of the reactions in metapelites

Previous research has also focused on the petrology and mineralogy of the melting reactions in metapelites. Several authors have noted that that melt starts at the quartz muscovite boundary (Connolly *et al.*, 1997b; Rushmer, 2001; Misra *et al.*, 2009). Rushmer (2001) experimented on a two mica pelite. There was a separate melting reaction of muscovite and biotite. Muscovite dehydration dominates the process even if biotite is present in the sample. The following reactions occurred:

- muscovite + quartz → melt +biotite +alumnosilicate
- biotite + plagioclase + quartz → k-feldspar + orthopyroxene + spinel + melt

Connolly (1997) demonstrated that melt formation in a metaquartzite with muscovite results in microcracking. The partial melt starts at the muscovite-quartz boundary and the muscovite is replaced by mullite and biotite melt. The microcracks emanate from the melt pockets. The experiments were performed at 800 MPa and 950-1126 K (677-853 °C).

Misra *et al.* (2009) focused on the petrological and thermodynamic aspects of a metapelite that subjected to shear deformation at a temperature of 750 °C (1023 K) and a pressure of 300 MPa. The sequence of deformation localisation and melt formation with increasing shear strain is shown in Figure 1.1 below. The images were made in BSE SEM. The experimental observations indicate that the nucleation of shear bands and the onset of melting are independent of one another. This is because firstly in the brittle field the Riedel shears form (strain localisation) and then later melt forms. Once melts start to form the rheology becomes ductile and strain softening occurs. The sequence of the processes within a sample is:

1. brittle shear localisation occurs
2. melt occurs and weakening in weaker zones is enhanced
3. melt migrates into the shear bands, which results in an acceleration of weakening
4. steady state flow limits melt generation.

There have also been experiments on similar rocks under lower pressures than the research by Misra *et al.* (2009) and Tumarkina *et al.* (2011). Van Diggelen *et al.* (2010) explored the high strain behaviour of

synthetic muscovite fault. The goal was to assess whether or not the weakness in fault gauges can be explained by the muscovite gauge. This goal was achieved by simulating fault gauge under normal stresses up to 100 MPa and 600 °C, with fluid pressures of 20-100 MPa. The strain went up to 100 and the shear strain rates varied between 10^{-5} to 10^{-3} s^{-1} . This resulted in pervasive and localised cataclasis associated with strain hardening up to 600 degrees. At 700°C (973 K) partial melting and chemical alteration occurred. The conclusion was that muscovite gauge strengthens with pressure and temperature therefore it most likely does not contribute to long-term weakness of major crustal shear zones (Van Diggelen *et al.*, 2010).

An overview of the experiments by Misra et al. (2009)

After pressurization at 300 MPa the initial porosity of the sample of 15 % had halved to 7-9% porosity.

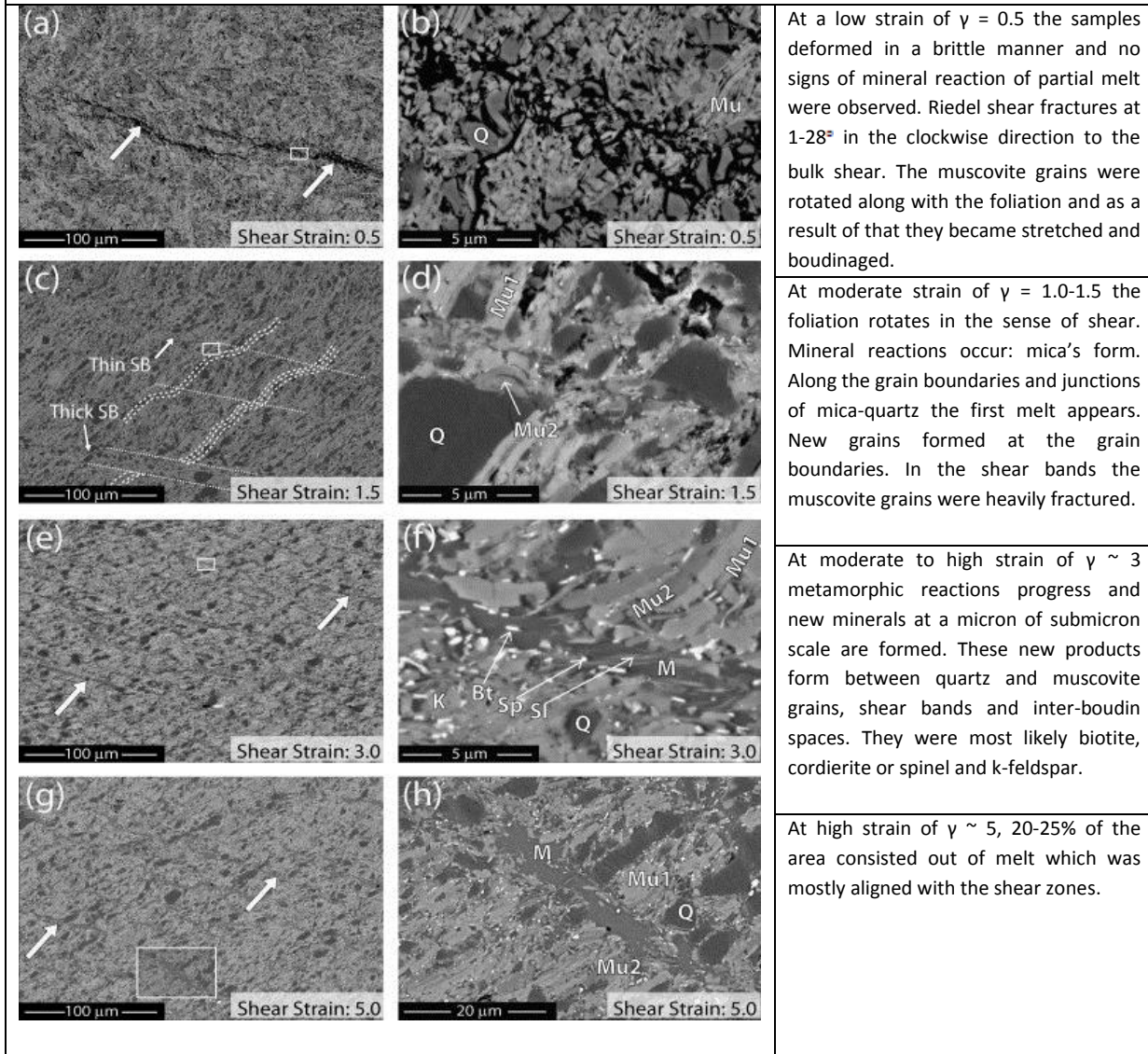


Figure 1.1 Metapelite under progressive strain. SEM BSE images in the left column and observations in the right columns.

After Misra et al. (2009)

1.1.1.3 Metamorphism of metapelites in the field

The metamorphism of metasediments in the Alps was investigated by Bousquet *et al.* (2008). From this and previous work on this topic a phase diagram was constructed, see Figure 1.2. This shows that under the conditions that this research will be performed (750 °C and 300 MPa) the material would undergo partial melt under wet conditions. This figure by Bousquet *et al.* (2008) assumes an absence of deformation, whereas we will deform the metapelites in this research. Despite of this discrepancy the figure can be used as an approximation.

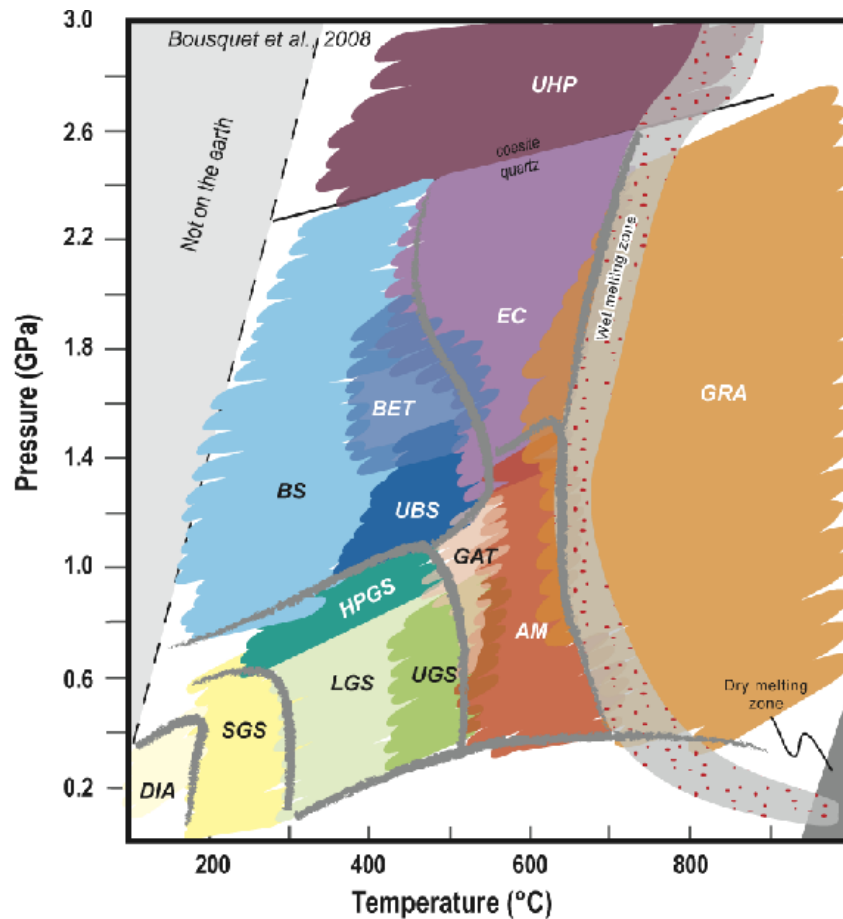


Figure 1.2 Metamorphic facies diagram for metapelites and metabasites (Bousquet *et al.*, 2008).

1.1.2 Partial melting in a global context

1.1.2.1 Partial melting in orogenies and spreading ridges

The occurrence of partial melt in association with shear zones has a profound effect on the rheology of crustal rocks, especially in crustal collision zones. Wei *et al.* (2001) studied the presence of widespread high electric conductivity in the Tibetan crust. He linked the extremely high conductivity and low seismic velocity in the shallow (15-20 km) southern part to the presence of partial melt and aqueous fluids in the crust. The deeper (30-40 km) northern high conductivity was solely explained by the presence of partial melt. Evans *et al.* (1999) focused on partial melt in order to find the source region for Mid Ocean Ridge (MOR) basalts of the East Pacific Rise. Using the magnetotelluric component of the Mantle Electromagnetic and Tomography (MELT) Evans *et al.* (1999) found an anomalously low resistivity west of the ridge. The latter is explained as a result of the presence of interconnected partial melt (1-2 %) melt and water in the form of dissolved hydrogen. Other authors have focused on the role of quartz and muscovite specifically in the role of deviant seismic signals (Mahan, 2006; Naus-Thijssen *et al.*, 2011; Ward *et al.*, 2012). The preferred orientation of muscovite was found to profoundly affect the seismic wave velocity. The latter can be impacted by deformation. These examples show the importance of partial melting and orientation of foliation of rocks in fundamental systems such as continental collision zones and spreading ridges

1.1.1.2 Partial melting in peridotites and 3D imaging

Partial melt in metapelites is of particular importance because of the liberation of water in the metamorphic reactions. Many authors have done research into the partial melting of other types of rocks, particularly peridotites (Zhu *et al.*, 2011; Evans *et al.*, 1999; Kelley and Cottrell, 2009). Because of the useful analogies that can be gained from these experiments it is important to also discuss their findings. Partial melt in peridotites plays a major role in the formation of melt that is expelled along ocean ridges (Zhu *et al.*, 2011). Zhu *et al.* (2011) used x-ray synchrotron imaging to model partial melt with various melt fractions in 3D. This research is different from this proposals' in the sense that (a) the composition of a peridotite is markedly different from a metapelite (not hydrated) and (b) the imaging method is different. The different x-ray method is non-destructive, whereas the FIB is inherently destructive. The resulting images are shown in Figure 1.3. Zhu *et al.* (2011) has shown that between melt fractions of 0.02 and 0.20 melt channels or tubes occur and that they could dominate transport. Below a melt fraction of 0.02 melt only exists in the films between two grains. Transport along channels

is faster than along the films. From the three-dimension modeling it is concluded that strong channelization is a transport mechanism of the partially molten mantle.

Thus from this analysis of partial melting in a global context we can conclude that (1) partial melt is present and important in orogenic belts and spreading ridges plus (2) that three-dimensional modeling on other materials provides more understanding of partial melt connectivity.

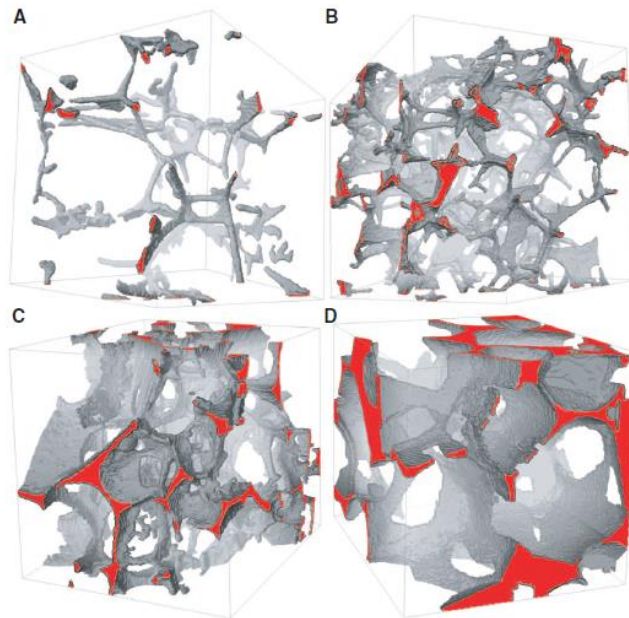
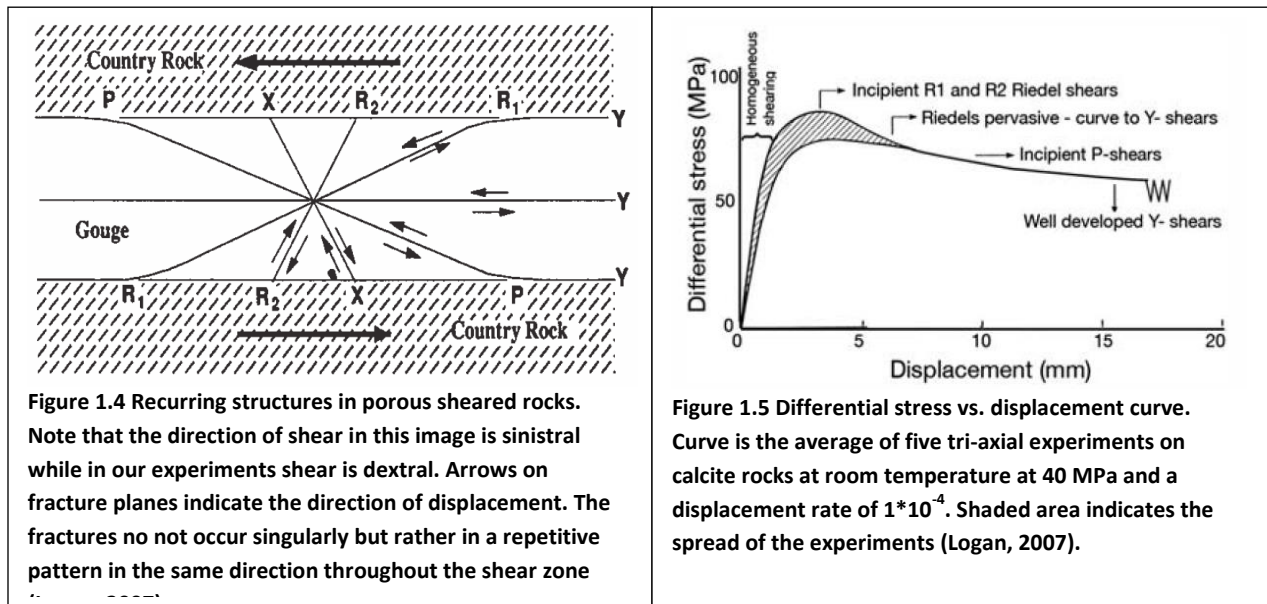


Figure 1.3 Three dimensional images of partial melt in basalt-olivine aggregates. The length of the sides of the cube is 140 μm . A = 0.02, B= 0.05, C =0.10 D=0.20 melt fraction. Grey indicated the interface between the melt and the olivine crystals, red indicates the inner part of a melt channel (Zhu et al., 2011).

1.1.3 Microstructural features shear zones.

It is important to establish which structures form as a result of the shearing and what effects they have because these features are also expected in the experiments. Hence, a complete understanding of the structures is key to the understanding of the results of the experiments. Logan (2007) digresses on these specific shear-zone structures. Shearing of porous rocks leads to repetitive and predictable fracture geometries. These fractures are in the R_1 , R_2 , P and Y direction, as illustrated in Figure 1.4. R_1 is also referred to as low angle Riedel shear and R_2 is the high angle Riedel shear. Fault gauge can form as a result of movement along these fractures. This weakens the rock by grain size reduction. Consequential concentration of deformation in the zone can lead to compaction of the material in the gauge zone. In Figure 1.5 a Differential stress vs. displacement curve with strain hardening and weakening is shown

with the indication which types of fractures generally occur during the shearing process (Logan, 2007). In other words, the development of new planes on which movement can occur severely impacts the “ease” of glide. The synthetic materials deformed in our experiments contained around 12-15 % porosity, but this was decreased to 7-9 % as the samples were loaded to the experimental condition of 300 MPa.



1.1.4 Deformation mechanisms in polycrystalline aggregates

Non-brittle deformation mechanisms in rocks can behave according to a viscous-power law rheology. Within this group, sub-mechanisms can be distinguished which are important as they control different localisation behaviour. Schmid *et al.* (1977) discerned three different flow regimes which he coupled to two different deformation mechanisms. Experiments were performed on Solnhofen Limestone with a grain size of 5 μm at temperatures between 600 and 900 $^{\circ}\text{C}$ (873 and 1173 K). The experiments took place at high temperatures, $T/T_m > 0.4$. Here T_m indicates the melting temperature of the material. The three creep regimes are:

1. Exponential stress dependence on strain rate in that fits in the form $\dot{\epsilon} \propto \exp(C\sigma)$

2. Power law creep with $n \sim 4,7$ based on the formula $\dot{\epsilon} = A e^{\frac{-H}{RT}} \sigma^n$

Controlled by dislocation creep, more specifically dominated by climb-controlled creep.

3. Superplastic regime with $n \sim 1,7$. This behaviour is heavily dependent on grain size. At the same stress, when the grain size is decreased the strain rate increases.

Here, n comes from the same equation as in regime 2.

Additionally $\dot{\epsilon}$ refers to the strain rate in s^{-1} , A and C are constants, σ is the stress in Pa, H is the enthalpy in J or J/mol, R is the universal gas constant and T temperature in K.

Microstructures are key to determine and recognize the deformation mechanism. In regimes 1 and 2 intracrystalline plasticity is dominant. The deformation mechanism is dislocation creep and the rate limiting step is diffusion. In regime 3 superplasticity dominates which is characterized by grain boundary sliding. In regimes 1 and 2 grains are flattened and intragranular plasticity (dislocation movement) causes undulose extinction and subgrain boundaries under the optical microscope. Regime 3 shows equiaxed grains and straight grain boundaries (Schmid *et al.*, 1977). The SEM and FIB-SEM imaging techniques will be used to distinguish these different mechanisms in the experiments done in this project. The power law exponent can also be seen as an indicator of how fast localisation or “necking” occurs. Superplasticity “necks” (n is ~ 1) are relatively stable whilst in dislocation creep ($3 < n < 6$) localisation occurs much more rapidly. In superplastically deforming rocks can accommodate large permanent strain (Mcdonnell *et al.*, 1999).

1.2 Goal and research questions

In the previous section the importance of this topic and the current state of research was established. From this we have distilled the unresolved issues. The goal of this research is to simulate, visualize and analyse the behaviour of metapelites in shear zones under different circumstances. The behaviour of rocks in shear zones is essential for the understanding of the overall mechanical behaviour of the crust under tectonic stress. The particular focus will lie on the partial melting. This will be done by mapping the melt distribution of synthetic metapelites at elevated pressure and temperature and large shear deformation.

This goal will be achieved by and answering the following main research questions: *how does partial melting and localisation vary as functions of composition, strain rate and finite strain in synthetic metapelites?* To answer this question the following sub questions or goals were formed.

- a. Partial melting and localisation in metapelites as a function of
 - (1) Composition
 - (2) Strain rate
 - (3) Finite strain
- b. Mechanical properties and rheology of sheared metapelites
- c. 3D structure of melt (novel method)
- d. Relation of these findings to localisation and melt migration in geological formations.

Answering these questions will literally and figuratively add another dimension to the understanding of rock behaviour in shear zones. This will be ensured by the determination of the localisation and partial melting under unexplored variables and by the novel usage of FIB-SEM 3D imaging.

Chapter 2. Materials and Methods

This chapter is composed of three parts that will altogether enable us to emulate and analyse the behaviour of metapelites in shear zones. Samples are synthesized with the desired foliation and chemical composition (part 1). Subsequently these samples will be sheared under high pressure and temperature by applying the torsion in the deformation apparatus (part 2). Finally the experimentally deformed samples are imaged in 2D (SEM) and in 3D (FIB-SEM tomography) and chemically analysed with X-ray diffraction (XRD), the electron microprobe and Thermogravimetric Analysis (TGA) (part 3).

2.1 Sample preparation and characterization

In order to be able to constrain the chemical composition of the samples they were synthesized rather than taken from nature. The samples were prepared by Dr. S. Misra and have been used in other publications e.g. Misra *et al.* (2009), Tumarkina *et al.* (2011) and Misra *et al.* (2011). The benefit of using these samples is that they can be compared effectively to previous enquiries.

The synthetic rock is made of two different starting materials (1) fine grained quartz and (2) fine grained muscovite. The latter were provided by Alberto Luisoni, Switzerland (www.albertoluisoni.ch). The grain size, density and chemical composition of the starting materials were determined. The grain size was measured with a *MasterSizer 2000* and respectively the sizes of quartz and muscovite were 4-5 μm and 30-34 μm . The Helium Gas Pycnometer *AccuPyc 1300* measured the densities of quartz and muscovite to be 2.65 and 2.82 grams per cubic centimeter. Chemical analysis by an electron microprobe found that the composition of muscovite is $(\text{K}_{0.9}\text{Na}_{0.1})(\text{Al}_{1.6}\text{Fe}_{0.3}\text{Mg}_{0.1})[\text{Si}_{3.2}\text{Al}_{0.8}\text{O}_{10}](\text{OH})_2$. Both XRD and microprobe analysis confirmed that the quartz was of a very pure composition (Misra *et al.* 2009).

The starting materials were used to synthesize two types of biminerallitic rock: (1) quartz:muscovite in a volume ratio of 30:70 and (2) quartz:muscovite in a volume ratio of 70:30. The powders of the starting materials were added together in appropriate proportions while being continuously slowly mixed by alcohol. The latter was done in order to avoid the clotting of quartz grains. In order to dry the mixture the containers were kept under an infrared lamp and were then oven dried for 24 hours at 110°C (383 K). The powder mixture was transformed into synthetic rock by firstly performing Uniaxially Cold-pressing (UCP) and secondly by Hot Isostatic pressing (HIP). During the first step (UCP) the porosity was decreased and the material was homogeneously compacted by filling and pressing small portions of the mixture with the same load (200 MPa). This was done in a stainless steel canister of 200 mm long, with a 50 mm inner diameter and 2 mm wall thickness. This process led to the formation of foliation parallel to

the surface of the canister. The canisters were sealed and the sealing was successfully tested by putting the canisters in water and vacuum conditions. In the second part (HIP) the canisters were subjected to confining pressures of 160 MPa and 590°C (863 K) in the internally heated gas vessel *ABRA Fluid AG Switzerland* for another 24 hours (Misra *et al.*, 2009).

The desired foliation was obtained in the following manner. Small cores were drilled out of the UCPped and HIPped canister in the direction perpendicular to the foliation formed by the UCP pressing. The foliation that resulted is illustrated in Figure 2.3. The porosity calculated using the Helium Gas Pycnometer yielded a porosity ranging between 12-15% (Misra *et al.*, 2009).

The structures of the initial samples were subsequently characterized by using scanning electron microscopy (SEM) in electron backscattered mode (BSE). This is relevant because the microstructure can impact the behaviour of the sample during deformation. More on this method can be found in this chapter under part three. The imaging showed that the muscovite grains were oriented sub parallel to the foliation formed during UCP. The quartz grains are located in between the planar muscovite grains and are locally enveloped by the muscovite flakes. Pores do exist and generally occur at the sharp edges of quartz or flat basal planes of muscovite grains (Misra *et al.*, 2009).

2.2 Deformation apparatus (Paterson Rig)

2.2.1 Introduction

In the field of experimental rock deformation the goal is to emulate natural deformation systems in a laboratory environment. The Paterson Rig is a tri-axial deformation apparatus that is internally heated and pressurized by argon gas. It provides a means to emulate a natural deeper crustal environment, both by providing appropriate pressure and temperature ranges, but also by deforming the sample. However, natural deformation processes occur on geological time scales (millions of years) and it is not possible to perform experiments during such long periods of time in the lab. This feature poses an inevitable limitation on the research. The Paterson is equipped with a torsion actuator motor which can shear rock samples. Simple shear occurs in a wide range of geological settings, particularly in orogenies. Beside simple shear the Paterson can also be used to perform (1) static experiments (i.e. without deformation) and (2) pure shear by coaxial deformation of the rocks. The rig can be used to attain confining pressures up to 500 MPa and temperatures up to 1600 K (Paterson and Olgaard, 2000). A schematic illustration of the assembly set-up can be found in Figure 2.1(a), and a photo of the instrument in the lab in Figure 2.1(b).

2.2.2 Jacket assembly

The rock sample is confined between alumina pistons and spacers, Partially Stabilized Zirconia (PSZ) pistons and an iron alloy jacket before being inserted into the deformation apparatus. This set-up ensures a stable assembly for both increased temperature and pressure. This assembly is shown in Figure 2.2. Because the thickness of the sample and spacers is smaller than the thickness of the pistons the jacket was swaged. This resulted in an increase of thickness of the jacket from 0.25 mm to 0.4 mm in the undeformed state and 0.6 mm in the deformed state.

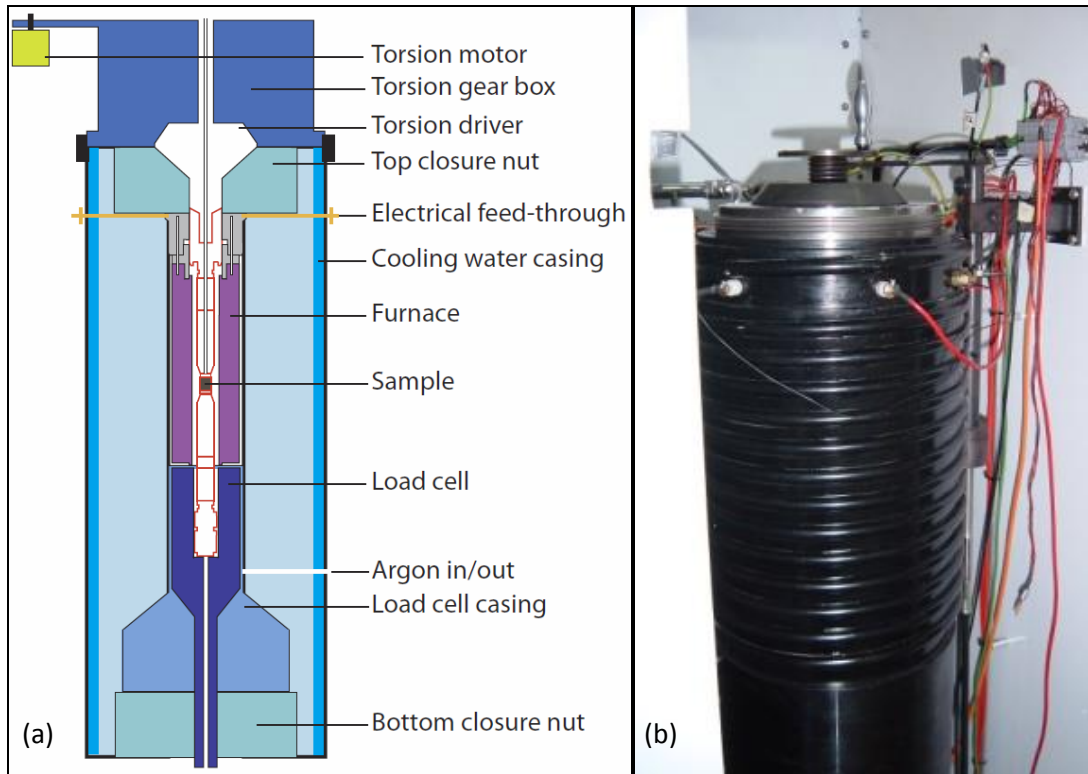


Figure 2.1 (a): Schematic overview of the deformation apparatus (Paterson rig) after Paterson and Olgaard (2000). The width of the column is 30 cm. On the left in (b) the apparatus in the experimental Rock deformation laboratory at ETH Zürich. The width of the Rig is roughly half a meter (courtesy S. Misra, 2012).

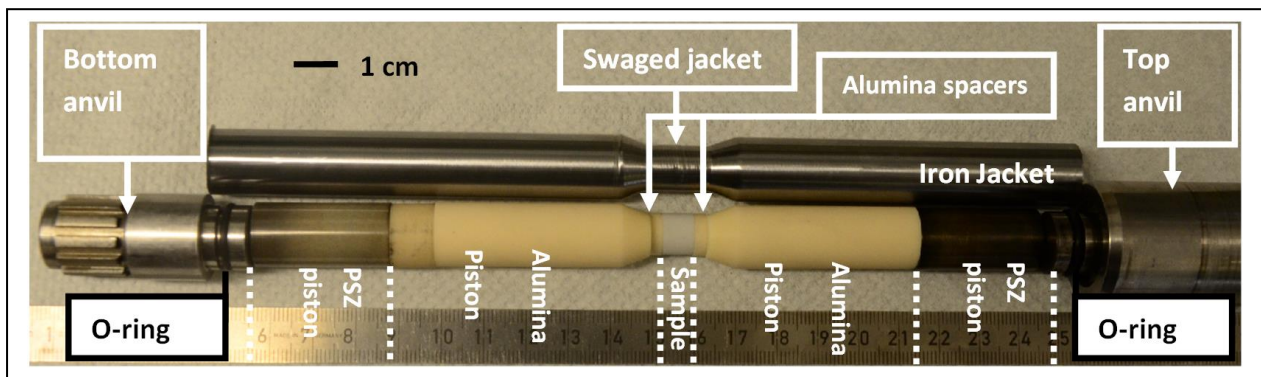


Figure 2.2 Representative assembly experiments

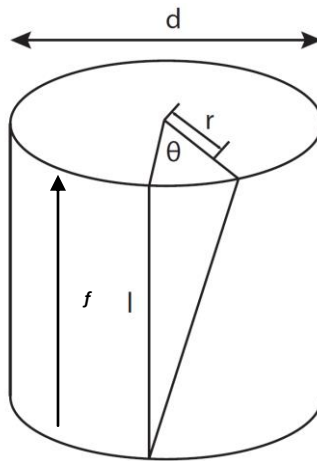


Figure 2.3 Torsion mechanism and sample geometry (Paterson and Olgaard, 2000). The abbreviations d , l , r and θ respectively denote the diameter, length, radius and the angular displacement of the sample. The direction of the foliation formed during sample synthesis denoted with f .

2.2.3 Experimental procedures Paterson Rig

In this project, the confining pressure and temperature were held at 300 MPa and 750 °C (1023 K) respectively for all experiments. The strain rate ($\dot{\gamma}$) of experiments was either $1 \cdot 10^{-4} \text{ s}^{-1}$ or $3 \cdot 10^{-4} \text{ s}^{-1}$.

In order to achieve these settings the sample assembly was first subjected to a minimal axial load to couple the segments. Subsequently the sample was pressurized up to ~ 230 MPa and then the furnace was heated. A confining pressure of minimum 50 MPa is required to operate the furnace as it accommodates the expansion of the argon gas that results from the heating. During the heating to 750 °C the gas expands and the confining pressure reaches 300 MPa. Small iterations in case of deviations from this mark were accommodated by either the release or the repeated pumping of the gas. The sample was heated at a rate of 15 °C per minute. After the required shearing was obtained the sample was quenched at a rate of 90 °C per minute. The temperature measurements were done using a thermocouple of K-type placed 3 mm above the sample. Because of the heating from all sides the deviation from the goal temperature is no more than 1 °C.

The torsion was performed by rotation of the motor and rotations per minute (rpm) of the motor are calculated dependent on the specific size of the sample. The sample sizes were measured by a 0.01 mm precise calliper. The strain rate ($\dot{\gamma}$) in these experiments was either $1 \cdot 10^{-4} \text{ s}^{-1}$ or $3 \cdot 10^{-4} \text{ s}^{-1}$. The Gear ratio is a unit-less property of the torsion actuator motor of the Rock deformation laboratory at ETH and is 54600.

$$\text{sample twist rate } \left(\frac{1}{\text{s}}\right) = \frac{\text{strain rate } \left(\frac{1}{\text{s}}\right) * \text{sample length (mm)}}{\text{sample diameter (mm)} * \pi} \quad (\text{Eq. 2.1})$$

$$\text{sample rpm} = 60 * \text{sample twist rate } \left(\frac{1}{\text{s}}\right) \quad (\text{Eq. 2.2})$$

$$\text{motor rpm} = \text{Gear ratio} * \text{sample rpm} \quad (\text{Eq. 2.3})$$

2.2.4 Torque mechanism

As stated previously the simple shearing is performed by torsion, which implies that the strain is zero at the center of the core and increases radially to its maximum at the edge of the sample. The shear strain γ_r at any given radius r of the sample is given by equation 2.4. The abbreviations l , r and ϑ respectively denote the length, radius and the angular displacement of the sample. In equation 2.5 the derivative over time or the strain rate is given (Paterson and Olgaard, 2000).

$$\gamma_r = \frac{r\theta}{l} \quad (\text{Eq. 2.4})$$

$$\dot{\gamma}_r = \frac{r\dot{\theta}}{l} \quad (\text{Eq. 2.5})$$

A schematic overview of the sample and the different parameters is given in Figure 2.3.

Because we measure the surface of the cylinder as we want to the effect of the largest strain we can simplify the formula's given above to equations 2.6 and 2.7. The $\dot{\theta}$ and ω refer to respectively twist rate in radians per second and the twist rate in revolutions per second (Paterson and Olgaard, 2000).

$$\gamma = \frac{d\theta}{l} \quad (\text{Eq. 2.6})$$

$$\dot{\gamma} = \frac{d\dot{\theta}}{l} = \frac{\pi d\omega}{l} \quad (\text{Eq. 2.7})$$

When we calculate the torque we will now only look at the outer rim of the sample and we will assume that the material is a solid. The torque the sample is subjected to is measured by Linear Variable Differential Transformers (LVDT).

Paterson and Olgaard (2000) describe the relation between shear stress and internal torque during shearing. In Equation 2.8 below, τ , n , M and d respectively refer to shear stress (Pa), power law exponent, internal torque (Nm) and the diameter of the sample (m). Here we assume that the material behaves in a power-law stress-strain dependence (Eq. 2.9) to the power n and that the sample possesses homogeneous properties. This parameter is determined experimentally by stepping strain rate experiments.

$$\tau = \frac{4M(3+1/n)}{\pi d^3} \quad (\text{Eq. 2.8})$$

$$\dot{\gamma}_r = A\tau_r^n e^{\frac{-Q}{RT}} \quad (\text{Eq. 2.9})$$

In Equation 2.9 A , n and R are constants. T is temperature (K), Q is the activation energy (J) and R is the universal gas constant ($\text{Jmol}^{-1}\text{K}^{-1}$). $\dot{\gamma}_r$ is the strain rate (s^{-1}) and the r in the subscript refers to the radius of the sample. All parameters are in SI units (Paterson and Olgaard, 2000).

A prerequisite to be able to deform the sample is that the strength of the rock is lower than the strength of the other components of the assembly and the friction between those. As a consequence, the rock

sample and surrounding jacket will be deformed during the experiment. If this is not the case, slipping can occur on one of the surfaces that are weaker than the rock sample. If the slipping is significant the iron jacket can rupture and degas, nullifying the goals of the experiment.

2.2.5 Stepping Strain Rate (SSR) experiments and the power law exponent

In the previous paragraph on the torque mechanism the relation between the power law exponent (n), internal torque and strain rate was explained. Internal torque and shear stress are linearly related as shown in equations 2.8 and 2.9 and simplified in equation 2.10. Equation 2.9 also shows that if the strain rate changes, this results in a change of the internal torque or vice versa. In between the changes of the strain rate there is a transition of the internal torque. The latter is however not in equilibrium and is therefore not taken into account. Solely the points at which the strain rate is in equilibrium with the internal torque are taken into account. The relation between the strain rate and the internal torque in equilibrium is used for typically at least three different strain rates. Equations 2.11 until 2.13 show how the exponential relation between shear strain and internal torque can be used to find the exponent n . C refers to a constant.

$$\sigma \propto \tau \quad (\text{Eq. 2.10})$$

$$\dot{\gamma}_r \propto \tau^n \quad (\text{Eq. 2.11})$$

$$\ln \dot{\gamma} = n \ln \tau + C \quad (\text{Eq. 2.12})$$

$$n = \frac{\Delta \ln \dot{\gamma}}{\Delta \ln \tau} \quad (\text{Eq. 2.13})$$

The obtained n allows for the correlation between internal torque measured in the experiment to the shear stress. The obtained n values of these series (P1668, P1669, P1670, P1671, P1672) was determined with stepping strain rate experiments that directly followed the deformation, hence there is a unique value for each experiment. For the experiments performed by S. Misra (P1129, P1084) the determination of n was done in a different manner. The stepping strain rate experiment was done in a separate experiment. Therefore it yielded one value that was used for several experiments.

2.2.6 Correction for the strength iron jacket

The sample is enveloped by the iron jacket and the strength of the latter will inescapably also take up some of the torque (Barnhoorn, 2004). Barnhoorn (2004) corrected for the strength of the jacket with respect to the sample and found that at 727 °C with a similar iron jacket, the latter took up 1 % of the

sample strength. There are however some differences between his experiments and ours that need to be taken into account.

The experiments of Barnhoorn (2004) were performed on Carrara marble. At 727 °C the peak shear stress of this sample goes up to around 50 MPa. As will be shown in the results section the shear stress of the metapelitic samples at similar temperature typically go up to 120 MPa or higher. This means that the metapelitic sample is even stronger than the Carrara marble and this can only diminish the importance of the strength of the Jacket. Furthermore, the strains in the Barnhoorn *et al.* (2004) paper are of the same magnitude which increases its comparability. The temperatures of our experiments are with 750°C only slightly above 727 °C and Barnhoorn *et al.* (2004) have shown a decrease in strength of the jacket with increasing temperature. As our temperatures are above this point we can even assume a diminished effect of the strength of the jacket. Hence it is assumed that the strength of the jacket is less than 1 % and therefore negligible taking into account the other imprecision of the total experiment.

2.3 Post-deformation analysis

2.3.1 Microstructural and textural analysis: SEM and FIB-SEM

2.3.1.1 Preparation samples for SEM and FIB-SEM imaging

In order to perform SEM imaging the deformed samples required further treatment.

1. The sample is separated from the assembly and subsequently sawn in half along the length of the sample. The latter is still enveloped in the swaged part of the jacket. The first half is designated for SEM and FIB-SEM imaging and the second half for chemical analysis.
2. The iron on the outer rim of the sample is removed by polishing in order to expose the surface of maximum strain for imaging.
3. To avoid the presence of pores the sample is firstly submerged the epoxy resin *Laromin Hardner* and then vacuum pumped. In order to fit the sample size of the SEM a tablet of plastic with the name *Specifast* by *Struers* was created.
4. The samples within the tablets were polished gradationally up to 1 µm with diamond polishing. The latter process removes scratches and smoothes the surface: enhancing the SEM resolution. The loss of material was kept at a minimum but notwithstanding cannot be determined. Therefore it will be assumed to be negligible.
5. The tablets were carbon coated to increase conductivity.

6. The tablets were mounted on a pin and a line of conducting silver paint was drawn between the sample and the metal pin in order to ensure the conductance of electrons and to avoid charging of the sample.
7. To avoid any types of contamination of dirt onto the samples the latter were cleaned by pure nitrogen gas before being inserted into the SEM-vacuum chamber.

2.3.1.2 SEM imaging

The scanning electron microscope (SEM) is an instrument based on the interaction of a focused electron beam with a sample. This interaction results in the production of secondary electrons (SE) or backscattered electrons (BSE). The SE mode can be used when the focus lies on the establishment of the topography while the BSE mode can be used when the focus lies on the compositional differences (i.e. differences in atomic number) in the sample. The heavier the atomic number, the more interaction hence the higher the brightness (Reed, 2005). The BSE mode is therefore more relevant for our research goals.

The SEM is composed of the following elements (1) a source of electrons or an electron gun, (2) lenses that focus the electron beam, (3) facilities to raster the electron beam, (4) detectors for the BSE and SE and lastly (5) computer screens to visualize the output of the detectors (Reed, 2005).

In this project the SEM FEI Quanta 200 FEG of the Electron Microscopy ETH Zürich center (EMEZ) was used. The SE mode was used to focus on the sample and BSE for imaging of the sample. For that we used a beam strength of 10 KeV and spot 5.

2.3.1.3 FIB-SEM imaging

The combination of focused ion beam-scanning electron microscopy (FIB-SEM) can be used to attain tomographic (3D) images of a wide range of samples on a micro to nano scale by the means of ion milling. The FIB-SEM in this project is used to create three-dimensional (3D) images of the melt or shear bands in the deformed samples. The focused ion beam (FIB) makes a cross-section and the scanning electron microscope (SEM) makes an image of this cross-section in secondary electrons (SE) or backscattered electrons (BSE). This provides imaging in the XY plane. Subsequently the FIB removes a thin slice and then SEM is used to image into the depth or Z plane of the sample (De Winter *et al.*, 2009). This method is inherently destructive because it removes the sample (milling). In Figure 2.4 after De Winter *et al.* (2009) this process is clearly illustrated. In Figure 2.5 a schematic overview is given of the orientation of the focused ion beam that uses gallium ions and the SEM (De Winter *et al.*, 2011).

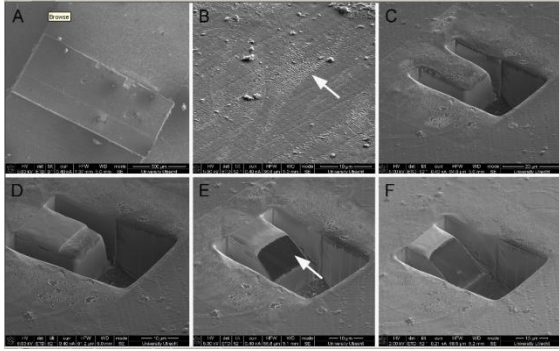


Figure 2.4 FIB milling. These images are made in SE and going from A to F it shows the preparation of the FIB-SEM tomography (De Winter *et al.*, 2009).

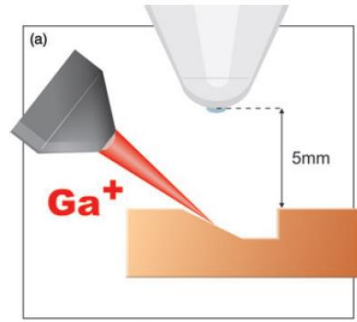


Figure 2.5 Set-up of the FIB-SEM tomography. There is a 52° angle with respect to the samples surface normal (De Winter *et al.*, 2011).

In this project the Zeiss NVision 40 FIB-SEM of the EMEZ was used. Due to material constraints the milled area was roughly in the height, width and depth direction respectively approximately 15, 20 and 20 μm . The milling current was 30 KV: 700 pA and the dwell time and milling resolution were set to automatic.

Before the milling process started an extra patch of carbon was deposited on the sample in order to enhance conduction. Similarly to Winter *et al.* (2009) the area surrounding the intended measured material was milled away (Figure 2.6). Two main detection modes were used (1) ESB and (2) SE2. The ESB is the Zeiss name for Energy Selective Backscattered electron detector to record backscattered electrons. SE2 is the Zeiss name for the Everhart-Thornley detector to record secondary electrons.

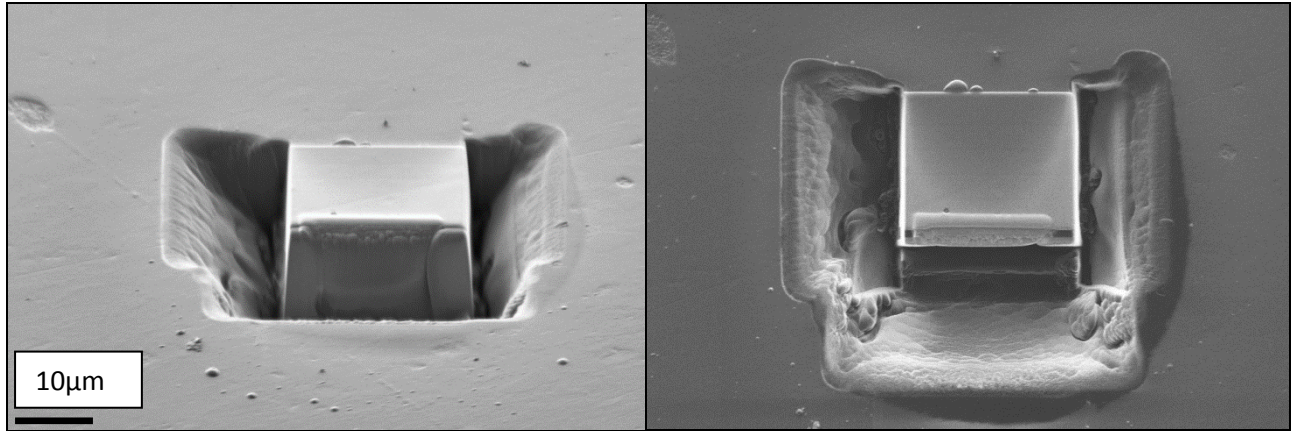


Figure 2.6 FIB-SEM milled section on sample P1129 (a) at an angle and (b) perpendicular to the surface. The detector mode is SE2. Scale is constant for both images.

2.3.2 X-Ray Diffraction (XRD)

The purpose of using X-ray powder diffraction (XRD) is to identify new minerals if those formed after deformation and also to reconfirm the original mineralogy of the samples. The XRD instrument of the Geochemistry and Petrology department of the ETH Zürich was used. The instrument is type D8 Advance Bruker AXS and is equipped with a Lynxeye detector. The diffraction patterns were measured between 5° and 90° 2θ with a step size of 0.02 degrees while the samples were rotated.

To prepare for the analysis a part of the second half of the deformed samples was grinded to powder with a chisel. The resulting material was placed on an XRD disk for analysis. The grain size of the powder still exceeds the size of the minerals which allows for the chemical analysis non-withstanding the size reduction of the sample. The diffraction patterns were corrected for the background noise and minerals were identified by using the International Centre for Diffraction Data (ICDD) database.

2.3.3 Electron Probe Micro Analysis (EPMA)

Electron Probe Micro Analysis (EPMA) was carried out on several deformed samples in order to constrain the melt composition. The instrument in full is the Jeol JXA-8200 superprobe of the Earth Sciences department of the ETH Zürich. The electron current of the beam was 15.2 mA and the voltage 15 kV. EPMA uses a technique that is closely related to that of the SEM. It is non-destructive and can both image and chemically analyse prepared samples. X-rays are excited as a result of interaction of a focused electron beam with the sample and they can be used for chemical characterization of the sample. The spectrum of the emitted X-rays contains lines that are characteristics of the elements present in the sample. The X-rays can be either collected by wave-length spectrometry (WDS) or by energy dispersive X-ray spectroscopy (EDS). The former is used because it has a higher X-ray peak resolution in spite of the slower acquisition rate. It is based on Bragg diffraction due to crystal lattice (Reed, 2005). The beam spot size of the electron beam is 2 μm there is an interaction cone below the beam spot exceeding this 2 μm in width. This size is limiting for the accuracy of the measurement.

Because the initial elemental composition was well constrained the detectors were set to detect Si, Na, Ca, Ti, Mn, Al, Mg, Cr, K and Fe in that sequence. No additional preparation was needed beside that already done for SEM.

2.3.4 Thermogravimetric Analysis (TGA)

The goal of the Thermogravimetric Analysis (TGA) is to see how much water is contained in the undeformed and deformed samples and to see how that is related to melt formation. The difference between the loss of water of the undeformed versus the deformed samples can give us information about the loss of water during melting.

During TGA analysis a sample is heated with a constant heating rate at room pressure while the mass of the sample is also measured. There are more possibilities to vary the temperature but they will not be discussed as they bear no relevance to our research goals. The results are plotted with mass percentage versus the temperature (TGA curve) (Gabbott, 2008).

The measured change in mass of the sample can be due to several factors as described by Gabbott (2008) beside the loss of volatile constituents such as water metals can for instance also be oxidized or decarboxylation can occur. However taking into account the composition of our samples we exclude the latter effects. Weight loss can be explained by the loss of atmospheric humidity trapped in the sample and the loss of water from the muscovite minerals and possibly the hydrated melt (Gabbott, 2008).

Chapter 3. Results

In this chapter the main results of the deformation experiments and the analytical methods are shown. The goal of this project is to see how partial melting and localisation as functions of composition, strain rate and final strain in synthetic metapelites. Because two compositions were used to answer this question this chapter is split up in three parts (1) a general overview (2) 70% quartz and 30% muscovite and (3) 30% quartz and 70% muscovite. Previous experiments performed by Dr. E. Tumarkina and Dr. S. Misra have been included in the overview because they complement the variation matrices. Only the main results will be shown, the appendices contain the more detailed data files.

3.1 General overview both compositions

3.1.1 General overview deformation experiments

In Table 3.1 below an overview of the deformation experiments performed in this study is given. All experiments were performed at 750 °C and 300 MPa.

Table 3. 1 Overview of the deformation experiments. “-” denotes an unknown quantity or variable.

| Experiment | Sample length (mm) | Sample diameter (mm) | Sample type Q: M | Shear Strain rate ($\dot{\gamma}$) s ⁻¹ | Finite shear (γ) | Yield-peak (MPa) | Rate of weakening (qualitative) |
|--------------------|--------------------|----------------------|------------------|--|---------------------------|------------------|---------------------------------|
| P1084 ¹ | - | - | 30:70 | 3·10 ⁻⁴ | 1.08 | 105 | slow |
| P1129 ² | - | - | 30:70 | 3·10 ⁻⁴ | 2.73 | 111 | slow |
| P1668 | 5.87 | 9.91 | 30:70 | 1·10 ⁻⁴ | 0.90 | 98 | fast |
| P1669 | 5.74 | 9.87 | 70:30 | 1·10 ⁻⁴ | 0.95 | 129 | - |
| P1670 | 7.73 | 9.99 | 30:70 | 1·10 ⁻⁴ | 2.92 | 96 | fast |
| P1671 ³ | 7.23 | 9.82 | 70:30 | 1·10 ⁻⁴ | 2.40 | 145 | very fast |
| P1672 | 7.46 | 9.88 | 70:30 | 3·10 ⁻⁴ | 2.98 | 148 | very slow |
| P1673 ⁴ | 6.87 | 9.85 | 70:30 | 1·10 ⁻⁴ | 1.20 | 112 | very fast |

¹ Experiment performed by Dr. E. Tumarkina and Dr. S. Misra, 2012

² Experiment performed by Dr. E. Tumarkina and Dr. S. Misra, 2012

³ Slip occurred in the jacket assembly during the experiment: results may be compromised.

⁴ Slip occurred in the jacket assembly during the experiment: results may be compromised.

3.1.2 General overview undeformed samples

The undeformed quartz-rich and muscovite-rich samples also have been imaged by S. Misra (p.c.) in SEM BSE (Figure 3.1). It is necessary to show these images in order to be able to distinguish between original features and deformation-induced features. From the images the following can be observed:

1. There is a foliation present made up by elongated slivers of muscovite.
2. Porosity is present (12-15% after Misra et al, 2009).
3. Quartz grains are mainly angular.

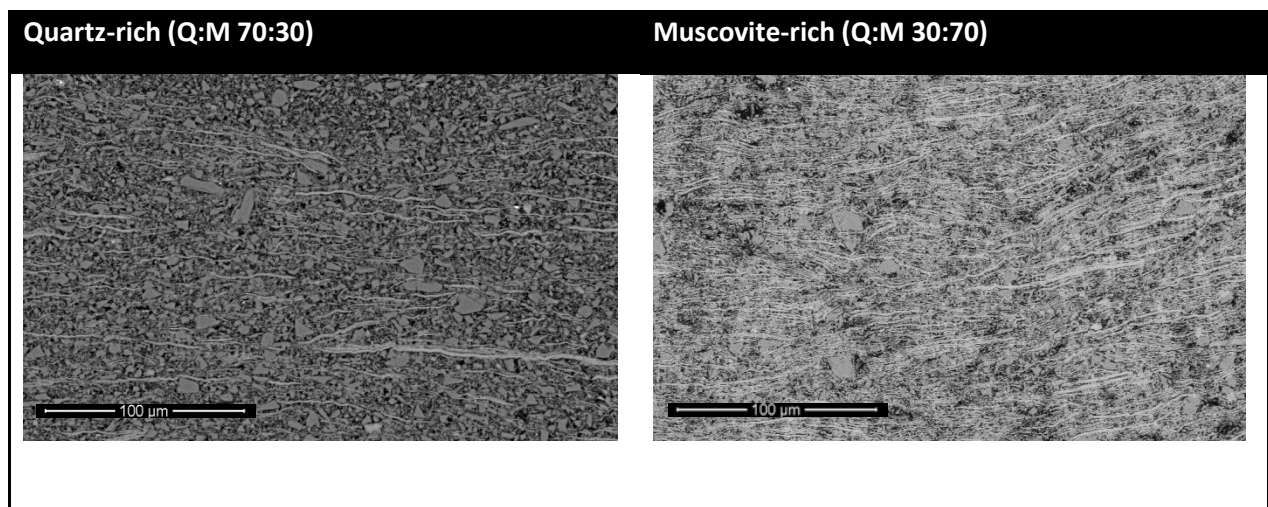


Figure 3.1 Undeformed samples, quartz-rich and muscovite-rich. Courtesy of S. Misra, 2009

3.1.3 General overview localisation features of both compositions

In Figure 3.2 a representative overview is given of the different localisation features of the deformed samples with their most striking characteristics in SEM BSE.

| P1084 S16, $\gamma \sim 1$, $\dot{\gamma} = 3e-4 \text{ s}^{-1}$, 1 hour | P1129 S15 $\gamma \sim 3$, $\dot{\gamma} = 3e-4 \text{ s}^{-1}$, 3 hours | P1668 S16, $\gamma \sim 1$, $\dot{\gamma} = 1e-4 \text{ s}^{-1}$, 3 hours | P1669 S14, $\gamma \sim 1$, $\dot{\gamma} = 1e-4 \text{ s}^{-1}$, 3 hours | P1670 S16, $\gamma \sim 3$, $\dot{\gamma} = 1e-4 \text{ s}^{-1}$, 9 hours | P1671 S14, $\gamma \sim 1$, $\dot{\gamma} = 1e-4 \text{ s}^{-1}$, 9 hours | P1672 S14, $\gamma \sim 1-2$, $\dot{\gamma} = 3e-4 \text{ s}^{-1}$, 3 hours | P1673 S14, $\gamma \sim 1$, $\dot{\gamma} = 1e-4 \text{ s}^{-1}$, 6 hours |
|--|--|--|---|--|--|---|---|
| | | | | | | | |
| 1. Foliation at ~ 45 degrees to shear direction 2. no localisation | 1. Idem 2. shear bands (s.b.) of a few μm thick 3. Melt with new minerals | 1. Idem 2. No s.b. 3. Brittle quartz dominant. Most likely formed post-deformation | 1. Idem 2. High strain zones 3. Brittle/ductile behaviour | 1. Idem 2. melt-filled bands, 2-10 μm thick. Short and discontinuous | 1. Idem 2. Broad bands of higher strain ($\sim 10\mu\text{m}$) with black spots | 1. Idem 2. Very wide shear band ($\sim 25\mu\text{m}$) and thinner ones 3. Only ductile behaviour | 1. Idem 2. Lack of clear localisation |

Figure 3.2 representative overview of the deformed samples in SEM BSE. The red arrow indicates foliation, the blue the direction of shear bands (if present) and the green arrow the shear direction. Dark gray grains are quartz, light gray is muscovite and intermediate colour is melt (in P1670 and P1129). Scale is constant for all images. The abbreviation “s.b.” refers to shear band. Finite strain is denoted by “ γ ” and strain rate by “ $\dot{\gamma}$ ”.

3.1.4 Classification localisation

Based on these BSE images we subdivide the bands into five categories, as can be seen in Table 3.2 below.

Table 3.2 Different types of shear bands

| Type of shear band | Samples |
|--|---------------------|
| Melt filled band | P1129, P1670 |
| Grain size reduction and melt (river bed) | P1672 |
| Transitional behaviour (ductile muscovite, brittle quartz) | P1669, P1671, P1673 |
| Purely brittle behaviour | P1668 |
| No localisation | P1084 |

3.2 Deformation and analysis of quartz-rich samples

For a constant composition of a quartz:muscovite volume ratio of 70:30 the strain rate and the finite strain are varied. Below in Table 3.3 the variation matrix of the different experiments is displayed.

Table 3.3 Matrix of variable strain rate and finite strain for quartz:muscovite volume ratio 70:30

| quartz:muscovite 70:30 (sample 14) | Finite strain $\gamma \sim 1$ | Finite strain $\gamma \sim 3$ |
|--|---|-------------------------------|
| Strain rate $\dot{\gamma} 1e-4 \text{ s}^{-1}$ | P1669 ($\gamma = 0.95$) P1673 ($\gamma = 1.2$) | P1671 ($\gamma = 2.4$) |
| Strain rate $\dot{\gamma} 3e-4 \text{ s}^{-1}$ | Failed | P1672 ($\gamma = 2.98$) |

In Figure 3.3 the images of the deformed samples are shown while they were still in the assembly. It is of importance to assess these images in order to (1) reconfirm the quantity of strain the sample underwent and (2) see whether any damages could have interfered with the experimental data. In P1671 and P1673 slip on the jacket occurred which may compromise the results.

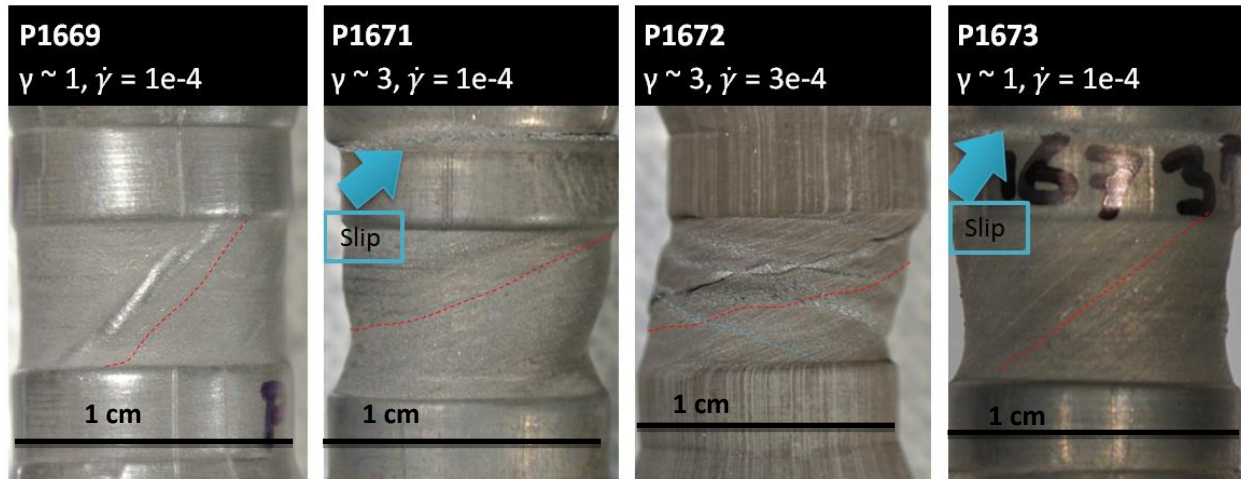


Figure 3.3 Deformed samples of the quartz-rich series. Sense of shear is dextral and the width of the spacer is 1 cm in all images. The abbreviation γ is for finite strain and $\dot{\gamma}$ for finite strain in s^{-1} . The striped red line indicates the path of the passive strain marker (vertical before experiment), the striped blue line indicates the direction of shear bands and the black line is 1 cm for scale. Note that slip on the jacket occurred in experiment P1671 and P1673.

3.2.1 Mechanical data

3.2.1.1 Stepping Strain Rate experiments (SSR)

As explained in the Chapter 2 on Materials and Methods, the Stepping Strain Rate experiments (SSR) are used to find the power law exponent using equations 2.10 through 2.13. The resulting value of n is used in equation 2.8 to find the Internal Torque (M) to shear stress. The details of these calculations can be found in Appendix C. In Figure 3.4 an overview of the data and values is displayed. In not all experiments the SSR could be performed due to experimental complications.

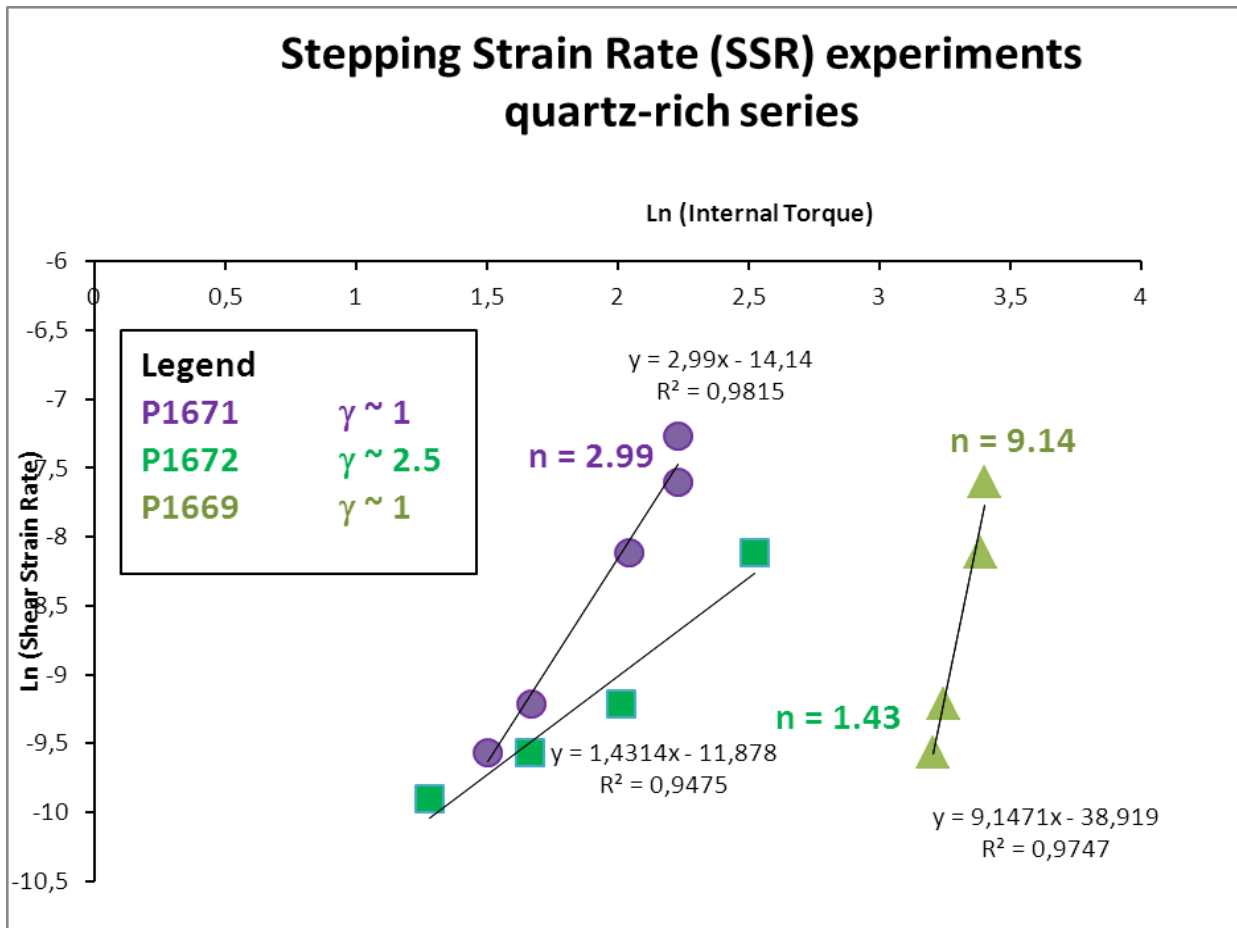


Figure 3.4 Stepping Strain Rate (SSR) experiments quartz-rich series (Q:M 70:30).

3.2.1.2 Shear Stress vs. Shear Strain

Figure 3.5 below shows the relation between shear stress and shear strain. The equations 2.8 and 2.9 were used to convert the internal torque measured by the Paterson Rig to shear stress and the shear strain was found using equation 2.6. During experiment P1671 there were problems with pressurization at a later stage: pressure was lost after the finite strain $\sim 1,5$. To be able to continue the vessel was “instantaneously” pressurized twice at $\gamma \sim 2,0$ and $\gamma \sim 2,6$.

The following can be observed from the Shear stress vs. Shear strain in Figure 3.5:

1. There is an elastic range (linear part) of deformation that is almost identical for all experiments up to shear strains of ~ 0.025
2. Then strain hardening occurs in from ~ 0.025 onwards. The extent to which this occurs varies per experiment. Higher strain rate experiments go up to higher shear stresses during strain hardening than experiments with a low strain rate.
3. After the peak in shear stress (yield-peak) it starts to decrease with increasing finite strain. It decreases faster in experiments with lower strain rate and slower in experiments with faster strain rate.
 - In the case of low strain rate (P1671) the shear stress drops to a minimum and stays at that constant value (~ 20 MPa).
 - In the case of higher strain rate the localisation (P1672) is slower and does not reach an equilibrium shear stress (yet).
4. The pressurisation that was performed twice in experiment P1671 is expressed in the instantaneous drops in shear stress during the experiment after strain ~ 2 and $\sim 2,6$.
5. The paths the low strain rate experiments follow is quite similar except when there is a specific instantaneous aberration deviating from the smooth curve. From this we can deduce that (1) the experiments are quite reproducible and that (2) if there is an aberration in the experiment it can be easily seen in the shear stress vs. strain curve and hence can be corrected for. The aberrations (P1671, P1673) are most likely due to slipping along the jacket, as has been confirmed by the photographs of the experiments

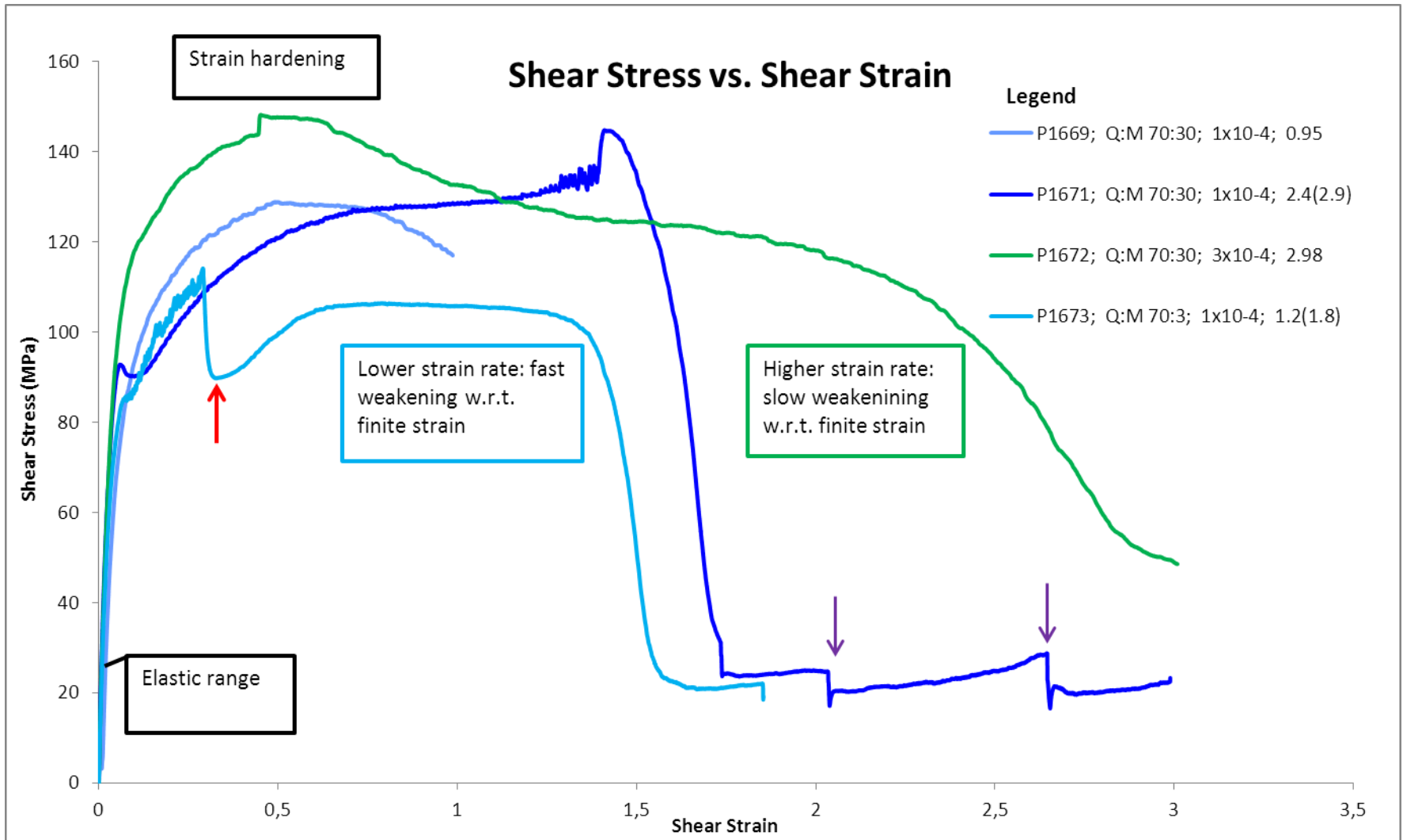


Figure 3.5 Shear Stress vs. Shear Strain of the quartz-rich sample. The finite strain values in the legend refer to the actual strain values reconfirmed by the passive strain markers and the values in between brackets refer to the values the finite strain should have had. The curves have been corrected for the initial torque and the initial rotation that were present before the experiment started. Red arrow indicates malfunction (slip on jacket) within the experiment. Purple arrows point to the moment pressure was increased as it was slowly dropping during the experiment. The abbreviation “w.r.t.” is short for “with respect to”.

3.2.2 SEM Images quartz-rich samples

In Figures 3.6 and 3.7 an overview of representative SEM BSE images of the quartz-rich series are shown in the variation matrix. Below we digress on the microstructures and specifically the localisation microstructures

For **low finite strain (γ) and low strain rate ($\dot{\gamma}$)** (P1669) there is both brittle and ductile localisation behaviour present in the low angle Riedel shear direction. Quartz is fractured throughout the sample, whilst muscovite is not. In the shear zone the muscovite curves into the shear zone, indicating a syn-deformation origin of the feature. In the areas of brittle fault localisation grain size reduction occurs. There is no visible evidence for melt. The black spaces between the quartz grains and muscovite are equally distributed though the sample. These are most likely voids that have been filled up with resin glue former porosities during the sample preparation. The foliation is tilted about 45° from the original vertical orientation. The mechanical data has shown a decrease in shear stress after $\gamma \sim 0.5$. On the P1669 image in Figure 3.6 there is a fracture in the lower left corners which cross-cuts the structures that are present: this fracture likely occurred after the experiment. The microstructures another low γ and low $\dot{\gamma}$ (P1673) in this section are not taken into account because of the evidence of slip on the jacket and in the shear stress curve (large instantaneous decrease in shear stress at $\gamma \sim 0.3$). Compared to the undeformed sample the muscovite is more aligned and more “diffuse” i.e. it is not a distinct sliver with straight boundaries but rather has a more serrated boundary.

In the experiment with **high γ and low $\dot{\gamma}$** (P1671) very different microstructures are visible. This experiment is compromised because evidence on the jacket and the shear stress curve also indicate slip within the assembly. As a consequence, the comparison between P1669 and P1671 in the variation matrix is not valid. There is no clear evidence of pronounced localisation: the muscovite slivers appear to be continuous. In some but not all areas the muscovite slivers are more curved. There are hints that the bands of black dots are aligned in the low angle Riedel shear direction but this behaviour is not ubiquitous. The black dots could be former porosities now filled by the glue as well. This could be evidence for a dilatant shear zone. The foliation is also tilted about 45° from the original vertical orientation. On a smaller scale it is visible that new minerals have formed of $1-3 \mu\text{m}$ in size.

In the **high γ and high $\dot{\gamma}$** (P1672) experiment the shear zones bear similarities to P1669 namely: (1) the shear bands occur in similar spacings and (2) there is evidence of grain size reduction (small quartz grains distinguishable). There are also marked differences: (1) melt is present and (2) melt zones are

wider in P1672 than P1669. However, there are also thinner zones of localised shear and melt in P1672, such as in the lower left corner of P1672 in Figure 3.6 below. Lastly, in P1672 (3) microlithons are present in the wide shear zones (~50 μm). These microlithons are less strongly deformed. The foliation is in roughly the same orientation as the previous samples. Due to the experimental complications of jacket-slipping in P1671, the latter and P1672 cannot be compared effectively.

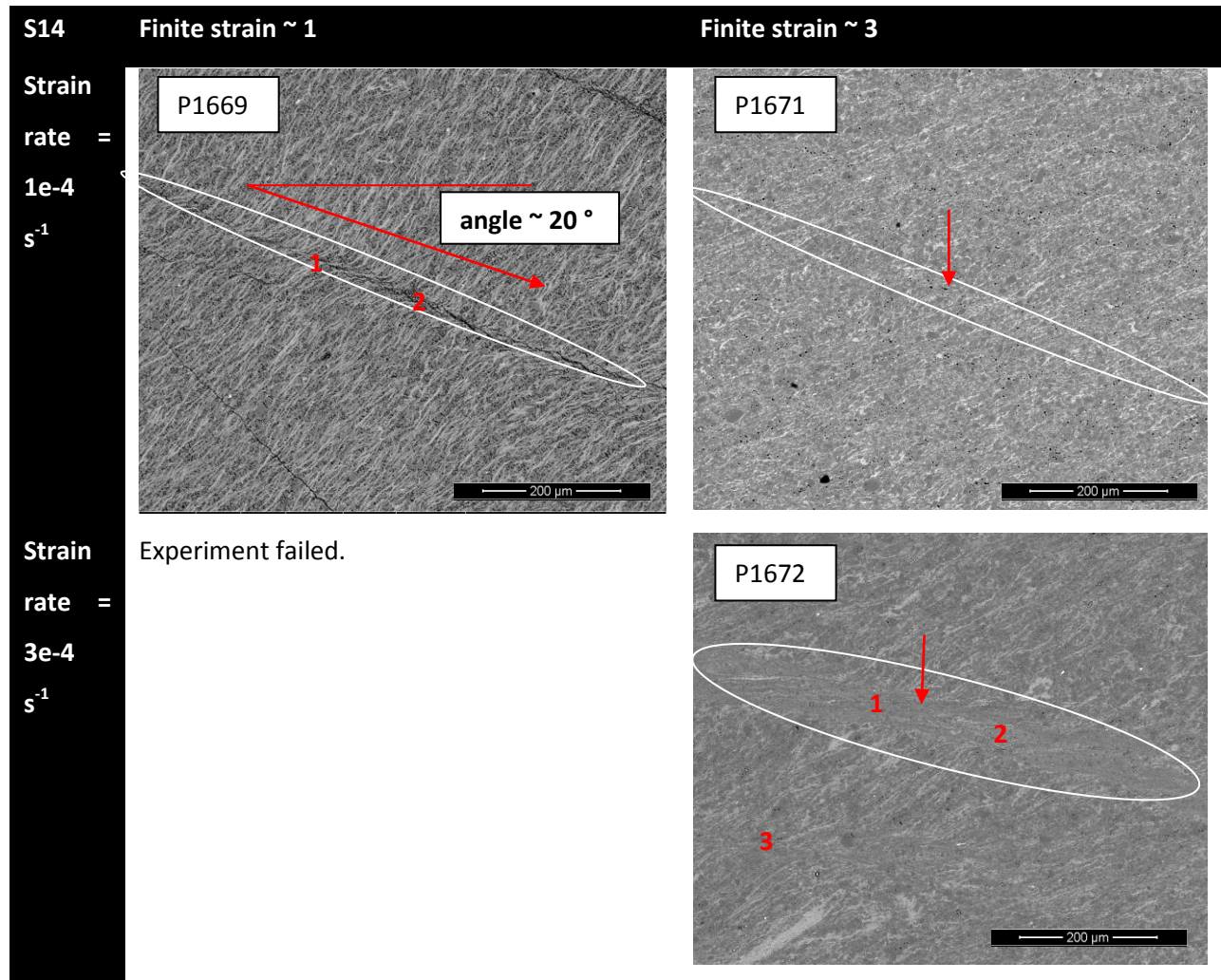


Figure 3.6 Overview of quartz-rich samples (S14) all at the same magnification. Scale is 200 μm . Image in SEM BSE. Light gray indicates muscovite, darker gray quartz and black are fractures or porosities. The intensity of the gray-scale is variable per image because the optimal settings of the SEM are variable. Areas of localised shear are marked with the white oval shape. The angle of the localisation bands is roughly 20° to the shear direction: confirming that the direction of the shear zones are low angle Riedel shears. For P1669 the numbers 1 and 2 indicate respectively an area of ductile deformation with muscovite curving towards the zone and a brittle area with grain size reduction. In P1671 the red arrow points to the porosity. In P1672 number 1 refers indicates a wide shear band, 2 a microlithon within the wide shear band and 3 a smaller shear band. Arrow points to grain size-reduced ($\sim 10\times$) and possibly rotated quartz clast.

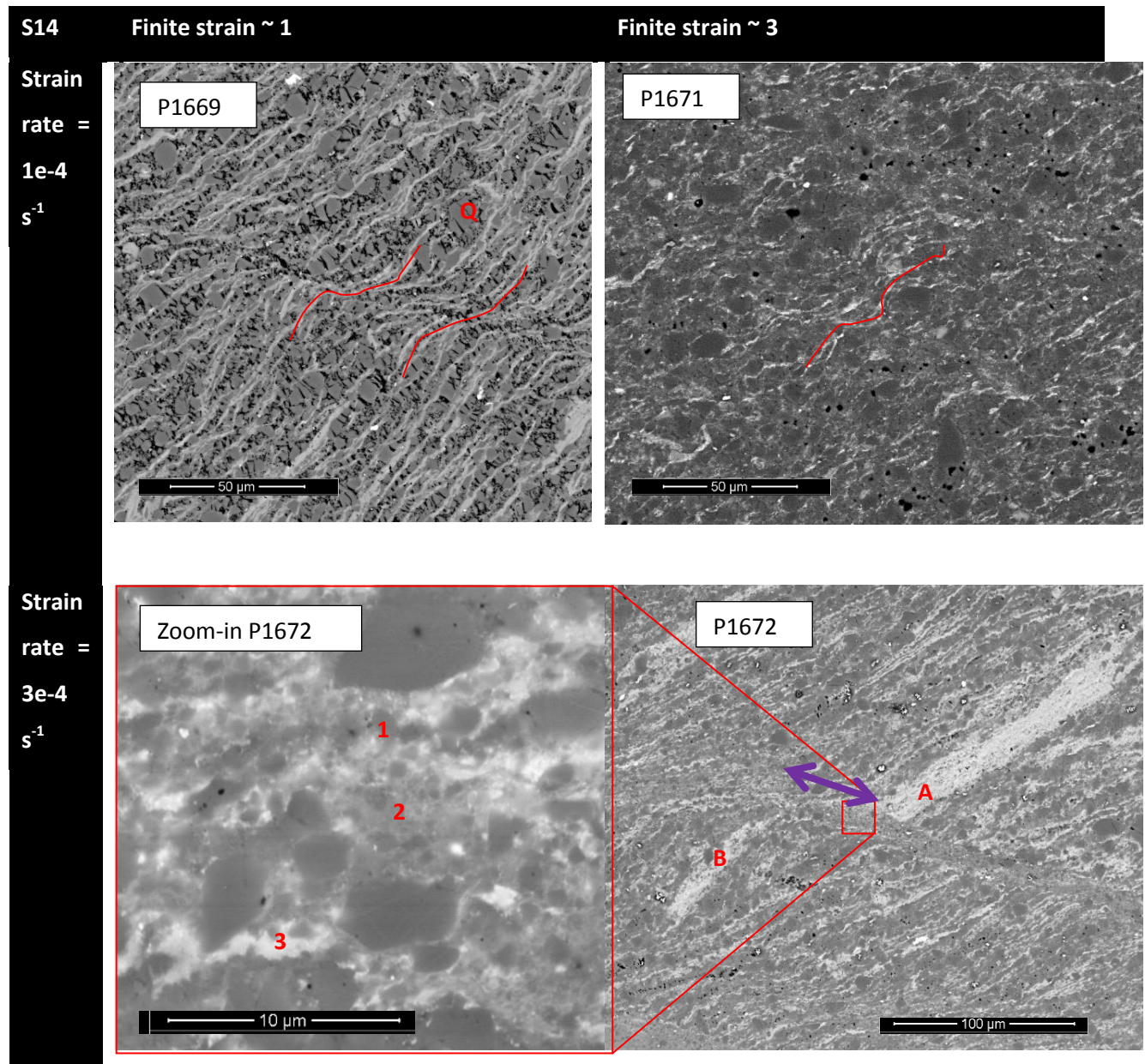


Figure 3.7 Overview of zoom-ins quartz-rich samples (S14) in SEM BSE. Note: scale is not constant, and the lower left quadrant is filled with a blow-up of a localisation band of P1672 (red box). Light gray indicates muscovite, darker gray quartz and black are fractures or porosities. The intensity of the gray-scale is variable per image because the optimal settings of the SEM are variable. P1669 Ductile muscovite (red curving line) with brittle quartz (red letter Q). P1671 red sliver indicating curved muscovite. P1672 shear band with wide muscovite block (parts A and B) as passive strain marker (purple arrow) indication a movement of $\sim 50 \mu\text{m}$. In lower left quadrant blow-up showing (1) grain size reduced quartz grains (2) melt and (3) broken up muscovite

3.2.4 X-ray Diffraction (XRD)

The purpose of using X-ray diffraction (XRD) is to identify new minerals if those formed after deformation and also to reconfirm the original mineralogy of the samples. The bimodal composition of the initial sample 14 was confirmed. There was no significant new signal (i.e. non quartz or muscovite peak) in the samples P1669, P1671 or P1672. The complete overview of the results is given in Appendix A. As a side note it is necessary to mention that the material used for his experiment was taken from one half of the deformed samples, so along the entire radius of the sample (i.e. not just the outside rim). As the deformation increases with increasing radius we have a moderately diluted signal of the deformation. As a consequence we can establish the presence of new minerals but we cannot say anything about their absolute quantity.

3.2.5 Electron Probe Micro Analysis (EPMA)

Microprobe analyses were carried in order to constrain the melt composition in the melt bands. Within this series there were no large melt-pockets in P1669, P1671 and P1673 and therefore these samples were omitted in the EMPA analyses. Only in P1672 there are shear zones with suspected melt between grain size reduced grains (Figures 3.6 and 3.7). An overview of this series can be found in Table 3.4 below.

The chemical measuring tools of the microprobe include taking point measurements (beam size 2 μm), elemental maps and line measurements (step size in this case 2 μm). The beam size of the probe implicates a practical limitation for this work. The melt-filled shear bands are generally only 2 μm thick with the exception of P1670 (muscovite rich, high strain). Therefore point measurements are usually not worthwhile. In an attempt to circumvent this practicality line measurements were taken of 2 μm step size. These however also did not yield satisfactory results. The detailed data can be found Appendix D.

Table 3.4 Quartz:muscovite 70:30 (sample 14) and presence of melt-filled shear bands (s.b.).

| Quartz:Muscovite 70:30 (sample 14) | Finite strain $\gamma \sim 1$ | Finite strain $\gamma \sim 3$ |
|---|--|-------------------------------|
| Strain rate $\dot{\gamma} 1\text{e-}4 \text{ s}^{-1}$ | P1669 no melt in s.b. P1673 no melt in s.b. | P1671 no melt in s.b. |
| Strain rate $\dot{\gamma} 3\text{e-}4 \text{ s}^{-1}$ | Failed | P1672 some melt in s.b. |

3.2.5 Thermogravimetry Analysis (TGA)

The goal of this method is to assess how much water is present in the initial samples and in the samples after deformation. The difference between these amounts will tell us something about the amount of water released during experiments. In other words, if water was lost from the system during the experiment.

During TGA the sample is heated up to 1400 °C (1673 K) under atmospheric pressure. It is assumed that the muscovite is completely dehydrated. Heating at atmospheric pressure (0,1 MPa) is a major disadvantage if we want to establish the dehydration behaviour of metapelites in the Paterson rig experiments that were performed at 300 MPa. Measuring water loss at elevated temperature and pressure is however experimentally not possible. Therefore we will use the TGA curves as an approximation for the amount of water loss.

There are several assumptions that lie at the basis of using this method. Firstly, one assumes that there is a finite amount of water is present in the original samples. Secondly, that the least strongly energetically bound water evaporates first and then the more strongly bound water later at higher degrees. In other words, first we lose atmospheric water and then water structurally bound in the muscovite. Hence, this amount is and nature of the water is determined by the two dehydration curves of the original samples. Thirdly it is assumed that all structurally bound water has been removed at 1400 °C. Lastly we assume that even though the TGA was done at low pressures the process repeats itself in the same stepwise and quantitative manner at higher confining pressures.

3.2.5.1 TGA Starting materials

In Figure 3.8 the dehydration curves of the two initial samples are shown. There are three striking features in this graph. (1) Sample 14 appears to lose more water than sample 16 while it contains less muscovite and hence less water. (2) There are two step wise kinks in both and (3) the second step in sample 16 is more rapid and larger than that of sample 14. From point 1 we cannot but conclude that the TGA analysis in this case cannot be used quantitatively as the result contradicts known input. However, what can be reliable is the shape in point 3: high muscovite can cause a stronger relative dehydration (~ 3 wt %) rather than low muscovite (~ 2 wt %).

3.2.5.2 TGA Deformed samples

Of the quartz-rich series P1669 and P1672 were measured. The results are shown in Figure 3.9 below. The deformed samples (1) follow roughly the same “2 step” shape as the curve of the starting sample (2) lose less water than the original sample (3) differ less than one percent from another.

Excluding the possibility of quantitative analysis we can say that sample 14 releases significant amounts of water and that the latter implies we are in the wet melting regime. Including the possibility of quantitative analysis we can say that the deformed samples release less water than the original samples.

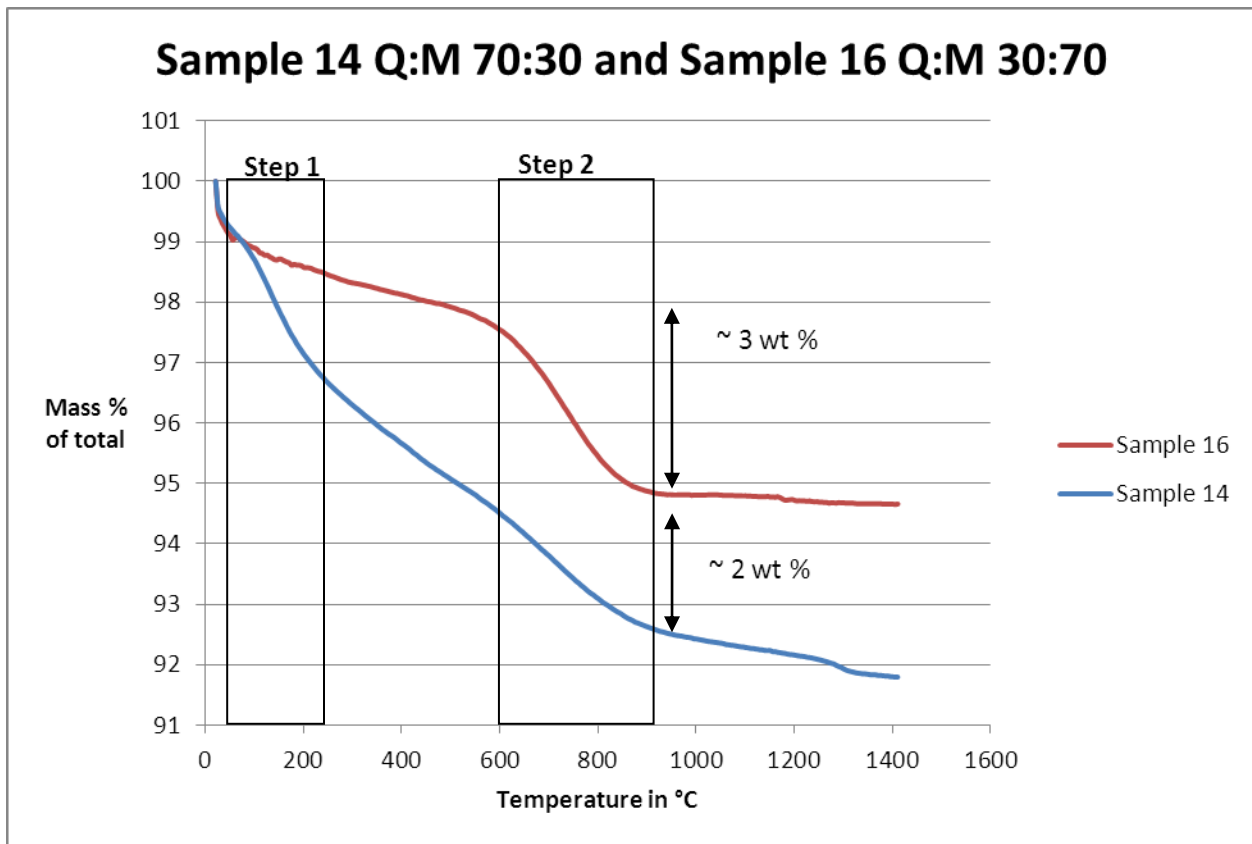


Figure 3.8 TGA Sample 14 Q:M 70:30 and Sample 16 Q:M 30:70. The two steps signify the two periods in increased loss of water from the sample.

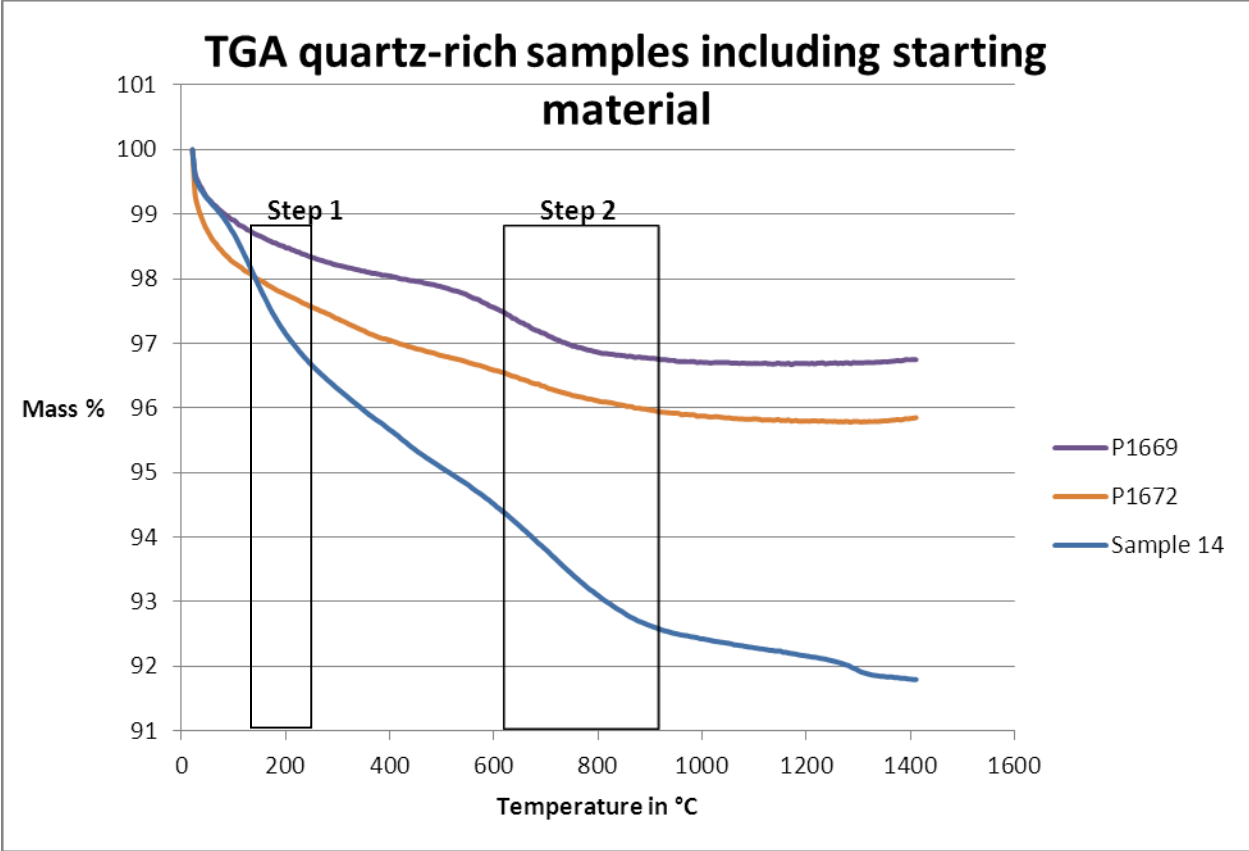


Figure 3.9 TGA undeformed and deformed quartz-rich samples. The two steps signify the two periods in increased loss of water from the sample.

3.3 Deformation and analysis of muscovite-rich samples

For a constant composition of a quartz:muscovite volume ratio of 30:70 the strain rate and the finite strain are varied. Below in Table 3.5 the variation matrix of the different experiments is displayed.

Table 3.5 Matrix of variable strain rate and finite strain for quartz:muscovite volume ratio 30:70.

| quartz:muscovite 30:70 (sample 16) | Finite strain $\gamma \sim 1$ | Finite strain $\gamma \sim 3$ |
|--|--|--|
| Strain rate $\dot{\gamma} 1e-4 \text{ s}^{-1}$ | P1668 ($\gamma = 0.90$) | P1670 ($\gamma = 2.92$) |
| Strain rate $\dot{\gamma} 3e-4 \text{ s}^{-1}$ | P1084 ($\gamma = 1.08$) ⁵ | P1129 ($\gamma = 2.73$) ⁶ |

In Figure 3.10 the images of the deformed samples are shown when they are still in the assembly. There are no images available of P1084 and P1129 performed by Dr. E. Tumarkina and Dr. S. Misra.

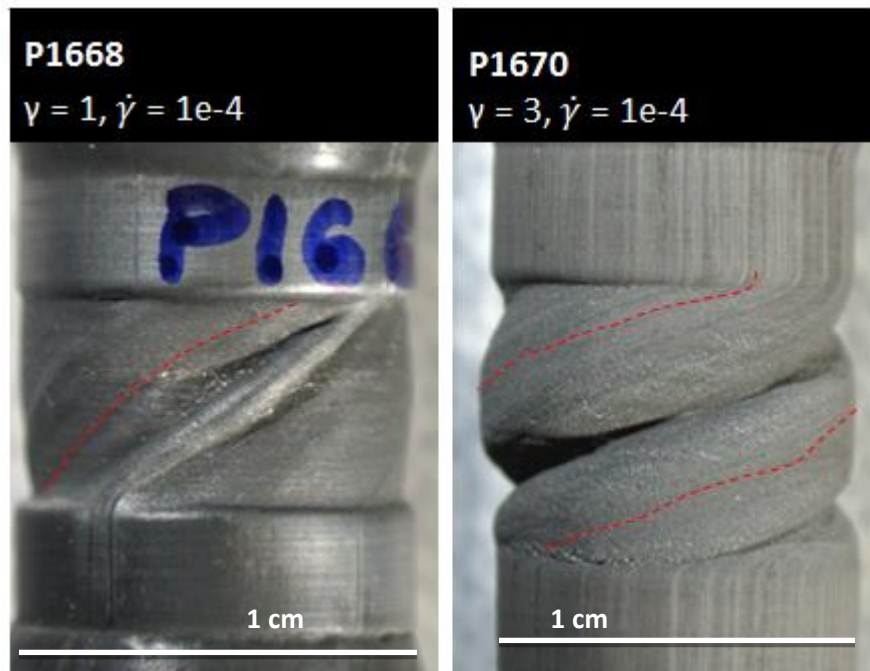


Figure 3.10 Deformed samples of muscovite-rich composition. Yellow arrow indicates the direction of shear, the striped red line indicates the form of passive strain marker, the striped blue line indicated the direction of shear bands and the white line is 1 cm for scale.

⁵ Experiment performed by Dr. E. Tumarkina and Dr. S. Misra, 2012

⁶ Experiment performed by Dr. E. Tumarkina and Dr. S. Misra, 2012

3.3.1 Mechanical data

3.3.1.1 Stepping Strain Rate experiments (SSR)

The results of the muscovite-rich series can be found in Figure 3.11 below. These experiments were performed analogously as described in section 3.2.1.1 and the details of these calculations can be found in Appendix C.

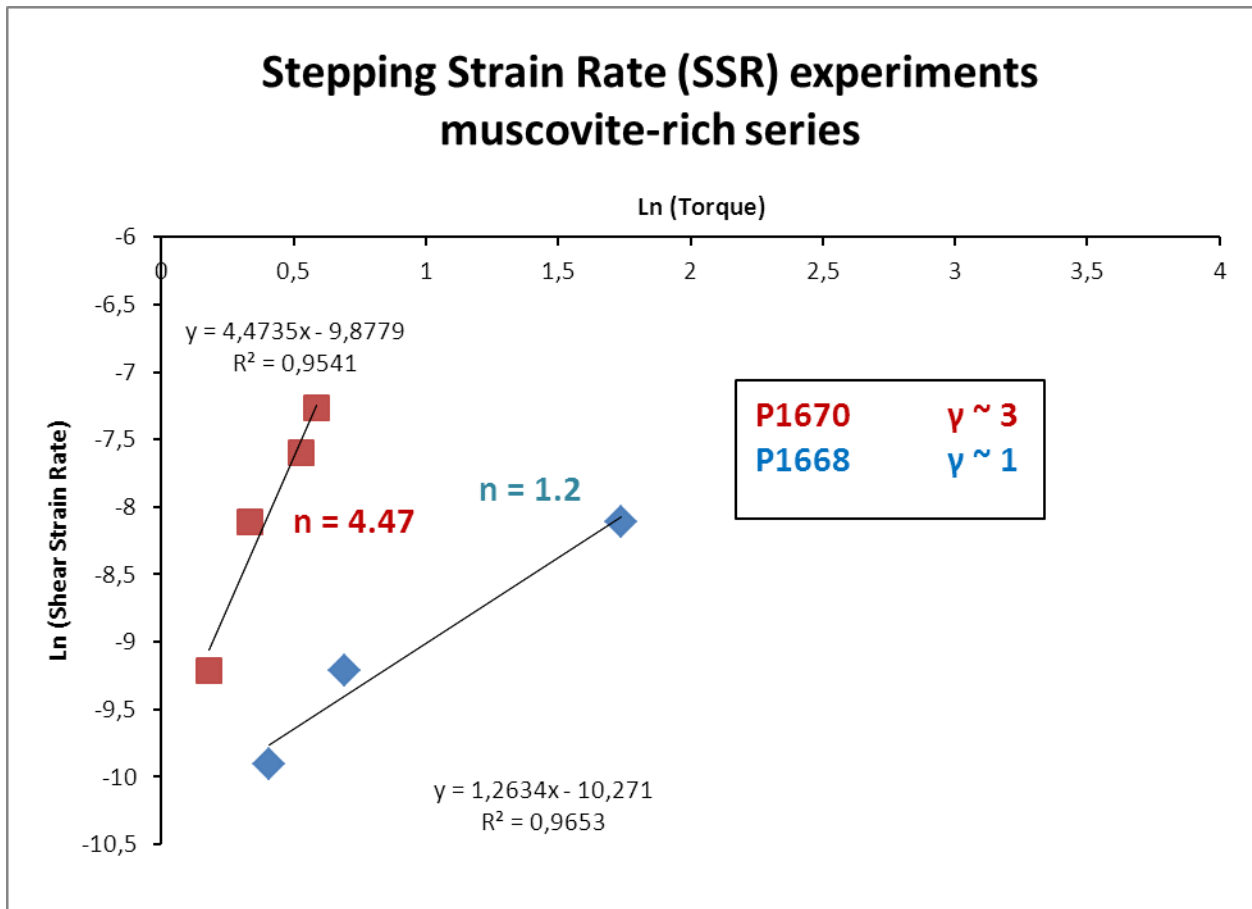


Figure 3.11 Results of Stepping Strain Rate (SSR) experiments muscovite-rich series (Q:M 30:70).

3.3.1.2 Shear Stress vs. Shear Strain

In Figure 3.12 below shows the relation between shear stress and shear strain for the muscovite-rich series, which have been calculated and corrected for initial values analogously to paragraph 3.2.1.2. For samples P1084 and P1129 the n exponent was determined in a separate experiment (same material, P and T) by S. Misra and found to have the value of 5,15. This value was used for both experiments (Misra *et al.*, 2009).

The following things can be observed in Figure 3.12:

1. There is an elastic range (linear part) that is almost identical for all experiments up to shear strains of ~ 0.025 as well.
2. Strain hardening occurs in from ~ 0.025 onwards. The extent to which this occurs varies per experiment. Higher strain rate goes up to higher shear stresses during strain hardening. Lower strain rates experiments go up to lower shear stresses.
3. After the peak in shear stress (yield point, around $\gamma \sim 0.3$) it starts to decrease. In the case of low strain rate the shear stress drops rapidly and decreases slowly from that points onwards to ~ 16 MPa for P1670 and ~ 4 MPa for P1668. In the case of higher strain rate the decrease in shear stress with increasing strain occurs less rapidly.
4. The curves of P1668 and P1670 are very similar which indicates that the experiments are repeatable and dependable. It is visible that there is a malfunction during the deformation of P1084 as the shear stress decreases instantaneously at $\sim 0.1 \gamma$ after which the trend is no longer coupled with that of P1129.

3.3.1.3 Shear Stress vs. Shear Strain both compositions

In Figure 3.13 below shows the relation between shear stress and shear strain of both the metapelitic rocks. The group of blue tones are of the quartz-rich sample 14 and the group of red tones are muscovite-rich sample 16. From this it becomes apparent that the quartz-rich samples can go up to higher shear stresses, localise later and slower when other circumstances are the same.

The following things can be observed in Figure 3.13:

1. Quartz-rich series reach higher shear stresses
2. Quartz-rich series weaken more slowly

3. Quartz-rich series experience more experimental malfunction (slipping of jacket)
4. Muscovite-rich series reach (all else the same) stable shear stress values before quartz does.

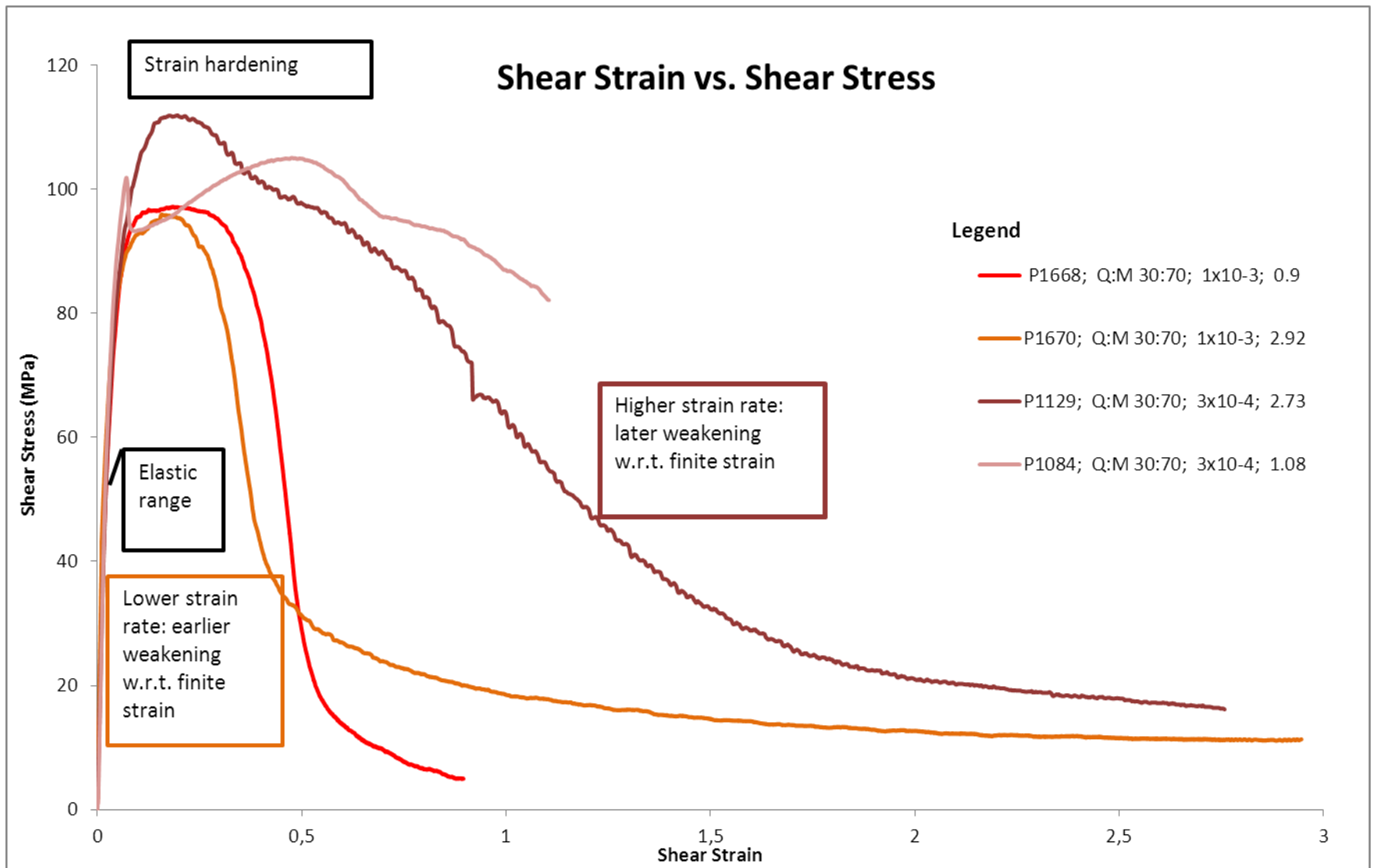


Figure 3.12 Shear Stress vs. Shear Strain of the muscovite-rich sample.

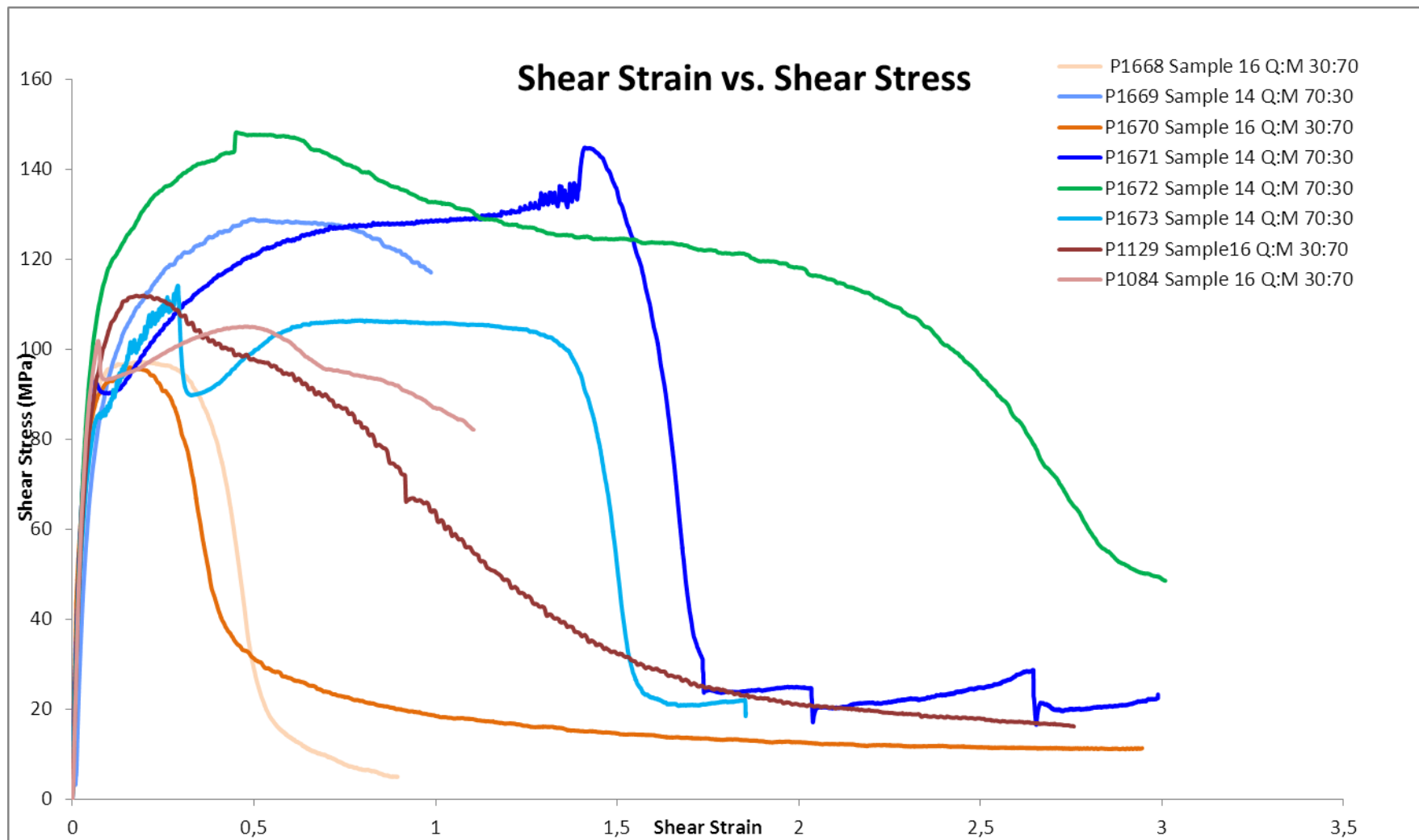


Figure 3.13 Shear Stress vs. Shear Strain in all experiments. Blue colour tones are quartz-dominated samples, the red colour tones are muscovite dominated samples. Quartz-rich group reaches higher shear stresses (yield-peak) and weakens more slowly than the muscovite-rich series.

3.3.2 SEM Images muscovite-rich sample

In Figures 3.14 and 3.15 below an overview of representative images of the muscovite-rich series are shown in the variation matrix. In this paragraph the features in SEM in Back Scattered Electron mode (BSE) of the samples plus their mechanical behaviour will be explored as well.

In sample P1668 with **low finite strain (γ) and low strain rate ($\dot{\gamma}$)** the foliation is tilted about 45°. There are fractures throughout the sample all in the low angle Riedel shear direction (~15 degrees to the shear plane). There are rare possible indications but no ubiquitous evidence of movement along these brittle fractures. The Riedel shear structures are highly similar to the brittle shear localisation behaviour described by Logan (2007) as can be seen in the inset. In the Shear stress vs. Strain curve we do see a strong progressive decline in shear stress at around $\gamma \sim 0.5$. Compared to the original samples (Figure 3.1) the quartz grains have become elongated.

In the case of **low finite strain (γ) and high strain rate ($\dot{\gamma}$)** (P1084) we see no evidence for localisation. The foliation is also tilted about 45°. Compared to the original samples (Figure 3.1) the quartz grains have also become elongated.

For **low finite strain (γ) and high strain rate ($\dot{\gamma}$)** (P1670) the foliation has roughly the same inclination. Shear bands are melt-filled, ~2-10 μm thick, relatively short (~50-150 μm) and poorly connected. They are also in the direction of low angle Riedel shears.

For **high finite strain (γ) and high strain rate ($\dot{\gamma}$)** (P1129) the foliation has again roughly the same inclination. Shear bands are ~2 μm thick, elongate (~150-200 μm), connected and anastomosing. Their direction is roughly in the low angle Riedel shear direction as well. There is no evidence (any more) of brittle behaviour. The difference in the morphology of the two experiments with melt bands (P1670 and P1129) is shown in Figure 3.16 with binary images of the melt bands. The amount of crystals with respect to the amount of melt is much higher in P1129 than in P1670. The duration of the latter is three times longer than the former.

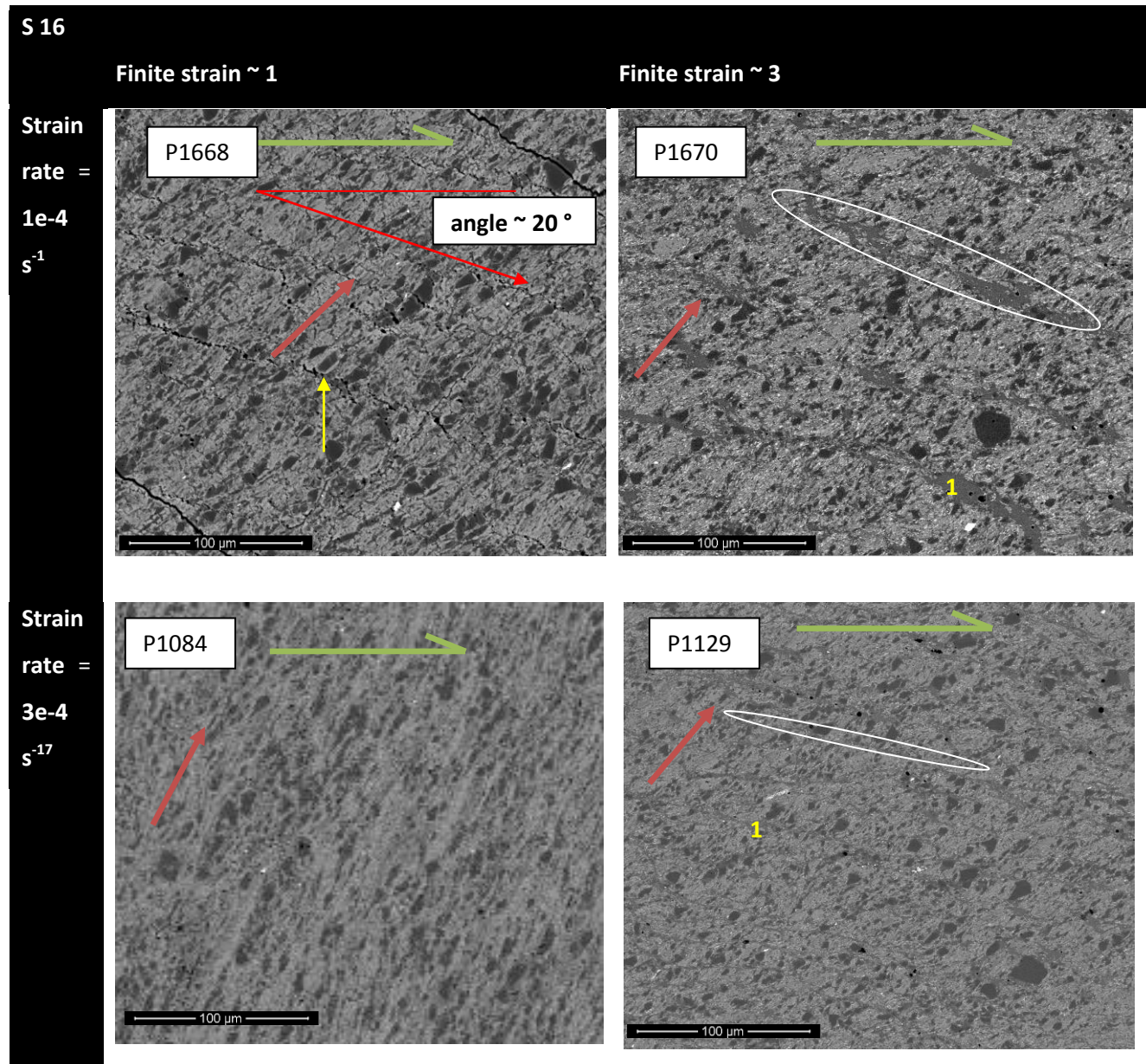


Figure 3.14 Overview of muscovite-rich samples (S16) all at the same magnification. Scale is 100 μm . Image in SEM BSE. Light gray indicates muscovite, medium gray melt, darker gray quartz and black are fractures or porosities. The intensity of the gray-scale is variable per image because the optimal settings of the SEM are variable. Areas of localised shear are marked with the white oval shape. The angle of the fractures or localisation bands is roughly 20° to the shear direction: confirming that the direction of the shear zones are low angle Riedel shears. In P668 the yellow arrow points to the low angle Riedel shear fracture. In P1670 number 1 indicates a melt pocket. In P1129 1 also indicates a melt pocket.

⁷ Samples P1084 and P1129 results discussed in dissertation E. Tumarkina, ETH Zürich (Tumarkina, 2012)

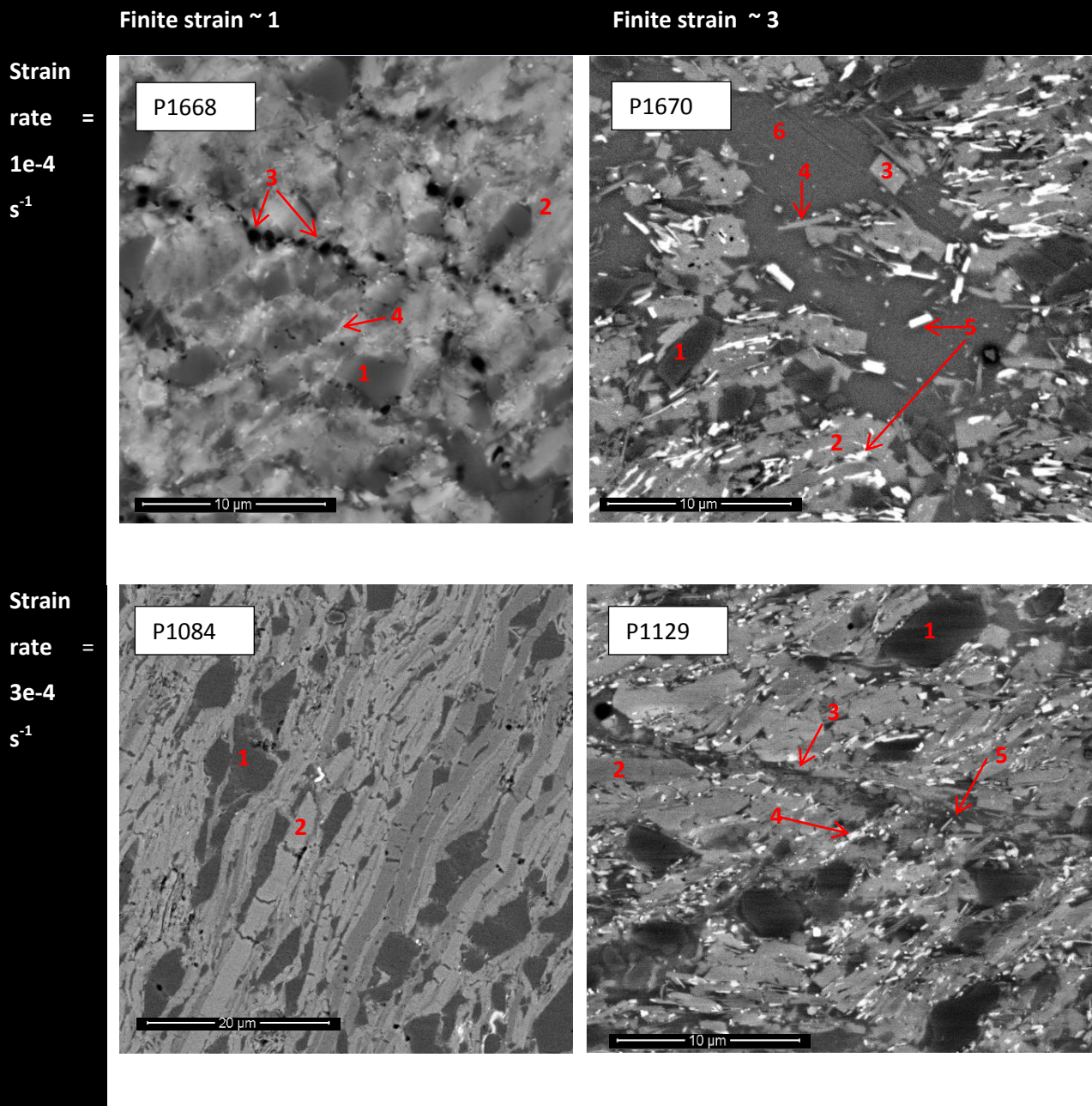


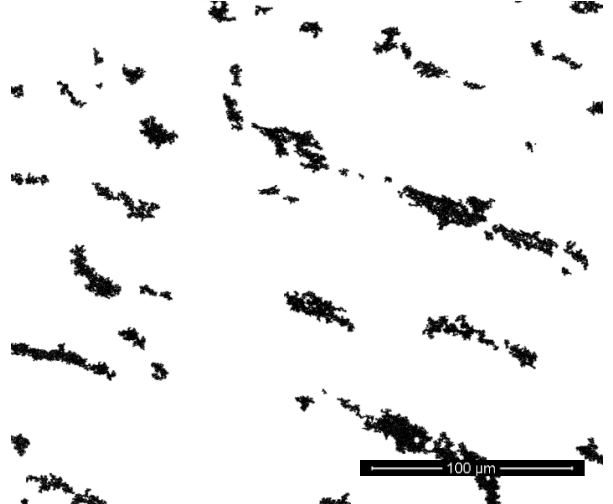
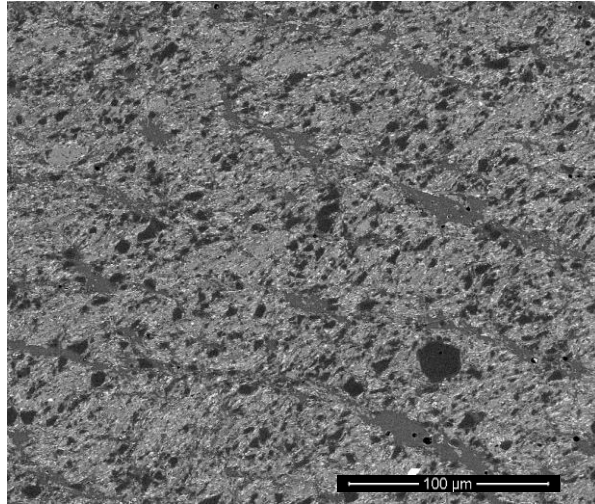
Figure 3.15 Overview of zoom-ins muscovite-rich samples (S16) in SEM BSE. Note: scale is not constant. Light gray indicates muscovite, darker gray quartz and black are fractures or porosities. The intensity of the gray-scale is variable per image because the optimal settings of the SEM are variable. P1668 numbers 1,2,3 and 4 respectively refer to quartz, muscovite, fracture and suspected sillimanite fibrous (characteristic shape). In P1670 numbers 1,2,3, 4, 5 and 6 respectively refer to quartz, muscovite, k-feldspar (characteristic shape), sillimanite (characteristic shape), biotite (shape and colour) and melt. In P1084 numbers 1 and 2 refer to quartz and muscovite. Note that quartz appears to be boudinaged. In P1129 numbers 1, 2, 3, 4 and 5 refer to quartz, muscovite, k-feldspar, biotite and melt.

S16 Shear bands SEM BSE Image

Melt pockets in shear bands

$\gamma \sim 3$

Strain
rate
=
 $1e-4$
 s^{-1}



Strain
rate
=
 $3e-4$
 s^{-1}

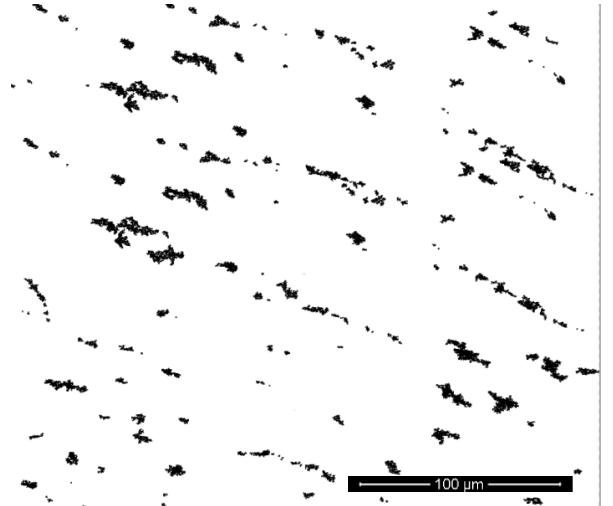
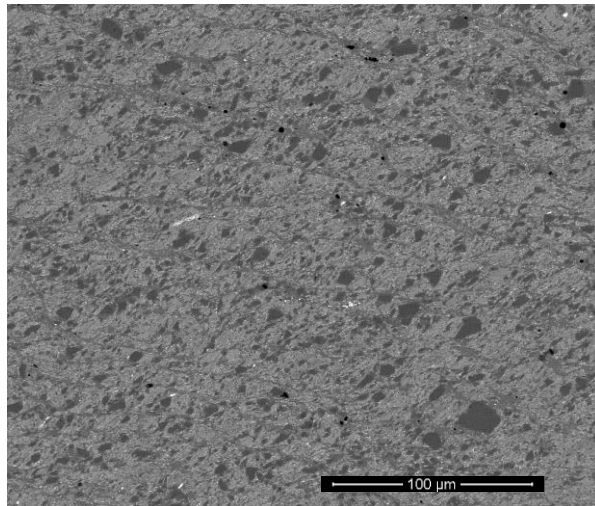


Figure 3.16 Muscovite-rich (S16) samples with high finite strain (γ) and variable strain rate ($\dot{\gamma}$). In the left column the original SEM BSE images, in the right column image with the melt-filled shear bands in black and all else in white. Shear is dextral.

3.3.3 X-ray Diffraction (XRD)

These muscovite-rich samples were prepared and measured in the same way as the quartz-rich samples. From the sample 16 series beside the sample itself P1668 and P1670 were measured. It was not possible to measure P1229 and P1084 because these samples had been completely consumed for other analyses. The complete overview of the results is given in Appendix A. The bimodal composition of the initial sample was confirmed. There was no significant new signal (i.e. non quartz or muscovite peak) in P1668. In P1670 however, biotite and orthoclase were detected (Figure 3.17). The coherence with the calculated peaks of sillimanite and the experimental XRD peak results of P1670 did not agree enough in order to be considered significant. The additional XRD figures can be found in Appendix A.

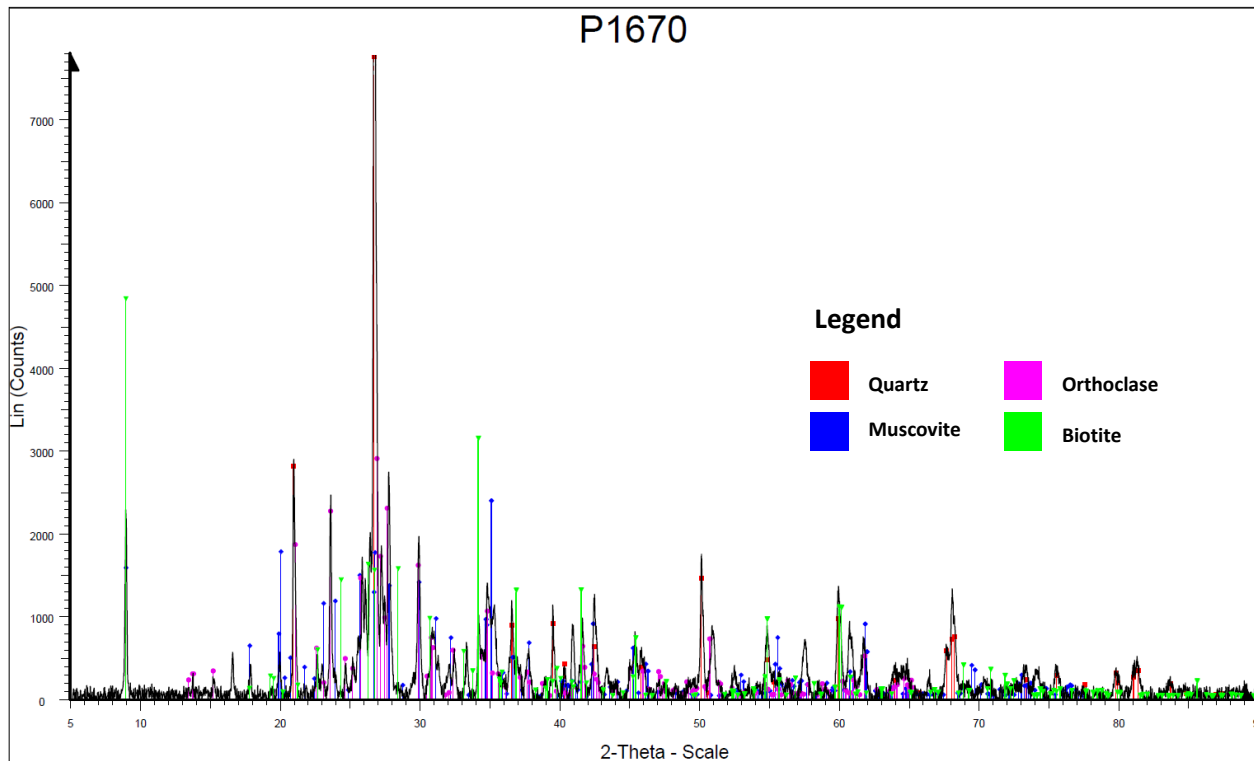


Figure 3.17 XRD plot with minerals P1670 identified using the ICDD database. P1670 shows new peaks of biotite and orthoclase.

3.3.4 Electron Probe Micro Analysis (EPMA)

Microprobe analyses were carried in order to constrain the melt composition in the melt bands. The 2 μm beam size of the probe results in a practical limitation for this work. The shear bands are generally only 2 μm thick or less, with the exception of P1670. Therefore point measurements were only done in the latter sample. A line measurement was taken of P1129 but this yielded unsatisfactory results. Details of this measurement can be found in Appendix D.

For the muscovite-rich experiment with low strain rate and high finite strain (P1670) the shear bands are between 2 and 10 μm thick. Therefore, it was possible to take several accurate point measurements and plot their composition. Because these measurements concern a melt and not a crystalline material the initial oxide data could not be corrected for a certain type of mineral. Hence the original electron microprobe data were plotted. In order to ascertain that the point melt measurements were not contaminated by muscovite it is also necessary to plot muscovite on the ternary diagram. Before doing that, the muscovite measurements also need to be validated. This is done by plotting the measured point on a cation replacement plot (Reed, 2005). Figure 3.18 shows that indeed the muscovite measurements fit on this plot. The composition of the melt is plotted in Figure 3.19.

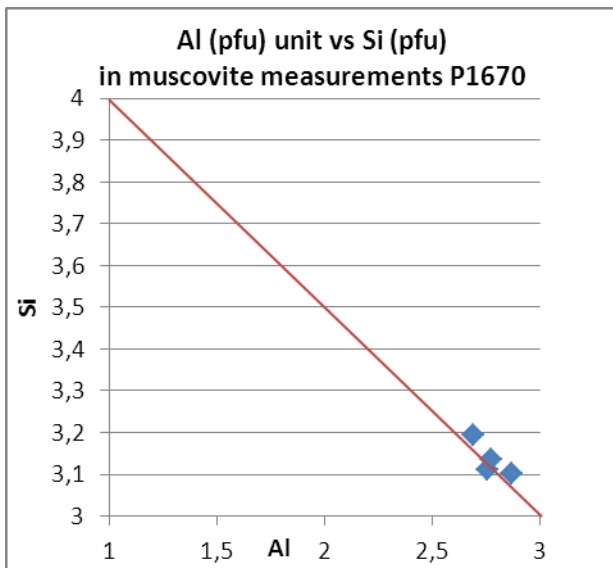


Figure 3.18 Cation abundance Al vs. Si in muscovite measurements P1670. The abbreviation “pfu” stands for “per formula unit”. Plotting on the line indicates the measurement fits with the mineral formula.

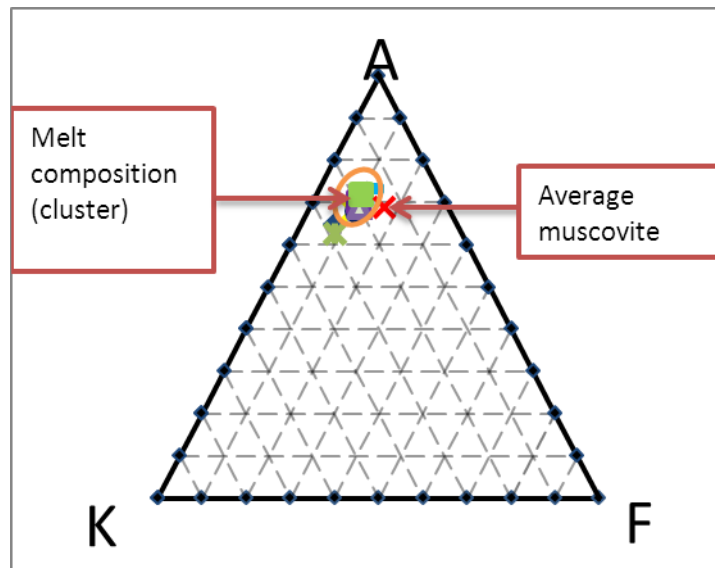
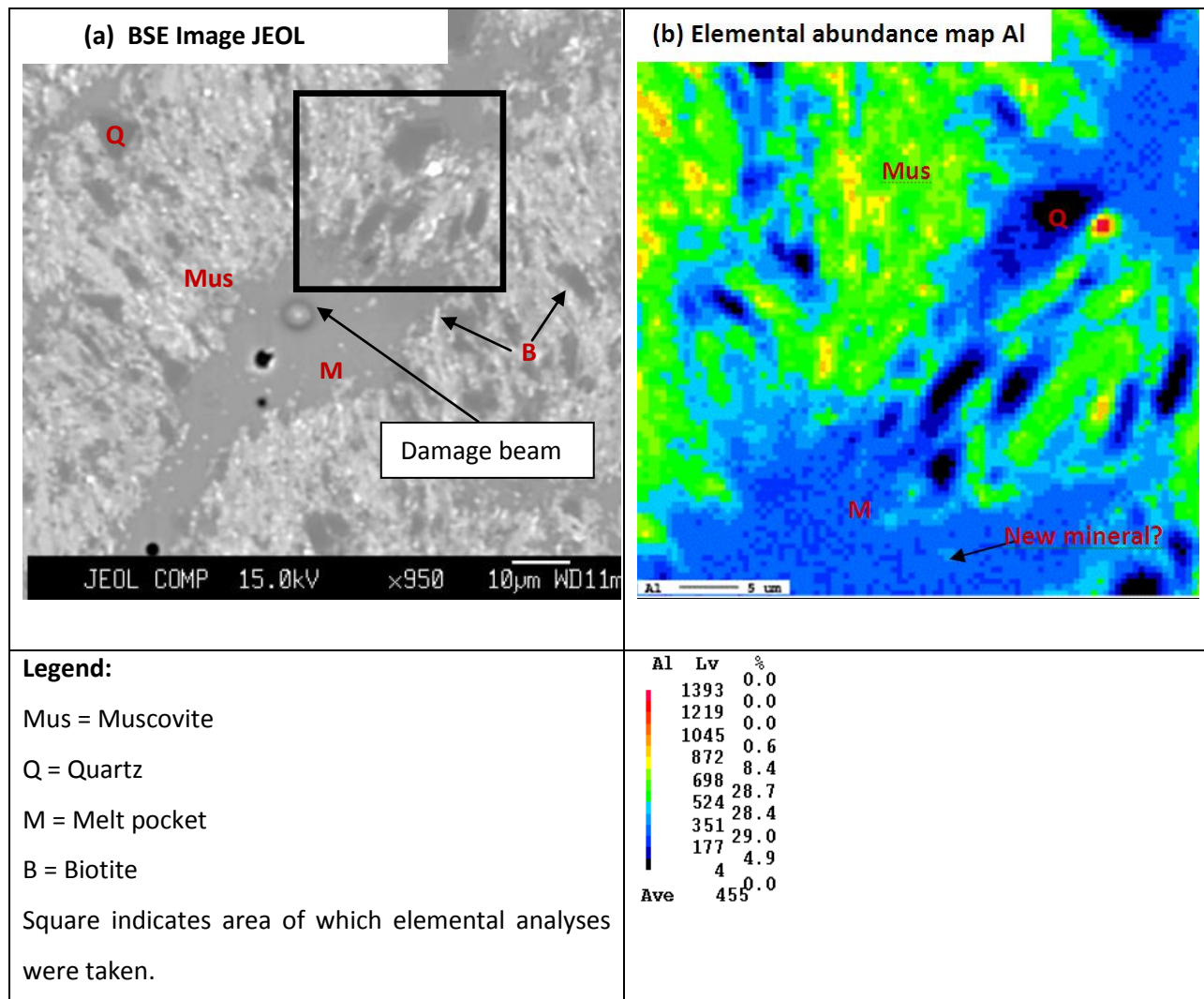
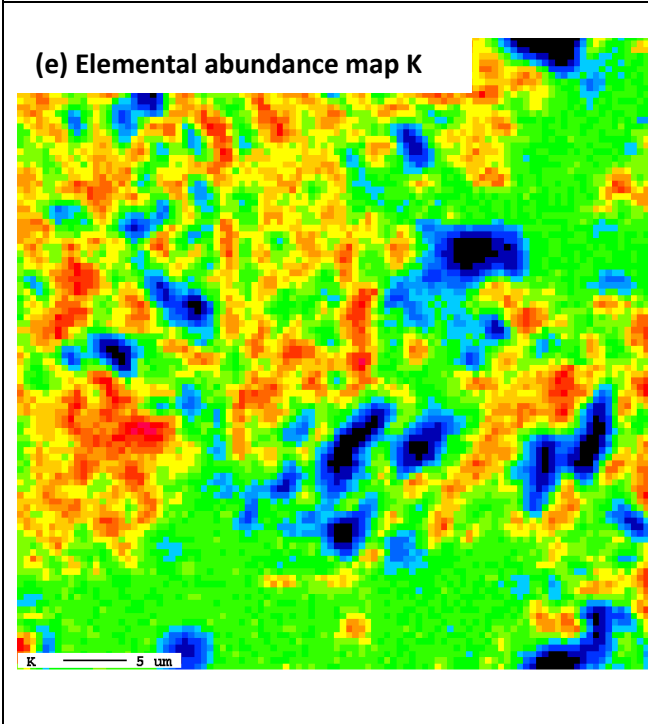
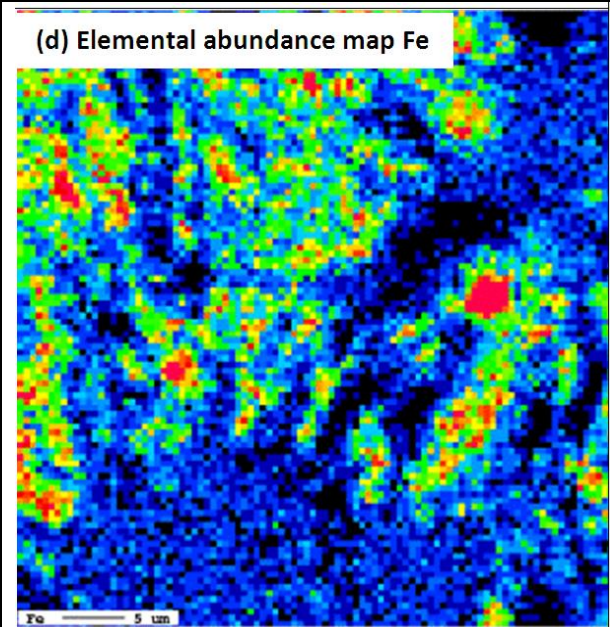
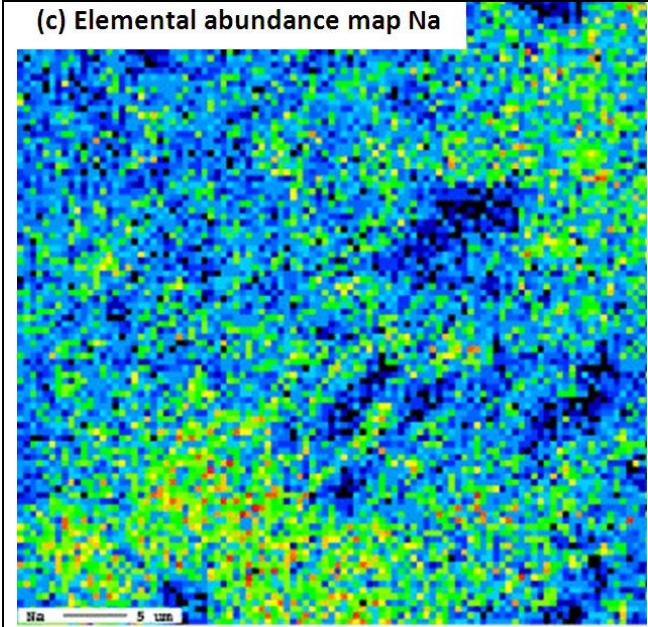


Figure 3.19 AKF diagram melt composition sample P1670. Here, A = Al_2O_3 , K = K_2O and F = FeO .

The elemental mapping of P1670 is done for the abundances of the elements Al, Na, Fe and K. In Figure 3.20 (a) the original backscattered electron (BSE) image is shown and the area on which elemental mapping has been performed is marked by the black square. The colour scale of the abundance plots is relative. The circular spot in the center of Figure 3.20 (a) is formed by the damage of the probe as a result of a measurement.

Summarizing, Figures 3.18-20 show that (1) the melt is a compositional mixture of both quartz and muscovite (2) melt composition of different melt pockets is highly similar (3) new minerals form in melt pocket (K enrichment) altering the composition within a melt pocket. Lastly (4) the system is very dynamic, melting and new mineral growth processes occur within nine hours.





Legends:

| Na | | | Fe | | | K | | |
|----------------------|-----|------|----------------------|-----|------|---------------------|-----|------|
| Na | Lv | % | Fe | Lv | % | K | Lv | % |
| [Color scale for Na] | 20 | 0.0 | [Color scale for Fe] | 32 | 0.8 | [Color scale for K] | 630 | 0.0 |
| | 17 | 0.1 | | 28 | 1.0 | | 551 | 0.5 |
| | 15 | 0.6 | | 24 | 2.2 | | 473 | 5.4 |
| | 12 | 1.9 | | 20 | 4.2 | | 395 | 17.7 |
| | 10 | 10.4 | | 16 | 8.5 | | 317 | 25.5 |
| | 7 | 16.4 | | 12 | 12.5 | | 238 | 33.9 |
| | 5 | 38.4 | | 8 | 18.9 | | 160 | 8.6 |
| | 2 | 22.2 | | 4 | 32.0 | | 82 | 4.7 |
| | 0 | 10.1 | | 0 | 20.0 | | 4 | 3.7 |
| | Ave | 6 | | 0.0 | Ave | | 9 | 0.0 |

Figure 3.20 Elemental mapping melt pocket sample P1670 by the EMPA.

3.3.5 Thermogravimetry Analysis (TGA)

In Figure 3.21 the dehydration of sample 16 (muscovite-rich) and the dehydration curve of the deformed sample P1668 are shown. All samples show significant dehydration, and the amount of loss is roughly the same for all samples, around 6 wt%. Striking is the high similarity in the shape of sample 16 (undeformed) and P1668 (deformed, no melt) which has two pronounced steps. There is a translational difference of roughly 1 wt% between the two. The path of the deformed sample with melt does not possess this two-step size.

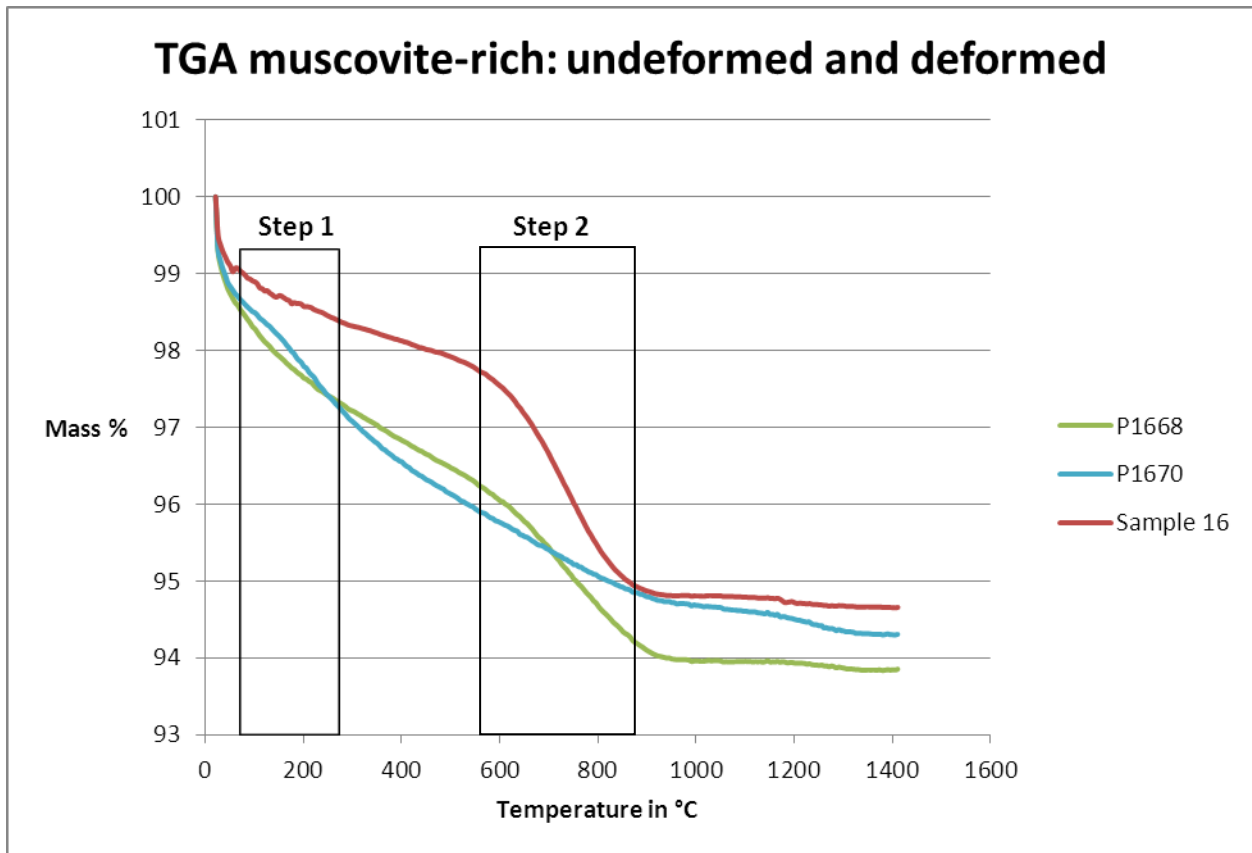


Figure 3.21 TGA muscovite-rich samples: undeformed and deformed. Sample 16 is the original sample (i.e. undeformed) and P1668 and P1670 have been deformed.

3.3.6 Focused Ion Beam (FIB)

The Focused Ion beam Scanning Electron microscopy (FIB-SEM) was performed on sample P1229. Because FIB-SEM is very time intensive and restricted regarding the size one sample (P1129) was imaged. This sample was deformed by E. Tumarkina and S. Misra at the ETH and was included in a publication by the latter authors in Tectonophysics (Tumarkina *et al.*, 2011). The reason that this sample was chosen rather than other candidates is that (1) shear band structure was well developed (2) shear band structure was small enough to be imaged and (3) new minerals had formed. The most optimal way of demonstrating the findings are in a movie which can be found in Appendix B as a digital document on the attached USB. Four key moments in the transect are illustrated in Figure 3.22 below. The video and images have been changed in ImageJ software (<http://rsbweb.nih.gov/ij/>).

From the FIB images in Figure 3.22 the following can be observed:

1. Regarding the data quality and scope:
 - Lack of contrast impediments the identification of the different phases. Quartz and melt cannot always be clearly distinguished from one another.
 - Charging and curtaining also decrease the visibility of the different phases
 - The visualized area is too small in order to visualize the anastomosing melt bands at depth.
 - The lack of contrast in new minerals especially in combination with the contrast variation along the sample makes it impossible to identify new species.
2. The melt band increases and decreases not only laterally (as seen in SEM) but also in depth (FIB-SEM).
3. Muscovite grains do not occur in the large melt pockets while quartz grains sporadically do.
4. Biotite occurs between larger grains but not in the larger pools of melt.
5. There is a lack of melt between larger grains that lie outside of the melt pocket.

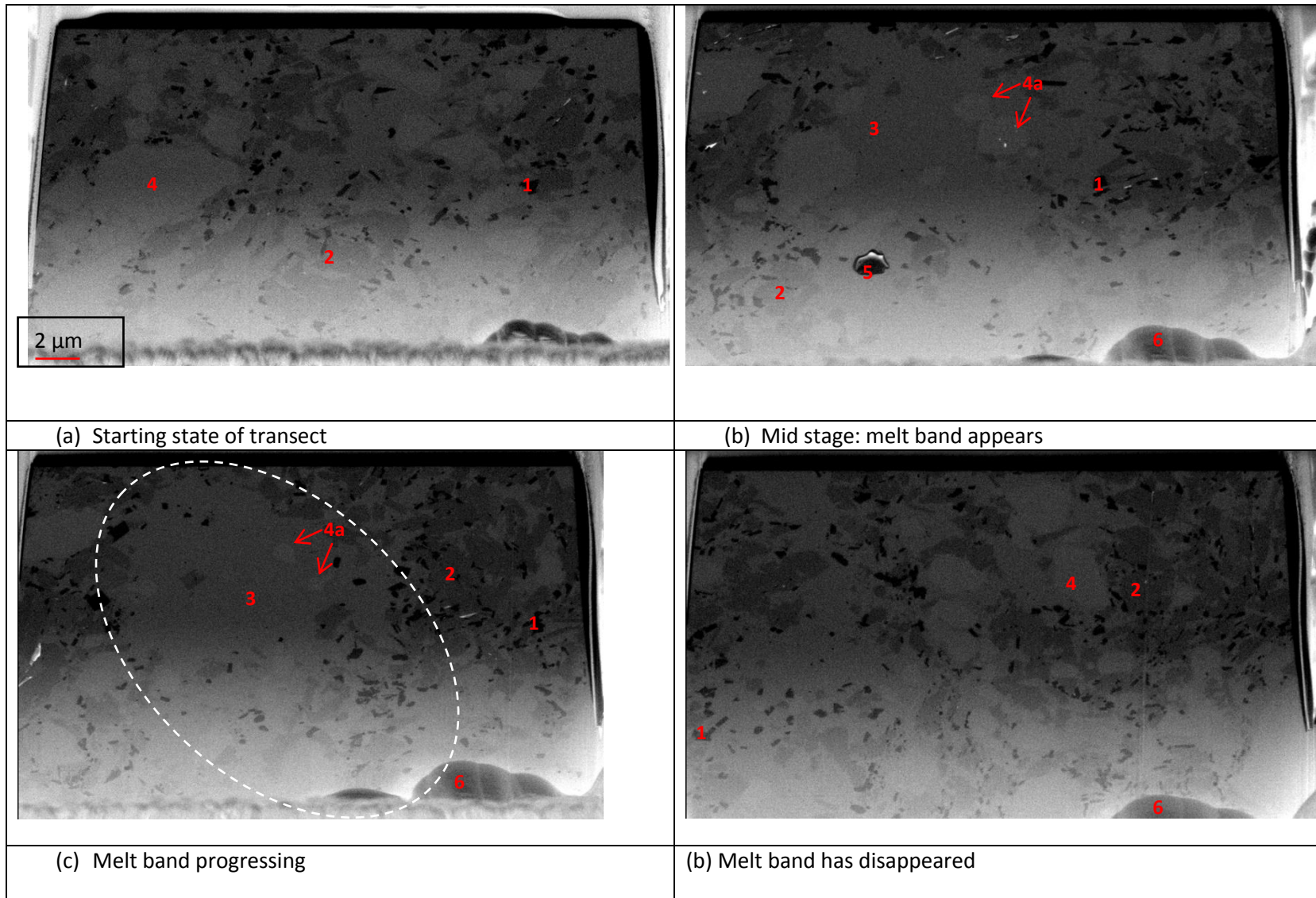


Figure 3.22 Key moments in the FIB transect through a melt band in sample P1129. Grayscale is inverted, scale is the same on all images. For the numbers (1) black is biotite (2) dark gray is muscovite (3) middle gray is melt and (4) lightest shade of gray is quartz. The identification of minerals based on grayscale is based on the known differences in weight of the different phases. Heaviest phases possess the darkest shade and vice versa. Note that the two phase 4 (quartz, lightest) grains that are visible in (b) are also visible in (c) but in the latter image they are already shrunken as the diameter of the grain decreased. They are marked with 4a. Porosities may persist in the sample and they are marked in the FIB images with 5. Milling products or “debris” is marked with 6. The melt pocket is marked by the dotted white oval. Charging of the sample and differences in angle caused the relative shade differences in individual images to vary and also caused differences within the image sequence.

Chapter 4. Discussion

In this chapter we will assess the effects of different composition, different strain rate and different finite strain on the mechanical properties and shear microstructures in synthetic metapelites.

4.1 General characteristics deformation experiments

Before assessing the separate effects of composition, strain rate and finite strain on deformation some general issues will be dealt with. The validity of the mechanical and chemical assumptions of the experiments will be evaluated in this section.

4.1.1 The power law creep exponent n and the deformation mechanisms

The power law creep exponent n value is indicative of the dominant flow law regime (Schmid *et al.*, 1977). The n values were determined by performing stepping strain rate experiments and using equation 2.8 which relates torque (M) to shear stress (τ). For abbreviations please see the chapter Materials and Methods. Equation 2.8 is based on equation 2.9 which assumes that deformation is accommodated by creep alone, i.e. not brittle deformation (Paterson and Olgaard, 2000).

$$\tau = \frac{4M(3+1/n)}{\pi d^3} \quad (\text{Eq. 2.8})$$

$$\dot{\gamma}_r = A\tau_r^n e^{\frac{-Q}{RT}} \quad (\text{Eq. 2.9})$$

In the case of P1669 there is coupled ductile-brittle behaviour, invalidating this assumption. In this instance a coupled law like the Mohr-Coulomb fracture criterion law would be more appropriate in order to describe the behaviour. The assumption for calculating the n value is not valid and hence the number is compromised.

$$\sigma_c = C + \mu\sigma_n \quad (\text{Eq. 4.1})$$

Here, σ_c is the critical shear stress, C is the cohesive strength (zero once there has been movement on the fracture), μ is the coefficient of friction and σ_n is the normal stress (Twiss and Moores, 2007). In Tables 4.1 and 4.2 is an overview of the different n values in the variation matrices. In the chapter Introduction the three deformation regimes and associated n values are explained after Schmid *et al.* (1977). If $n \sim 1.7$ superplasticity dominates, if $n \sim 4.7$ dislocation creep does. Experiments on which this is based were done on a limestone, and in these series we have performed experiments on bimineralic

metapelites. Assuming that the n power law exponent is also valid in this case, we can tentatively infer the following about the deformation mechanisms:

1. A. For quartz-rich, high finite strain (γ) and low strain rate ($\dot{\gamma}$) we see an n value that lies close to the value of Schmid's dislocation creep field. Dislocation creep would be controlled by the speed of diffusion (Schmid *et al.*, 1977).
B. Similarly, for muscovite-rich high γ and low $\dot{\gamma}$ we see an n value that is extremely close to the indication of Schmid *et al.* (1977) for dislocation creep.
2. A. For quartz-rich, high γ and high $\dot{\gamma}$ (P1672) we see an n value of 1.43: the regime of superplastic flow. Superplasticity depends on grain size: the strain rate increases when the grain size is decreased at the same stress. In P1672 we see a decrease in the grain size in the wide shear bands. Based on the theorem of Schmid *et al.* (1977) it can be concluded that this grain size reduction may lead to a concentration of strain. After initial grain size reduction the superplasticity could have initiated a positive feedback loop concentrating the deformation in the shear bands.
B. The muscovite-rich, low $\dot{\gamma}$ and low γ (P1668) also gives a low n value. However, because of the indications of brittle movement along the fractures this value should be disregarded.

The samples with higher n values should have stronger localisation as shown in Eq. 2.9. Indeed, there is a pronounced lack of clear localisation in P1672 and P1668. Localisation in P1671 and P1670 is clearly much stronger. This confirms the likelihood that P1672 deformed superplastically and that this was most likely accommodated by grain boundary sliding. P1671 and P1670 are more likely to have been deformed by dislocation creep.

Overall with the current data a clear pattern could not be distinguished. Therefore the n data can not give definitive answers regarding the deformation mechanisms. More deformation experiments combined with Stepping Strain Rate experiments should be performed.

Table 4.1 Values power law exponent quartz-rich sample. The notation "--" indicates that it was not possible to determine this value.

| Quartz:Muscovite 70:30 (sample 14) | Finite strain $\gamma \sim 1$ | Finite strain $\gamma \sim 3$ |
|--|---|-------------------------------|
| Strain rate $\dot{\gamma} 1e-4 s^{-1}$ | 9.14 (P1669) not valid: brittle ductile behaviour | 2.99 (P1671) |
| Strain rate $\dot{\gamma} 3e-4 s^{-1}$ | -- | 1.43 (P1672) |

Table 4.2 Values power law exponent muscovite-rich sample. The notation "--" indicates that it was not possible to determine this value.

| Quartz:Muscovite 30:70 (sample 16) | Finite strain $\gamma \sim 1$ | Finite strain $\gamma \sim 3$ |
|--|--|-------------------------------|
| Strain rate $\dot{\gamma} 1e-4 s^{-1}$ | 1.2 (P1668) Compromised: brittle movement along fractures? | 4.47 (P1670) |
| Strain rate $\dot{\gamma} 3e-4 s^{-1}$ | -- | -- |

4.1.2 Open or closed chemical system?

4.1.2.1 Water release from samples (TGA)

Firstly, water release is pivotal for the capacity of the rock to melt. Secondly, the difference in water loss between the undeformed and deformed samples can indicate whether the system is chemically closed or not. The TGA results have demonstrated that there is significant loss of water both in the undeformed and deformed samples. Consequentially it can be assumed that there is water available to initiate the melting.

However, data indicates that the undeformed quartz-rich sample loses more water mass percentage-wise than the undeformed muscovite-rich sample. This appears to be implausible because the only component that contains water is muscovite. This discrepancy could be due to two things:

- (1) A singular faulty measurement in the undeformed quartz-sample. This is corroborated by the result that the quartz-rich deformed samples possess less water than muscovite-rich deformed samples.
- (2) The overall results should not be interpreted quantitatively but rather qualitatively. More measurements would have been required to exclude either possibility.

It can be concluded with certainty that these measurements indicate that there is significant water loss in the original samples, and that there is still a significant amount of water present in the sample after the deformation. The water in the undeformed samples is presumed to be in the muscovite. In the deformed samples the water is presumed to be in the muscovite, biotite and melt. The two-step curves can indicate initial loss of atmospheric water up to ~100 °C and subsequent loss of water in the muscovite structure.

In the muscovite-rich series there is not much difference in water release between the deformed and undeformed samples: this could indicate a closed system. The quartz-rich samples have the opposite result: an open system. In previous work by Tumarkina (2012) loss of water was also established and there the conclusion was that the “rough” calculations indicate the Paterson Rig does not provide a closed system. Therefore the overall possibility of water loss from the sample is not excluded, and this system may not be chemically closed.

4.1.2 Biotite composition and the (in)flux of Fe²⁺ and Mg²⁺

In a large part of the experiments biotite has formed. The chemical composition of biotite is different from muscovite in the sense that it is richer in Iron (Fe) and Magnesium (Mg) than muscovite. There are two possible sources for the Fe²⁺ and Mg²⁺. Either (1) it comes from the muscovite. The amount of iron and magnesium released from muscovite should be sufficient to build the amount of biotite that is visible; consequentially the melt should be extremely depleted of Fe²⁺ and Mg²⁺. Or (2) the source of these metallic ions is the iron alloy jacket. The jacket is in direct (unshielded) contact with the outer layer of the sample. The outer layer is the examined layer because the strain is the highest there. The jacket is deformed and twisted at high pressure and temperature as well. Therefore it is possible that Fe²⁺ and Mg²⁺ started to diffuse into the sample. From the PerpleX calculations of Tumarkina (2012) it is known that biotite is thermodynamically more stable than the starting minerals. Therefore there will be a thermodynamic drive to decrease Gibbs free energy by forming it. This in turn could be a driving force for the transport of Fe²⁺ and Mg²⁺.

Back-of-the-envelope calculation of the Fe²⁺ and Mg²⁺ source

In order to establish whether option (1) is possible we will execute a simple calculation. The goal is to see how many moles of Fe²⁺ and Mg²⁺ are released from muscovite and if this amount is sufficient to build all the biotite that is present.

An estimate of the surface of the different phases in a representative image of P1670 (muscovite-rich, high γ , low β) is respectively for muscovite, quartz, melt and biotite 50, 20, 20, 10 area %.

Chemical formula of biotite is from the Mineralogy Database (mindat.org), because we could not establish the chemical composition of biotite in our samples. The chemical composition of muscovite was established with the Electron Microprobe by S. Misra (Misra et al., 2009).

Rough calculation in moles. Assuming (1) that volume per unit formula of mineral is the same, (2) no Fe or Mg goes into the melt, (3) that 70 volume % roughly equals 70 area % and (4) composition remaining muscovite is constant.

- Loss area muscovite: - 20 area %, increase area biotite + 10 %.
 - Moles Fe²⁺ released from muscovite: 0.2*0.3 = 0.06, Moles Mg²⁺ released from muscovite: 0.2*0.1 = 0.02
 - Moles Fe²⁺ required for biotite: 0.1*1.5 = 1.5, Moles Mg²⁺ required for biotite: 0.1*1.5 = 1.5
- Amount iron and magnesium from the disappeared muscovite cannot accommodate the required Fe²⁺ and Mg²⁺ for biotite. There is roughly a factor of 25 or 75 more iron required for biotite than is roughly liberated. This discrepancy is so large that it is significant even though the calculation is simplified. Hence the ions most likely originate from the iron alloy jacket.

| | |
|--------------------------------------|---|
| Biotite general chemical composition | $K(Mg,Fe^{2+})_3[AlSi_3O_{10}(OH,F)_2]$ |
| Muscovite composition this series | $(K_{0.9}Na_{0.1})(Al_{1.6}Fe_{0.3}Mg_{0.1})[Si_{3.2}Al_{0.8}O_{10}](OH)_2$ |

4.2 Static vs. Dynamic systems: impact on melt transport

It is necessary to assess the differences between the distribution of melt in static versus deforming (stressed) systems because they impact the transport of melt.

4.2.1 Phase diagrams and mineral stability

In the preceding work by Tumarkina (2012) phase diagrams were modeled using Perplex (<http://www.perplex.ethz.ch/>) for the based on the chemical composition of the initial samples used in this thesis. The modeling provided in the following results:

1. Quartz-rich rocks at experimental condition would, at equilibrium condition, consist of:
Biotite, melt, K-feldspar, spinel, sillimanite and quartz.
2. Muscovite-rich rocks at experimental condition would, at equilibrium condition, consist of:
Biotite, melt, K-feldspar, spinel and sillimanite.

As a consequence we must conclude that without deformation and at elevated P, T the initial mineral assemblage (quartz, muscovite) is not stable and will start moving toward equilibrium. This will lead to the transformation of the initial minerals to the previously mentioned phases such as melt and biotite. This effect needs to be taken into account when we want to distill the exact effects of deformation.

4.2.2 Static experiments

In order to compare our dynamic experiment to their static twins we will here summarize and evaluate the results of several static experiments by Tumarkina (2012) in the Paterson Rig. The absence of the state of equilibrium by changing the P, T conditions already brings about large changes in mineralogy and morphology in the samples. The relevant experiments and their characteristics can be summarized in Table 4.3 below.

Table 4.3 Overview static experiments Tumarkina (2012) all experiments performed at 300 MPa.

| Sample type | Time experiment | mineralogy | Deformation apparatus |
|----------------|-----------------|--|-----------------------|
| Muscovite-rich | 1 hour | Fe-rich phengite and Fe-poor phengite | Paterson Rig |
| | 2 hours | Small melt pockets along grain boundaries (7 % area, ~1 µm) Fe-rich phengite and Fe-poor phengite (no | Paterson Rig |

| | |
|---------|--|
| | original muscovite) |
| | Melt associated with sillimanite +biotite |
| 5 hours | Melt along grain boundaries and as Paterson Rig continuous films along grain boundaries (13 area %) Other new phases (sillimanite and biotite) present in higher abundance. K-feldspar grains occurred. |

Representative images collected by Tumarkina (2012) in SEM BSE can be found in Figure 4.1 below. Taking into the effect of the static situation, the question is: what can we say about the effects of shearing specifically on localisation, weakening and the transport of melt?

The following can be concluded from them:

1. Experiments show that at 300 MPa and 750 °C the sample decomposes to form melt, biotite, sillimanite and k-feldspar. This is confirmed by PerpleX calculations.
2. The 1-hour experiment has the same duration and composition as P1084 with $\dot{\gamma} = 1$ (low) and $\dot{\gamma} = 3 \cdot 10^{-4} \text{ s}^{-1}$ (high).
 - ➔ P1084 contains quartz and muscovite as does the static experiment (Tumarkina, 2012). So, at this stage the differences are not clearly visible.
3. For the 3-hour muscovite-rich experiments (P1129, P1668) one can average interpolate the static experiments of 2 and 5 hours. Quartz-rich 3-hour experiments P1669 and P1672 cannot be compared effectively because muscovite controls water release and the formation of melt. The muscovite content is different from the experiments by Tumarkina (2012).

Interpolation entails that we expect the 3-hour static stage to be somewhere between the existence of melt pockets and the emergence of melt films along the grain boundary (~ 9 area % melt, assuming a constant increase in melt).

 - ➔ In P1129 there is roughly 20 area% melt, approximately double of the static experiment (Tumarkina, 2012). Still, it has to be concluded that not all melt can be attributed to deformation

→ P1668 there is no melt visible. This result is puzzling because even in static experiment there is melt. There were no experimental malfunctions visible during the experiment.

4. Analogously, for the nine-hour experiment of P1670 we can extrapolate the results of the five-hour static experiments. In the static state we expect 21 area % melt, assuming the interpolated melting rate of 2 area % per hour. Also, a visible presence of other phases such as biotite, sillimanite and K-feldspar. Descriptions of mineralogy after Tumarkina (2012). In P1670 we see an estimated 30 area % melt, and the melt is strongly focused in the melt bands. This value is based on SEM imaging and pixel counting of melt identified with the same greyscale. The growth of new minerals, especially k-feldspar is concentrated along the rims of the melt pockets.

Summarizing, the location and quantity of melt is dependent on deformation. There is a significant effect of deformation 1) in the location of the melt and 2) in the quantity.

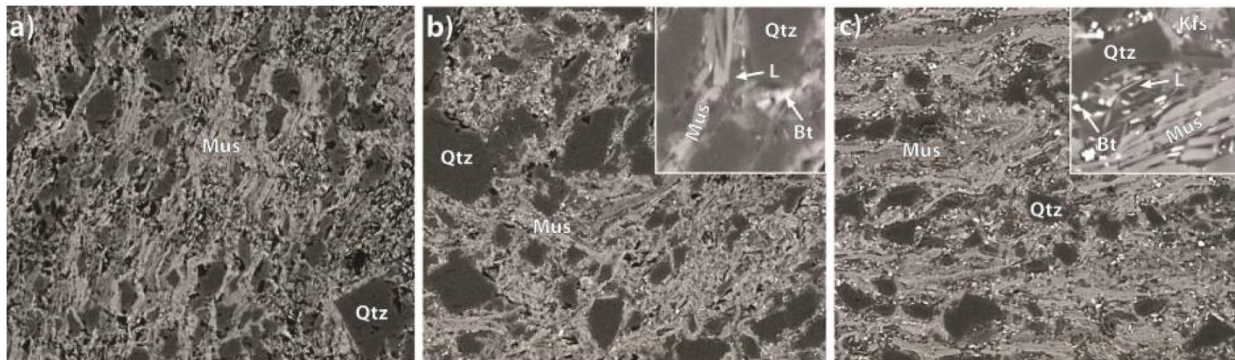


Figure 4.1 Paterson Rig experiments after Tumarkina (2012) all at 300 MPa and 750 °C. Respectively a), b) and c) are 1, 2 and 5 hours duration experiments. Images are at high magnification. Mus = muscovite, Qtz = quartz, Bt = biotite, Kfs =K-feldspar and L = liquid (melt).

4.2.3 Implications differences for melt migration

4.2.3.1 Melt distribution in current experiments

It has been established by Tumarkina (2012) that in the static experiments of more than 2 hours the melt occurs ubiquitously at the grain boundaries throughout the sample. In the dynamic experiments it was visible that the melt was highly concentrated in the shear bands. Between the grains there were newly formed crystals visible but no separate melt pockets (P1670 and P1129, confirmed by SEM, FIB-SEM and XRD). The FIB-SEM analysis on P1129 has proven that also in depth the areas between the grains were mostly devoid of melt, with only residual biotite. The melt was mostly present in the shear bands. The thickness in depth of these shear bands was found to be highly variable on the scales of tens of μm and the melt zones extended to at least 20 μm into the sample. The variability in thickness may have profound effects of transport: the melt may be initially concentrated but if it then gets “stuck”, no effective transport can take place. Microprobe analyses in sample P1670 have proven that the melt in P1670 is of uniform composition (eutectic melting). It was not possible to measure the melt in other samples.

There are indications of at least planes of weakness (P1668) or shear zones with grain size reduction fracturing (P1669) which may cause a pressure gradient, causing the melt to migrate.

4.2.3.2 Mechanisms of melt transport

Kohlstedt and Holtzman (2009) diverge on the importance of shearing and the transport of melt in the crust. *Melt migration* indicates transport of melt on distances larger than the grain size, *melt segregation* indicates that there are regions depleted of melt and enriched in melt. Kohlstedt and Holtzman (2009) distinguish between the shear stress driven regime with a viscous response and in one occasion in the brittle field. Focusing on these two mechanisms:

(1) stress-driven melt segregation in the viscous regime.

When subjected to shear, melt spontaneously segregates into melt-enriched channels (Stevenson, 1989). This is also what has been observed in our samples P1670 and P1129. The mechanism behind this, as proposed by this author, is that the complete viscosity is very sensitive to the melt fraction. This entails the following. When a small perturbation in stress occurs and more melt forms, this part becomes weaker. This drives the melt from the higher pressure areas to the lower pressure areas. Areas with more melt are weaker and hence have lower pressures. A positive feedback loop forms and melt accumulates. This has been observed for mantle mineralogy rocks (Kohlstedt and Holtzman, 2009 and

references therein) and has now also been established to occur in hydrous metasedimentary rocks in our research.

(2) stress-driven melt segregation in the brittle regime

When brittle fractures exist melt can be transported along these pathways, parallel to the shear plane (Holtzman *et al.*, 2005). In P1669 there is evidence of brittle behavior in Riedel shears. In P1672 there was grain size reduction (brittle) and melt visible, also in Riedel shears. The Riedel shear direction is not parallel to the shear plane. Therefore it is unclear whether this process dominated melt transport in P1672 or P1669.

4.2.3.3 Concluding remarks regarding melt transport

Overall, it can be concluded that the shearing of metapelitic rocks has a significant positive impact in the formation of melt and its concentration in low angle Riedel shear direction. This enhanced concentration can impact transport of melt. It also impacts the overall crustal rheology because the rocks with more melt will be the weakest (the more muscovite the weaker). Consequently, muscovite-rich rocks will concentrate the deformation and melt formation. Partial melting of the weakest (muscovite-richest) crustal rocks may determine a large part of the production of partial melt in the crust. Misra *et al.* (2011) describes that sheared metapelitic rocks with a high percentage of partial melt in shear zones may play an important role in the decoupling of material in the lithosphere.

At the moment we detected eutectic melting (EMPA results) but it can be possible that the melt composition changes resulting from (1) formation of new minerals (2) non-eutectic melting when one of the starting materials has run out. Our results regarding enhanced deformation-induced melt migration and formation is consistent with other authors (Rushmer, 2001; Misra *et al.*, 2009; Connolly *et al.*, 1997). A major disadvantage of the lab is that the melt cannot escape the system, while it can in natural systems. Attempts to solve this issue were undertaken placing using porous spacers on the sample by S. Misra (p.c., 2012). However this set-up proved to be too weak: the experiments could not be executed.

4.3 Effect of chemical composition

The goal of these experiments was to emulate natural circumstances. As metapelites vary compositionally in nature two different compositions were taken. Samples were composed of a quartz: muscovite volume ratio of 70:30 and vice versa. Differences resulting from changes in composition can be observed both in the rheology, microstructures and chemical composition.

Rheologically, for more quartz-rich samples:

1. Higher shear stresses are achieved when subjected to deformation
2. Shear stress decrease (i.e. weakening) occurs less quickly, as is expressed by the lower power law exponent n value at $\dot{\gamma} \sim 3$ and $\dot{\gamma} = 1e-4 \text{ s}^{-1}$ (hence it exhibits less pronounced localisation).
3. Both the quartz-rich and quartz-poor samples fall within the dislocation creep deformation field with the n power law value.

Microstructurally, a more complex image emerges. In Table 4.4 below an overview is given. Overall, we can conclude that more muscovite leads to stronger localisation across thinner areas and induces melt more strongly. In the case of more quartz a rock is more prone to grain size reduction as a mechanism to accommodate shear. An interpretation of the causes of these differences is given in Table 4.5.

Table 4.4 Overview microstructural differences per composition.

| Both compositions | Finite strain ~ 1 | Finite strain ~ 3 |
|-------------------------------------|---|--|
| Strain rate = $1e-4 \text{ s}^{-1}$ | <p>1. Quartz-rich: Ductile brittle transitional behaviour, visible movement along shear zones. Grain size reduction and angular quartz fragments dominate shear zone.</p> <p>2. Muscovite-rich: Low angle Riedel shear fractures, either originated syn or post deformation (undetermined). Value n 1.2.</p> <p>➔ Comparison compromised</p> | No comparison possible |
| Strain rate = $3e-4 \text{ s}^{-1}$ | No comparison possible | <p>1. Quartz-rich: Wide shear bands with traces of grain size reduction and with melt.</p> <p>2. Muscovite-rich: Melt-filled shear bands up to 5X thinner, $\sim 2\mu\text{m}$ thick, elongate, connected and anastomosing. Their direction is roughly in the low angle Riedel shear direction as well. There is no evidence (any more) of brittle behaviour. Value n 2.5.</p> |

Table 4.5 Overview mechanisms behind differences resulting from different composition.

| Feature | Perceived mechanism |
|--|---|
| Magnitude of achieved shear stresses | <p>In quartz-rich samples the quartz is determines the overall strength of the rock. The strength of quartz exceeds that of muscovite under the same circumstances, so higher shear stresses are achieved in the quartz-rich materials. This is in accordance with the microstructures, where quartz behaves brittlely whilst muscovite is already deforming ductilely.</p> <p>More muscovite-rich rocks will be weaker in a series of metapelitic rocks. As a consequence, shear will be more concentrated in then and they could function as an “easy” rock: dictating the speed at which the crust is deforming</p> |
| Rate of weakening | <p>More rapid in muscovite-rich samples because the more muscovite rich samples release water and produce relatively more melt than the quartz-rich sample does. The quartz-rich samples experience grain size reduction (P1669, P1672) which appears to progress over time. As grain size reduction continues grains become smaller, flow becomes easier and the rock becomes weaker. This can cause the slow weakening observed in P1672. If there is melt present (muscovite-rich) samples (P1129, P1670) deformation is accommodated by the latter. The melt weakens more strongly and constantly than the quartz-rich dominating grain size reduction.</p> |
| Power law exponent n value | <p>Both known exponents lie (high finite strain and low strain rate) in the dislocation creep field (Schmid <i>et al.</i>, 1977).</p> |

Role of composition in P1668 vs. P1669

In the Results chapter it became clear that there are some questions regarding the experiment P1668 and the relation to experiment P1669. Based on two interpretations there are two conclusions possible.

1. Fractures in P1668 occurred during the experiment (syn). Movement along the fractures allows for weakening because strain localises along these plains. Evidence is sporadic and inconclusive. The fractures are in the low angle Riedel shear direction. For the progressed version of this

experiment (P1670) the low angle dilatant Riedel shear fracture could provide space for the melt. In the pore the pressure is lower and therefore there would be a pressure gradient driving the movement of melt in this direction (Kohlstedt and Holtzman, 2009).

Contradicting this possibility is that the opening of fractures requires significant force under 300 MPa.

2. Fractures in P1668 occur after the experiment (post). Because the confining pressure is released rapidly the sample will fracture in the planes that are the most weakened. These planes of weakness coincide with the direction of melt filled shear bands in the progressed experiments. If these planes would have already been weakened at a finite strain of 1, then there is still a possibility that as the experiment progressed toward higher strain the melt would have concentrated there because of the previously mentioned melt localisation behaviour (Kohlstedt and Holtzman, 2009).

The comparison with P1669 (more quartz) is complicated by this conundrum. P1669 has ductile-brittle behaviour whilst it has less muscovite than P1668. This is strange because the more muscovite one has the more one would expect ductile (weaker) behaviour. Both experiments should be repeated in order to provide answers; with the current data no definitive statements can be made.

4.4 Effect of strain rate ($\dot{\gamma}$)

The relative differences resulting of the relative change in strain rate can provide us with information about the rheology of metapelites in nature, in spite of the fact that the lab strain rates are multiple orders of magnitude too large. This comparison is only valid for the muscovite-rich sample because the quartz-rich series does not contain sufficient data.

Rheologically,

1. Samples with the higher strain rate go up to higher shear stresses
2. Weakening of the sample occurs at a later (i.e. more progressed) stage of deformation
3. The power-law rheology implies that the faster deformation occurs the higher the stress must be to achieve the same deformation. There is not sufficient data from the n power law exponent to be able to compare the effect of strain properly.

Microstructurally, the following features can be set out against each other in Table 4.6:

Table 4.6 Variation matrix muscovite-rich experiments. Abbreviation “w.r.t.” short for “with respect to”.

| Quartz:Muscovite 30:70 (sample 16) | Finite strain $\gamma \sim 1$ | Finite strain $\gamma \sim 3$ |
|--|---|--|
| Strain rate $\dot{\gamma} 1e-4 s^{-1}$ | Brittle fractures, syn or post (P1668) → Experiment is compromised | wide melt bands (P1670) few new crystals w.r.t. melt |
| Strain rate $\dot{\gamma} 3e-4 s^{-1}$ | No clear localisation features (P1084) | narrow connected melt bands (P1129) more new crystals w.r.t. melt |

Summarizing & concluding: Higher strain rates go up to higher shear stresses and localise more slowly because of the power law relation between stress and strain rate “shear thickening”. The microstructures manifest this as well: the shear bands are thinner for higher strain rates. In geological settings this behaviour may impact the distribution of strain. If quickly deforming rocks become harder to deform by “shear thickening” the strain may shift to rocks with a lower strain rate. This redistribution of strain may impact the applicability of usage of such high strain rates in experiments. This effect of strain rate may also impact melt migration. Strain rate impacts the morphology and thus connectivity of melt band and hence the possibility of melt to escape the system.

4.4 Effect of finite strain (γ)

In the muscovite-rich series of experiments it was possible to establish that the deformation mechanisms evolve and change strongly with progressive straining. The strength of the rock increases up to the yield point ($\gamma \sim 0.3$, dependent on strain rate) after which it decreases up to a stable value. The crux underlying this phenomenon is the “ease” of deformation along the planes of weakness or shear zones. Around lower strains ($\gamma \sim 1$), weakening has not occurred to a very large extent. In the microstructures underdeveloped shear zones (P1668, P1084). As the finite strain progresses the shear zones connect and many “easy” glide planes occur, allowing for lower strength of the rock (P1670, P1129). Fuisseis *et al.* (2006) also describes these features in the field of Cap de Creus, Spain. The underdeveloped shear zones in our experiments lie around phase (3) in Figure 4.2 below. The developed shear zones are more analogous to phases (4) and (5). This has major consequences on overall metapelitic crustal rheology: as straining continues the crust may become weaker. Our experimental studies provide experimental evidence for the inferred crustal weakening of Fuisseis *et al.* (2006). We will digress on this in the next section on the geological context. It can be concluded that the

experiments are well reproducible, because the shear stress vs. strain paths of several experiments are similar.

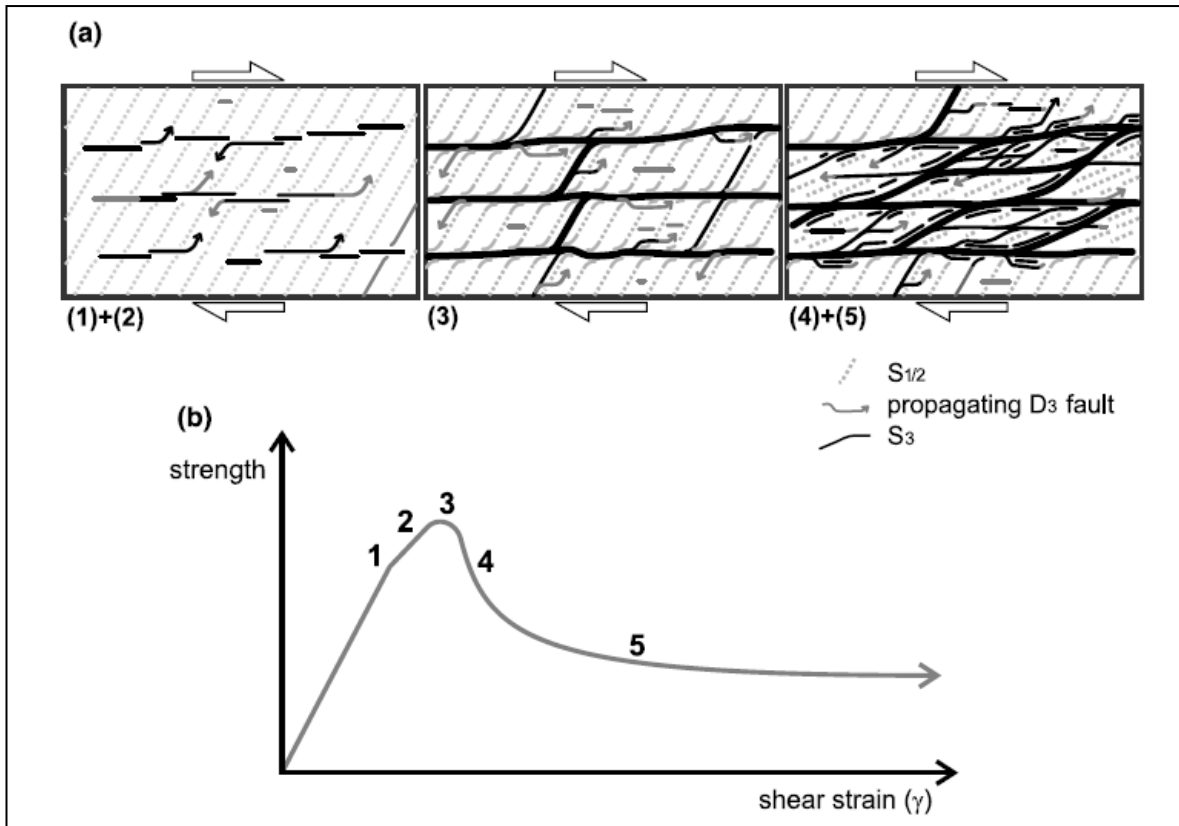


Figure 4.2 Model for the mechanical evolution of a shear zone networks under progressive strain. Note: scale on hundreds or thousands of meters. Part (a) mechanical evolution shear zones (b) according rheology (Fusseis et al., 2006).

4.5 Application in Geological context

In order to be able to simulate naturally deforming systems in the lab the strain rates are increased orders of magnitude and the temperature is increased above the geotherm. This allows us to reproduce features we see in nature in the lab. However, it impediments the translation of rheological and microstructural data from the lab to natural systems. Temperature has a profound effect on the deformation mechanisms as explained previously in this chapter. Below we will assess three geological settings in which our results could be used: (1) Bushveld Intrusion, South Africa (2) Cap de Creus, Spain and (3) seismic profiles of the deeper crust.

(1) Bushveld Intrusion, South Africa

An intrusion into the crust can cause relatively high temperatures to occur at lower pressures. There is some deformation in most cases, but not as extreme as in the case of collision zones. In the Bushveld area, South Africa an intrusion was emplaced into metasediments around 2,06 Ga. Subsequent partial melting of the rocks of metapelitic composition ensued. At the peak of metamorphism anatexis (partial melting) occurred at 300 ± 50 MPa pressure and a temperature of 750 °C (Johnson *et al.*, 2003). Johnson *et al.* (2003) found that eutectic and paratactic partial melting formed migmatites. Melting was induced by pulses of fluid coming from the cooling underlying intrusion. The amounts of formed melt are estimated to be > 10 mol % and flow of melt is thought to be deformation-driven. This is consistent with the amounts of melt in our metapelites and our interpretations regarding the effects of deformation. Though the P, T conditions are highly similar to our experiments there are major geological differences. There is no major uniform shear stress component and the system is continuously changing because of an input of fluid and a loss of melt. Nonetheless, the example confirms the validity and importance of our results. Perhaps the Bushveld microstructures can be used to infer relative differences in strain rate by using the newly acquired knowledge in this thesis regarding the effect of strain rate.

(2) Cap de Creus, Spain

The area of Cap de Creus, Spain is characterized by high strain Hercynian deformation. The area consists out of metapelites and metagraywackes. The lithology and deformation regime bear strong similarities to our experiment. However, our high strain rates and high temperature remain unfeasible for this area. This area comprises shear zone networks that resulted from the deformation. Shear zones that exceed several meters in size are often interconnected to neighboring shear zones. There are also areas which show the brittle-viscous transition (Druguet *et al.*, 1997). Similar structures on a much finer scale occur

in P1129 and P1669 respectively. Assuming scaling is possible then FIB-SEM on experimental sample (small scale) would provide a wealth of information. Conclusions from the lab could be extrapolated to the natural shear zones. Also, because of the similarities of the microstructures the rheological information from our experiments may be applied to the field. In this case it would enable one to see which areas were deformed more rapidly than others due to the strain rate dependence behaviour. Our conclusions regarding the effect of finite strain also provide experimental evidence that crustal weakening occurred as the deformation progressed. This is due to the development of interconnected shear zones as discussed in the previous paragraph.

(3) Deep crustal rheology of quartz muscovite rocks

Deformation is known to impact the overall large-scale crustal rheology, especially in collision zones. Analyses on the seismic signals of quartz and muscovite-rich rocks have been explored by several authors (Mahan, 2006; Naus-Thijssen *et al.*, 2011; Ward *et al.*, 2012). The seismic signal from molten rocks or rocks with a strong preferred orientation is different from that of solid material without a preferred orientation (Mahan, 2006). The paper by Naus-Thijssen *et al.* (2011) focuses on how different microstructures affect wave speed. It was found that an increase in muscovite content and an increase in the alignment of these grains results in greater seismic anisotropy. What we have concluded from our experiments is that the muscovite slivers are rotated by shearing as a result of deformation. It cannot be established if their alignment was positively impacted by deformation because the sample was initially foliated. Based on our experiments we can only say that foliation is dependent on deformation, which will impact the seismic wave velocity. It would be very interesting to quantify this by measuring the seismic wave velocity through the deformed and undeformed sample.

4.6 Errors and deviations in experiments

The nature of the high pressure and temperature torsion mechanisms is such that numerous repetitions of experiments are not feasible. This makes an estimation of the error margin precarious. However, from the spread of different experiments which are supposed to have an identical initial path we can deduce an approximate margin of error. In these series this boils down to ~10 % of the shear stress excluding experimental aberrations. Including experimental aberrations it can go up to ~30 %.

Chapter 5. Conclusions

The goal of this project was to assess the effects of composition, strain rate and final strain on shear localisation and partial melting. We can summarize the main conclusions point-wise:

1. Melt formation and shear localisation is dependent on chemical composition.

Increased quartz content has a negative impact on localisation and melting. It has a positive impact on the achieved shear stresses (i.e. strength material). Only when muscovite is dominant in mass it determines the behaviour. In this case the strength of the material is lower. The data of the power law exponent n is insufficient to draw conclusions regarding differential micromechanical behaviour of the two compositions. Both samples gave an n value that was in the dislocation creep field. Because the more muscovite-rich rocks are weaker and show more localisation than their quartz-rich counterparts we expect that the strain in natural shear zones will be focused more strongly in the more muscovite-rich rocks. For this reason we expect the muscovite-rich rocks to dictate the overall strength in metapelitic sequences and also the composition of the expelled melt.

2. Melt formation and shear localisation is dependent on strain rate.

The power-law viscous behaviour of the deformation dictates that the samples strained at a higher rate reach higher shear stresses and deform more slowly (i.e. slower localisation). Strain rates impact the morphology of the melt bands. If the rate is higher the bands are more elongate, more connected and less wide. It is yet unclear whether feature has a positive or negative influence on melt migration. The increased presence of new minerals in melt pockets with strain rate is in accordance with the behaviour previously described by Misra *et al.* (2011).

3. Melt formation and shear localisation is strongly dependent on finite strain.

As strain progresses brittle or brittle-ductile processes may be transformed to ductile processes. Also, the amount of glide planes increases with progressive strain. This lowers the strength of the rock by increasing the “ease” of glide. The emergence of more glide planes may be enhanced my melt migration.

4. FIB-SEM: insufficient to determine the 3D structure.

The novel tool of FIB-SEM to establish the 3D structure in melt has proven to be a promising but challenging tool. Significant adjustments are necessary in order to acquire sufficient information. During our analysis too many visibility issues occurred to allow for the visualization of the 3D structure of the melt.

5. Melt migration is dependent on deformation.

Shear deformation has a positive influence on melt migration and segregation on scales of ~100 μm . Melt is higher in area percentage in dynamic experiments than in their static counterparts. Melt is strongly concentrated in shear bands in case of dynamic experiments. This will positively impact overall mobility of the melt, but the degree to which this occurs could not be determined because melt cannot escape the sample assembly. This conclusion is consistent with other authors (Rushmer, 2001; Misra *et al.*, 2009; Tumarkina *et al.*, 2011; Connolly *et al.*, 1997)

6. Experiments and field geology: poor link.

The unrealistically high strain rate and temperature heavily impediments the translation of experimental data to the field in most cases. However, similarities can be found for certain geological settings (1) the partially molten metapelites around the Bushveld intrusion: the temperature, pressure and mineralogy are similar but the tectonic setting is different. And (2) the sheared rocks of Cap de Creus, Spain: the tectonic setting is similar but temperature and strain rate are very different.

Chapter 6. Recommendations and outlook

1. FIB in the Future

In order to improve the quality of the 3D rendering (1) the milling area could be increased, though it is very time-consuming. Or (2) minerals producing stronger contrasts could be used in experiments. The latter requires that minerals differ more in mass from one another.

2. Avoiding experimental failure

Quartz-rich samples have often been proven to be too strong for the jacket: inducing slipping of the jacket rather than deforming the sample. This could perhaps be solved by either increasing the strength of the assembly or decreasing the quartz content (weakening the sample).

3. Closed or open chemical system

TGA analyses have thus far left some uncertainties regarding the release the loss of water during experiments. Reruns of these experiments and analyses will prove key to solve these issues conclusively. The diffusion of metallic ions is very complicated to assert experimentally, but a numerical model may provide conclusive answers.

4. Melt migration

There is still much unknown regarding the exact mechanism of melt migration and the effects of deformation of rocks (Kohlstedt & Holtzman, 2009). This research provided some answers, but they would be more valuable if the melt could “migrate” away from the sample. Thus far attempts to capture the melt have been unsuccessful. Future enquires should focus on this quantification of melt transport.

5. Geological integration

The similarities of the experiments and natural setting could be increased by (1) taking natural rocks (2) decreasing strain rate and (3) lowering temperature. These adjustments however complicate the viability of the experiments. The similarities between the Paterson Rig experiments and Ore Deposit sites (shallow intrusions) are very promising and should be looked into more in the future.

References

- Barnhoorn, a, 2004, The role of recrystallisation on the deformation behaviour of calcite rocks: large strain torsion experiments on Carrara marble: *Journal of Structural Geology*, v. 26, no. 5, p. 885–903.
- Berger, A., and Kalt, A., 1999, Structures and Melt Fractions as Indicators of Rheology in Cordierite-Bearing Migmatites of the Bayerische Wald (Variscan Belt , Germany): v. 40, no. 11, p. 1699–1719.
- Bousquet, R., Oberhansli, R., Goffe, B., Wiederkehr, M., Koller, F., Schmid, S.M., Schuster, R., Engi, M., Berger, a., and Martinotti, G., 2008, Metamorphism of metasediments at the scale of an orogen: a key to the Tertiary geodynamic evolution of the Alps: Geological Society, London, Special Publications, v. 298, no. 1, p. 393–411.
- Connolly, J.A.D., Holness M. B., Rubie, D.C., and Rushmer, T., 1997, Reaction-induced microcracking: An experimental investigation of a mechanism for enhancing anatexis melt extraction: *Geology*, , no. 25, p. 591–594.
- Van Diggelen, E.W.E., De Bresser, J.H.P., Peach, C.J., and Spiers, C.J., 2010, High shear strain behaviour of synthetic muscovite fault gouges under hydrothermal conditions: *Journal of Structural Geology*, v. 32, no. 11, p. 1685–1700.
- Druguet, E., Passchier, C.W., Carreras, J., and Brok, S. Den, 1997, Analysis of a complex high-strain zone at Cap de Creus , Spain: v. 280, p. 31–45.
- Evans, R., Tarits, P., Chave, A., White, a, Heinson, G., Filloux, J., Toh, H., Seama, N., Utada, H., Booker, J., and Unsworth, M., 1999, Asymmetric Electrical Structure in the Mantle Beneath the East Pacific Rise at 17 degrees S.: *Science*, v. 286, no. 5440, p. 752–756.
- Fusseis, F., Handy, M.R., and Schrank, C., 2006, Networking of shear zones at the brittle-to-viscous transition (Cap de Creus, NE Spain): *Journal of Structural Geology*, v. 28, no. 7, p. 1228–1243.
- Gabbott, P., 2008, Principles and Applications of Thermal Analysis: Oxford : Blackwell.

- Holtzman, B.K., Kohlstedt, D.L., and Phipps Morgan, J., 2005, Viscous energy dissipation and strain partitioning in partially molten rocks: *Journal of Petrology*, v. 46, p. 2569–92.
- Johnson, T.I.M.E., Gibson, R.L., Brown, M., Buick, I. a N.S., and Cartwright, I. a N., 2003, Partial Melting of Metapelitic Rocks Beneath the Bushveld Complex , South Africa: *Journal of Petrology*, v. 44, no. 5, p. 301–314.
- Kelley, K. a, and Cottrell, E., 2009, Water and the oxidation state of subduction zone magmas.: *Science*, v. 325, no. 5940, p. 605–607.
- Kohlstedt, D.L., and Holtzman, B.K., 2009, Shearing Melt Out of the Earth: An Experimentalist's Perspective on the Influence of Deformation on Melt Extraction: *Annual Review of Earth and Planetary Sciences*, v. 37, no. 1, p. 561–593.
- Logan, J.M., 2007, The progression from damage to localization of displacement observed in laboratory testing of porous rocks: *Geological Society, London, Special Publications*, v. 289, no. 1, p. 75–87.
- Mahan, K., 2006, Retrograde mica in deep crustal granulites: Implications for crustal seismic anisotropy: *Geophysical Research Letters*, v. 33, no. 24, p. L24301.
- Mcdonnell, R.D., Peach, C.J., and Spiers, C.J., 1999, Flow behavior of fine-grained synthetic dunite in the presence of 0 . 5 wt % H₂O: v. 104, p. 823–845.
- Misra, S., Burg, J.P., and Mainprice, D., 2011, Effect of finite deformation and deformation rate on partial melting and crystallization in metapelites: v. 116, no. July 2010, p. 1–9.
- Misra, S., Burlini, L., and Burg, J.-P., 2009, Strain localization and melt segregation in deforming metapelites: *Physics of the Earth and Planetary Interiors*, v. 177, no. 3-4, p. 173–179.
- Naus-Thijssen, F.M.J., Goupee, A.J., Vel, S.S., and Johnson, S.E., 2011a, The influence of microstructure on seismic wave speed anisotropy in the crust: computational analysis of quartz-muscovite rocks: *Geophysical Journal International*, v. 185, no. 2, p. 609–621.
- Paterson, M.S., and Olgaard, D.L., 2000, Rock deformation tests to large shear strains in torsion: v. 22, p. 1341–1358.

- Reed, S.J.B., 2005, *Electron Microprobe Analysis and Scanning Electron Microscopy in Geology*: Cambridge University Press.
- Rushmer, T., 2001, Volume change during partial melting reactions: implications for melt extraction, melt geochemistry and crustal rheology: *Tectonophysics*, v. 342, no. 3-4, p. 389–405.
- Schmid, S.M., Boland, J.N., and Paterson, M.S., 1977, Superplastic flow in finegrained limestone: v. 43, p. 257–291.
- Stevenson, D.J., 1989, Spontaneous small-scale melt segregation in partial melts undergoing deformation: *Geophysical Research Letters*, v. 16, p. 1067–70.
- Tumarkina, E., 2012, *Role of deformation on partial melting of metapelitic rocks*: ETH Zurich.
- Tumarkina, E., Misra, S., Burlini, L., and Connolly, J. a. D., 2011, An experimental study of the role of shear deformation on partial melting of a synthetic metapelite: *Tectonophysics*, v. 503, no. 1-2, p. 92–99.
- Twiss, R.J., and Moores, E.M., 2007, *Structural Geology*: W. H. Freeman.
- Vielzeuf, D., and Holloway, J.R., 1988, Experimental determination of the fluid-absent melting relations in the pelitic system Consequences for crustal differentiation: , p. 257–276.
- Ward, D., Mahan, K., and Schulte-Pelkum, V., 2012, Roles of quartz and mica in seismic anisotropy of mylonites: *Geophysical Journal International*, v. 190, no. 2, p. 1123–1134.
- Wei, W., Unsworth, M., Jones, a, Booker, J., Tan, H., Nelson, D., Chen, L., Li, S., Solon, K., Bedrosian, P., Jin, S., Deng, M., Ledo, J., Kay, D., *et al.*, 2001, Detection of widespread fluids in the Tibetan crust by magnetotelluric studies.: *Science*, v. 292, no. 5517, p. 716–719.
- De Winter, D.A.M., Lebbink, M.N., De Vries, D.F.W., Post, J.A., and Drury, M.R., 2011, FIB-SEM cathodoluminescence tomography: practical and theoretical considerations.: *Journal of Microscopy*, v. 243, no. 3, p. 315–326.

De Winter, D.A.M., Schneijdenberg, C.T.W.M., Lebbink, M.N., Lich, B., Verkleij, A.J., Drury, M.R., and Humbel, B.M., 2009, Tomography of insulating biological and geological materials using focused ion beam (FIB) sectioning and low-kV BSE imaging.: *Journal of Microscopy*, v. 233, no. 3, p. 372–383.

Zhu, W., Gaetani, G.A., Fuisseis, F., Montési, L.G., and De Carlo, F., 2011, Microtomography of Partially Molten Rocks: Three-Dimensional Melt Distribution in Mantle Peridotite: *Science*, v. 332, no. 6025, p. 88–91.

Acknowledgements

I would like to thank my supervisors Santanu, Chris and Karsten very much for their support, critical questions and helpful insights. It helped me develop myself scientifically and encouraged my passion for research.

I would also like to thank Bjarne Almqvist for providing me with interesting new ideas, Evangelis Moulos for the help with the Microprobe and Richard Bakker for helping me with the method details.

Also I would like to thank Lydia Zender for the help with the XRD and the development of my German skills to a new level, and Christian Mensing for the TGA analyses. I would like to thank Robert Hoffman for the technical support in the Rock Deformation Lab. I am grateful to Prof. J.P. Burg for accommodating me in his structural geology group at the ETH.

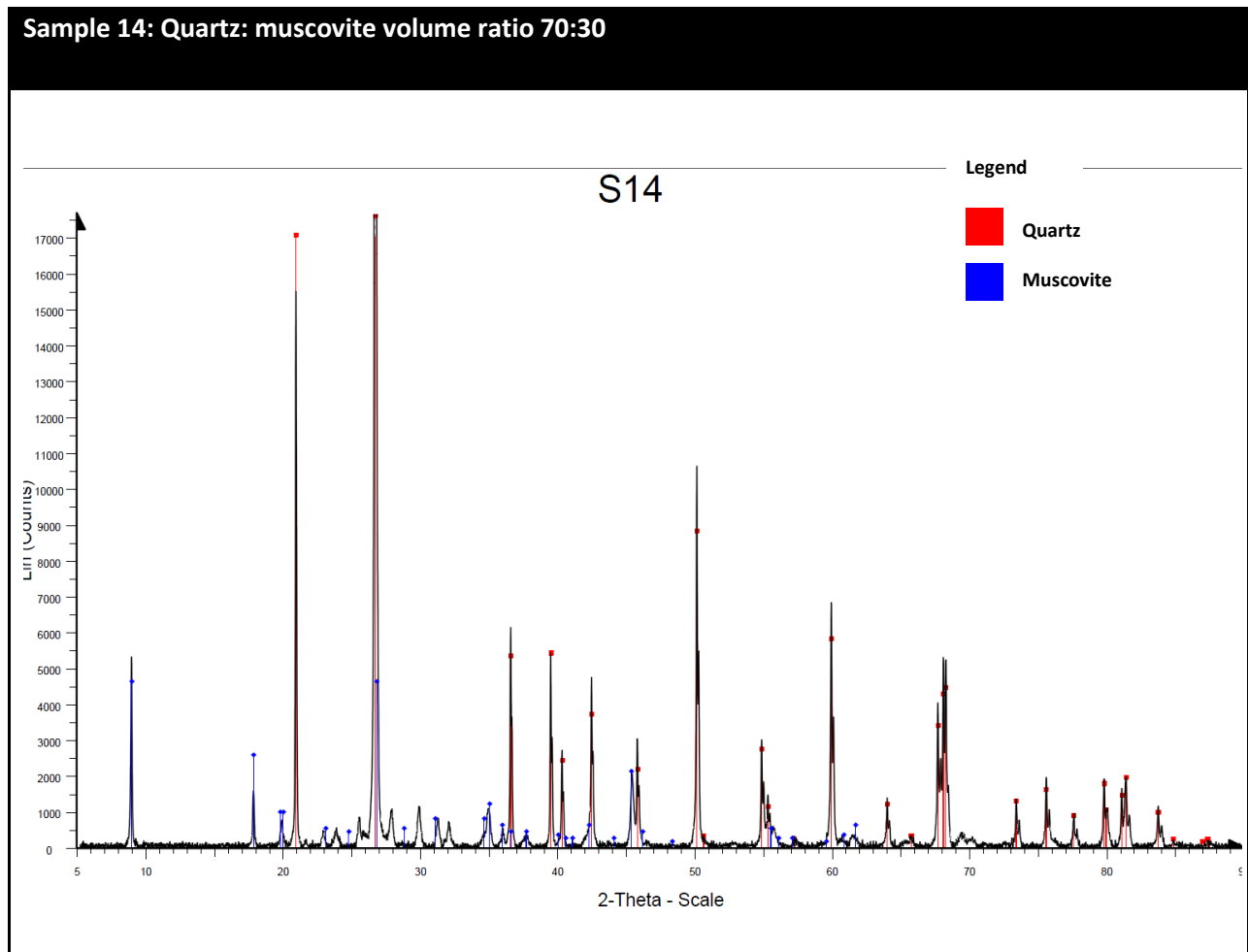
Thanks to Ingrid Okanta, Sigrid Tindler, Andrea Rothenbuhler at the ETH for their support in the administrative maze, and at the University of Utrecht thanks to Ingrid Beekman and Arman Kliet for their help.

I could not have done it without my friends and fellow thesis-writers. Aike, Marloes and Maartje for the best days of writing, Martijn and Elke for your useful insights and support. Thanks to Wouter, Esther and Demetri for those moments of glory in the Utrecht University Library. In Zurich Edine, Anna, Giulia, Vivian, Verena, Sabrina, Michele, Luca, Usman and Thomas, for the tea, the coffee and the fun. Thanks to my flat mates in Utrecht, for their voluntary and involuntary advice and the best sandwiches a girl could survive on: Henrik, Timo, Tanly, Fred, Heleen, Jasmijn, Jesse, Ayla, Koen, Noor and Daan. Thanks to my family, my loving siblings, Nicolaas, Gemma, Cathelijne, my parents and my grandmothers. My mother in particular for supporting me with all my choices. Most of all Leon, thank you for supporting me in everything and helping me make big life decisions.

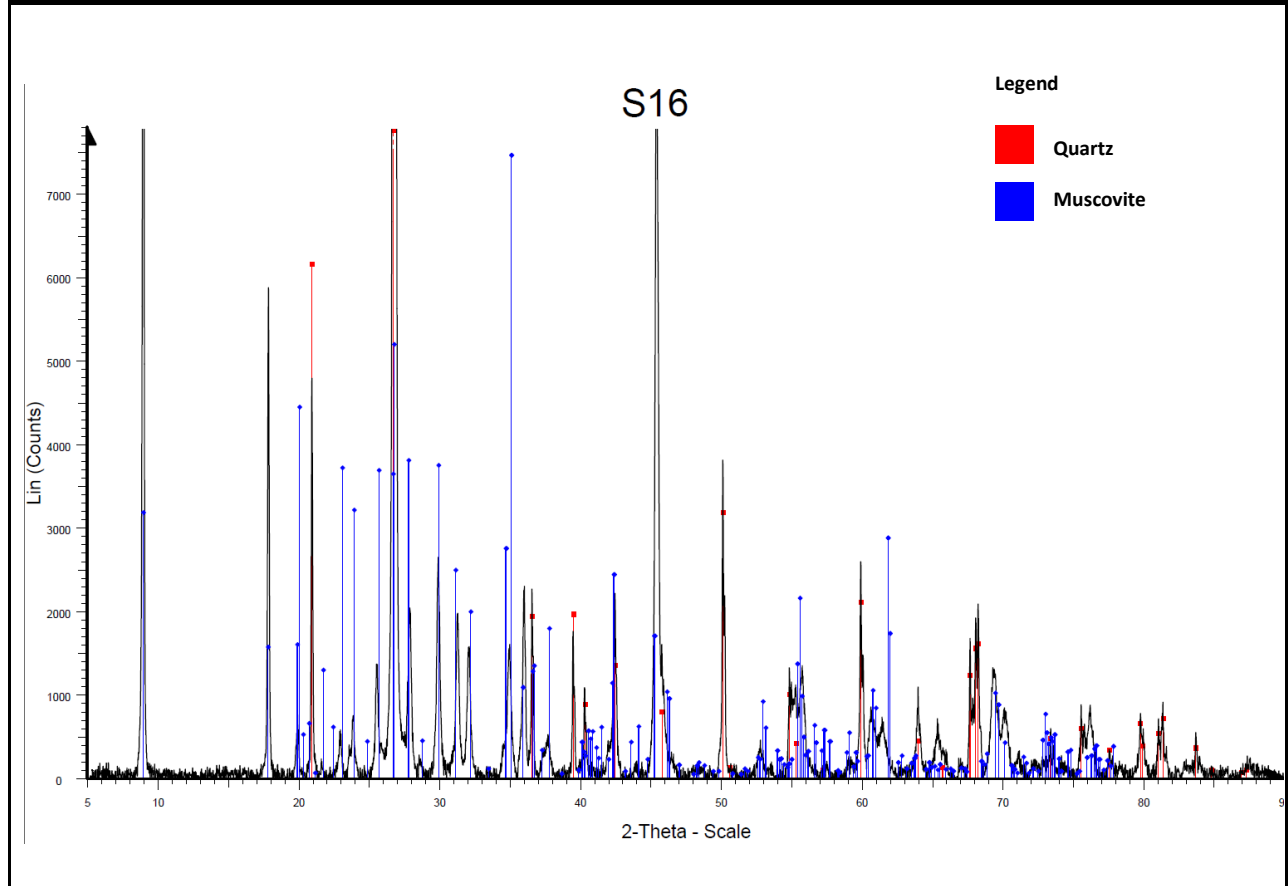
My stay at ETH has been supported by an Erasmus Placement Scholarship.

Appendix A XRD plots

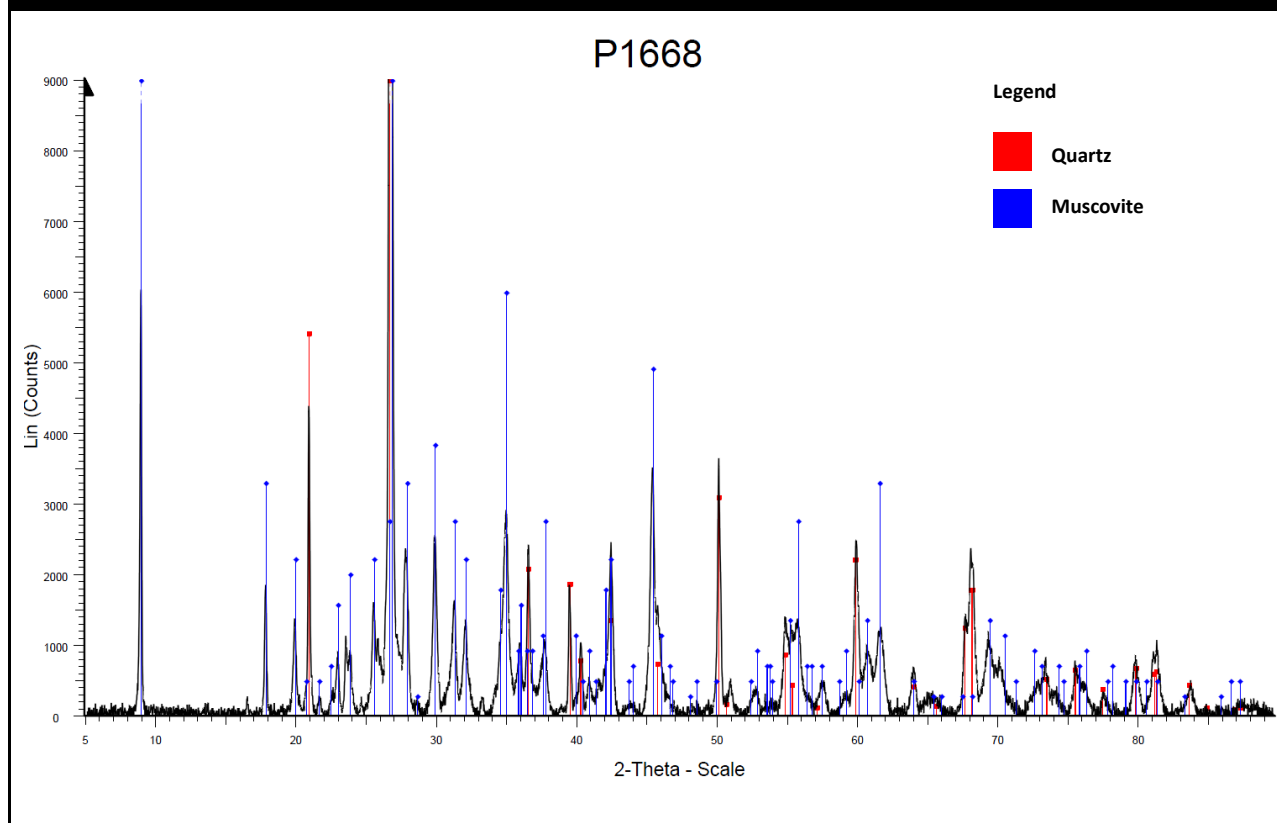
This appendix contains the XRD plots obtained from the undeformed and deformed samples.



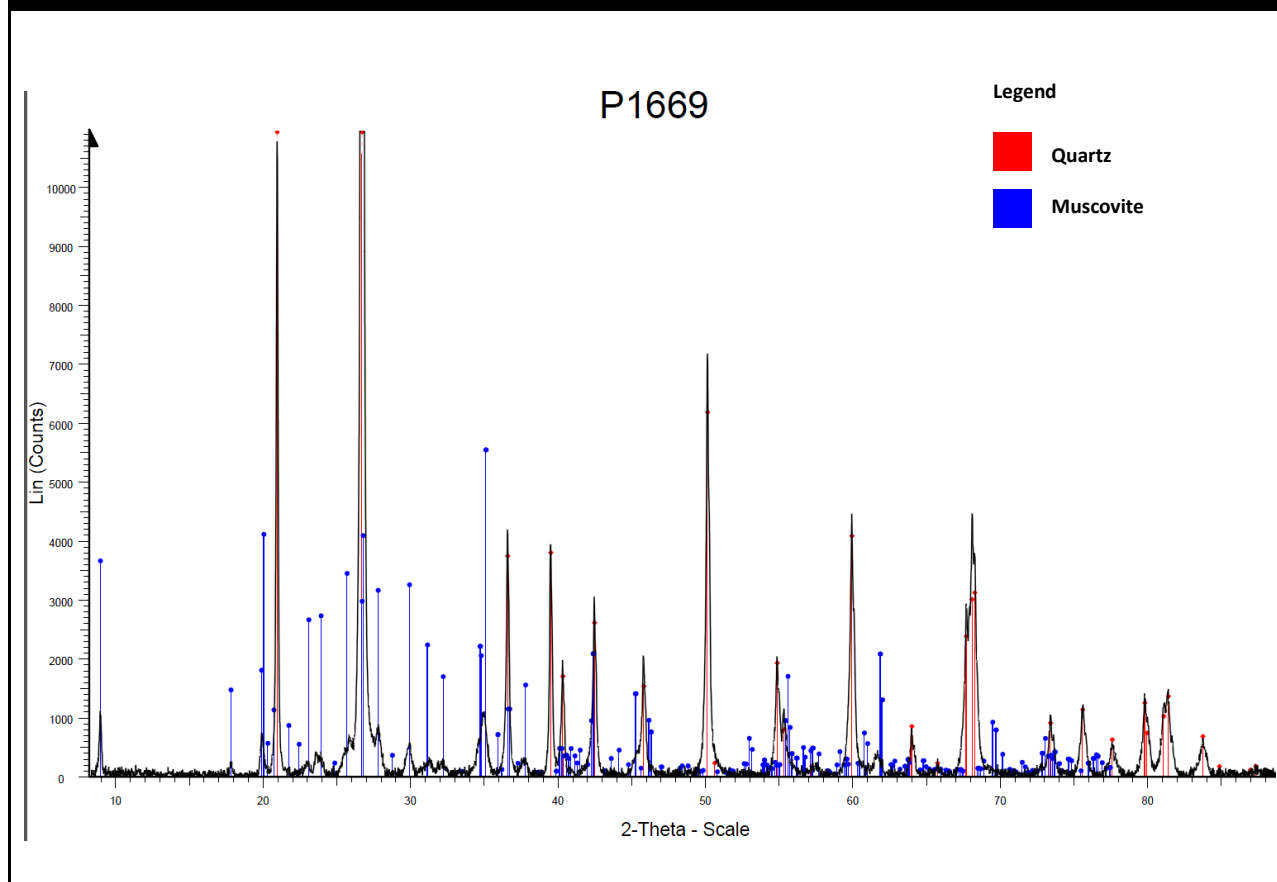
Sample 16: Quartz: muscovite volume ratio 30:70



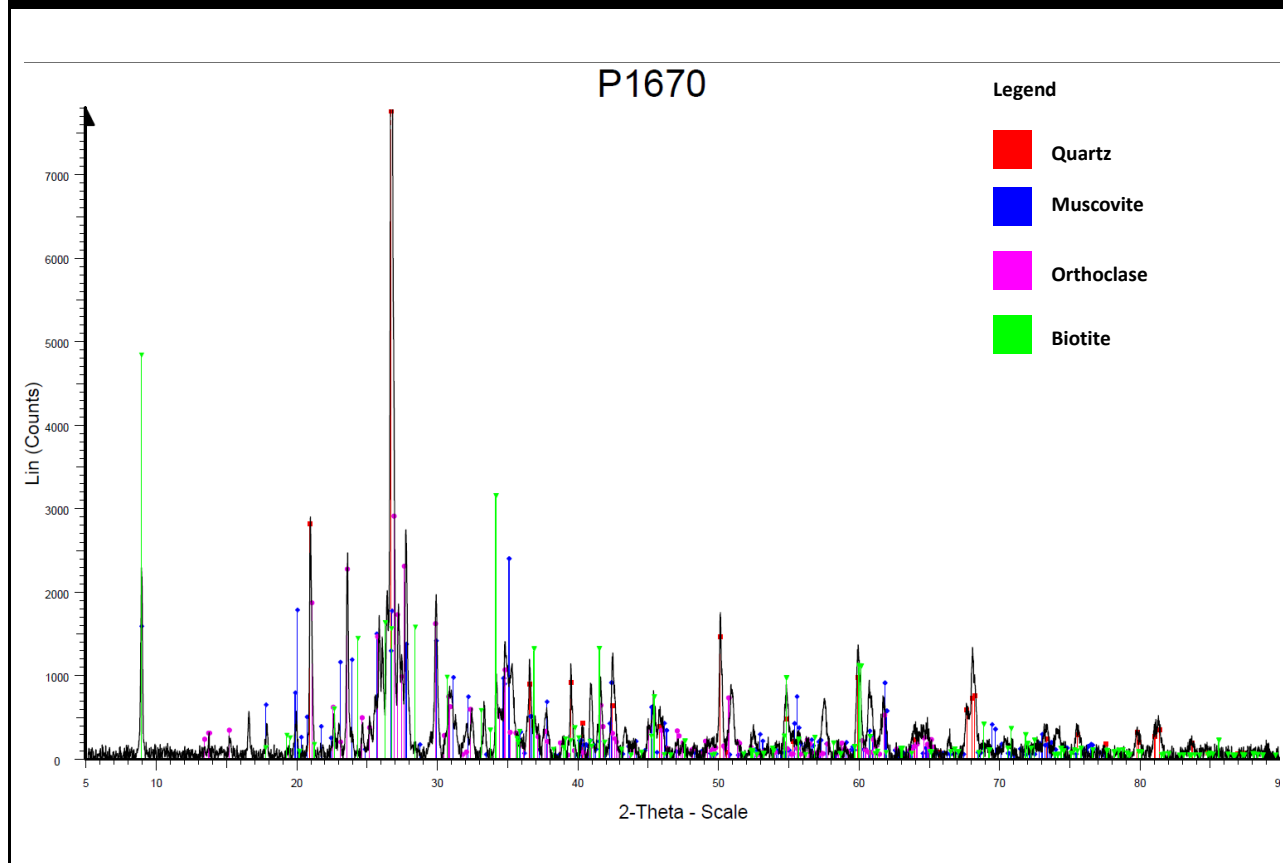
Sample P1668 : Quartz: muscovite volume ratio 70:30



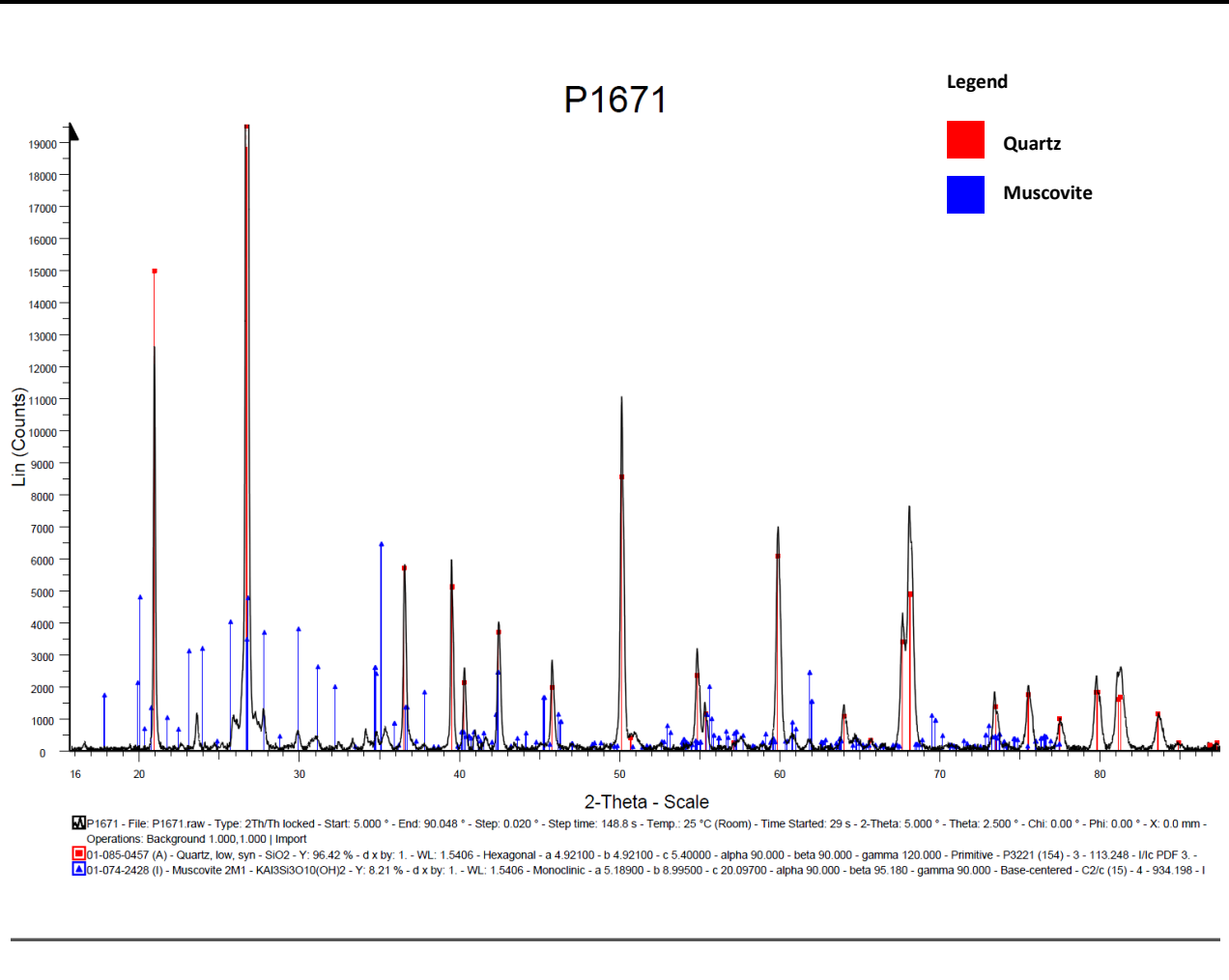
Sample P1669 : Quartz: muscovite volume ratio 30:70 (based on sample 14)



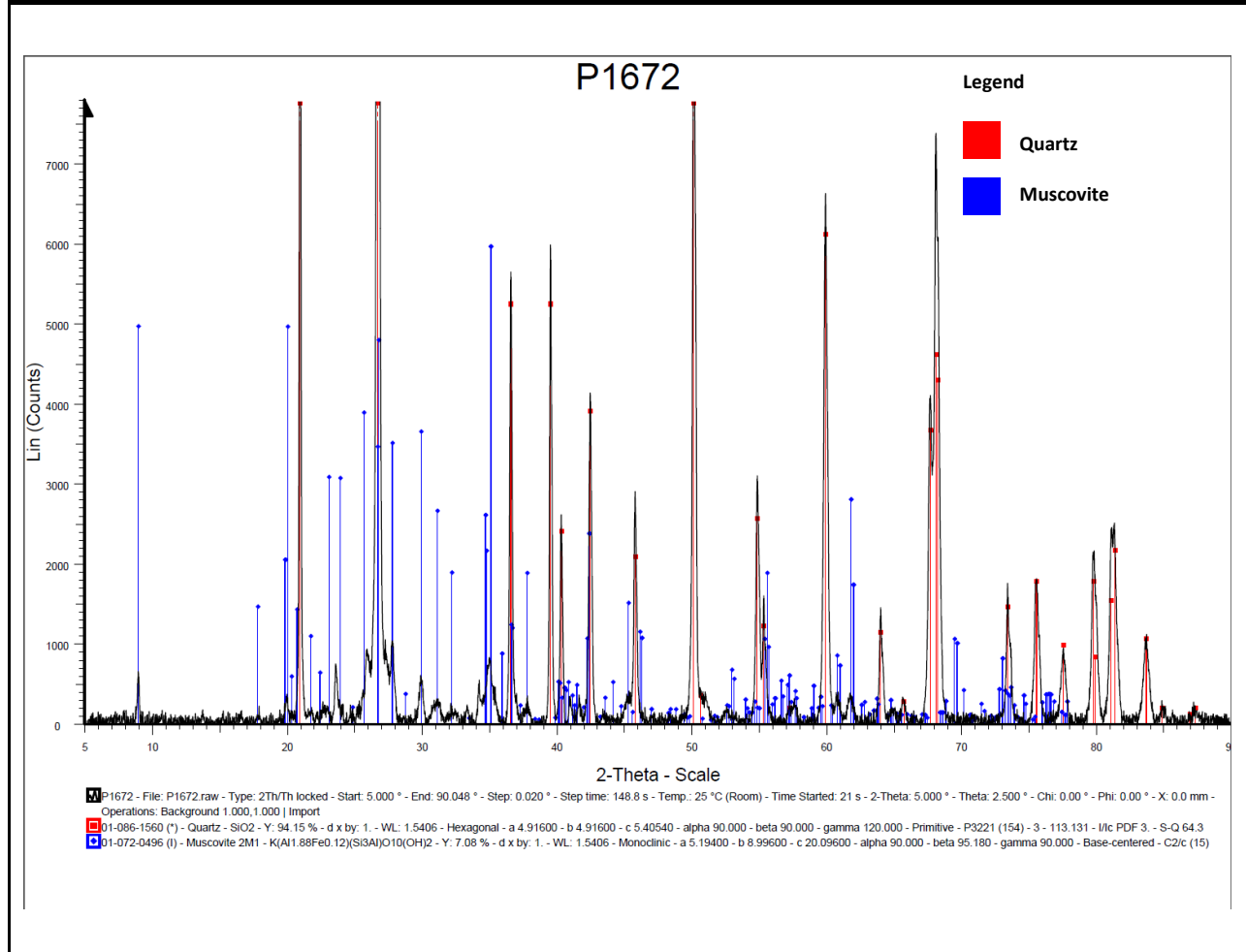
Sample P1670 : Quartz: muscovite volume ratio 70:30 (based on sample 16)



Sample P1671 : Quartz: muscovite volume ratio 30:70 (based on sample 14)



Sample P1672 : Quartz: muscovite volume ratio 30:70 (based on sample 14)



Appendix B FIB-SEM

Please see attached video on the USB attached to this thesis

Appendix C Stepping Strain Rate (SSR) Experiments

C.1 SSR of Sample 14 Quartz:Muscovite 70:30

C.1.1 Experiment P1669

Experiment P1669 $\gamma \sim 1$

| Strain Rate (1/s) | Internal Torque uncorrected | Torque Corrected for zero Torque (12.68) | In (Corrected Internal Torque) | In (shear strain rate) |
|-------------------|-----------------------------|--|--------------------------------|------------------------|
| 7.00E-05 | 37.4 | 24.72 | 3.207612633 | -9.567015316 |
| 1.00E-04 | 38.4 | 25.72 | 3.247268899 | -9.210340372 |
| 3.00E-04 | 42.3 | 29.62 | 3.388449809 | -8.111728083 |
| 5.00E-04 | 42.8 | 30.12 | 3.405189403 | -7.60090246 |

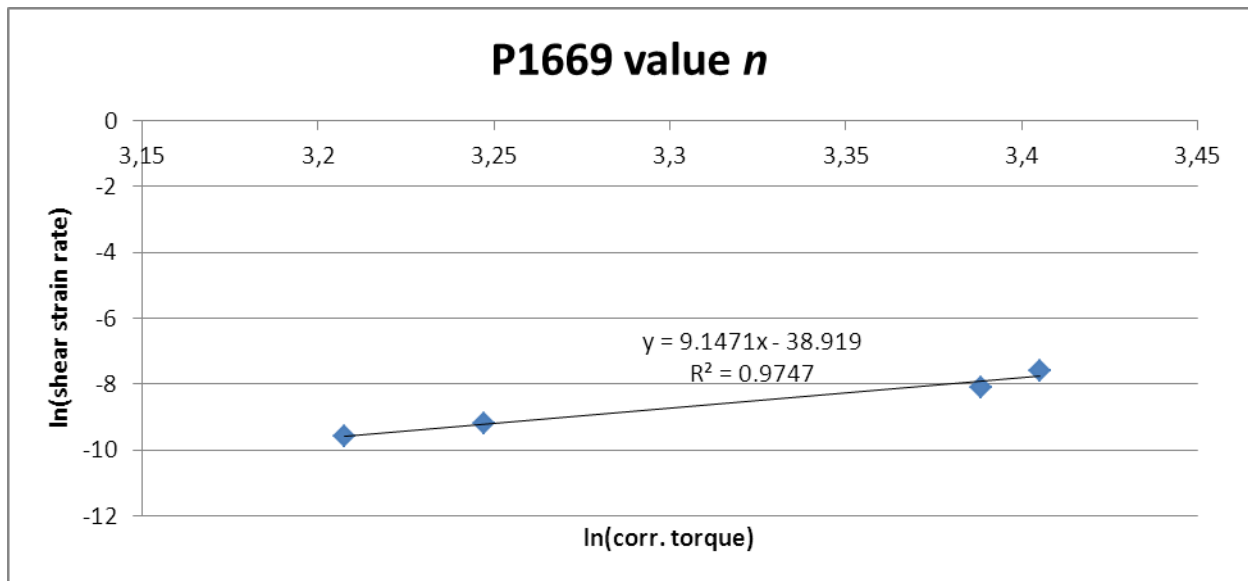


Figure C.3 Graph representing data for n value experiment P1669

C.1.2 Experiment P1671

Experiment P1671 $\gamma \sim 3$

| Strain Rate (1/s) | Internal Torque uncorrected | Torque Corrected for zero Torque (18.09) | In (Corrected Internal Torque) | In (shear strain rate) |
|-------------------|-----------------------------|--|--------------------------------|------------------------|
| 0.00007 | 22.6 | 4.51 | 1.506297154 | -9.567015316 |
| 0.0001 | 23.4 | 5.31 | 1.669591835 | -9.210340372 |
| 0.0003 | 25.8 | 7.71 | 2.042518188 | -8.111728083 |
| 0.0005 | 27.4 | 9.31 | 2.231089091 | -7.60090246 |
| 0.0007 | 27.4 | 9.31 | 2.231089091 | -7.264430223 |

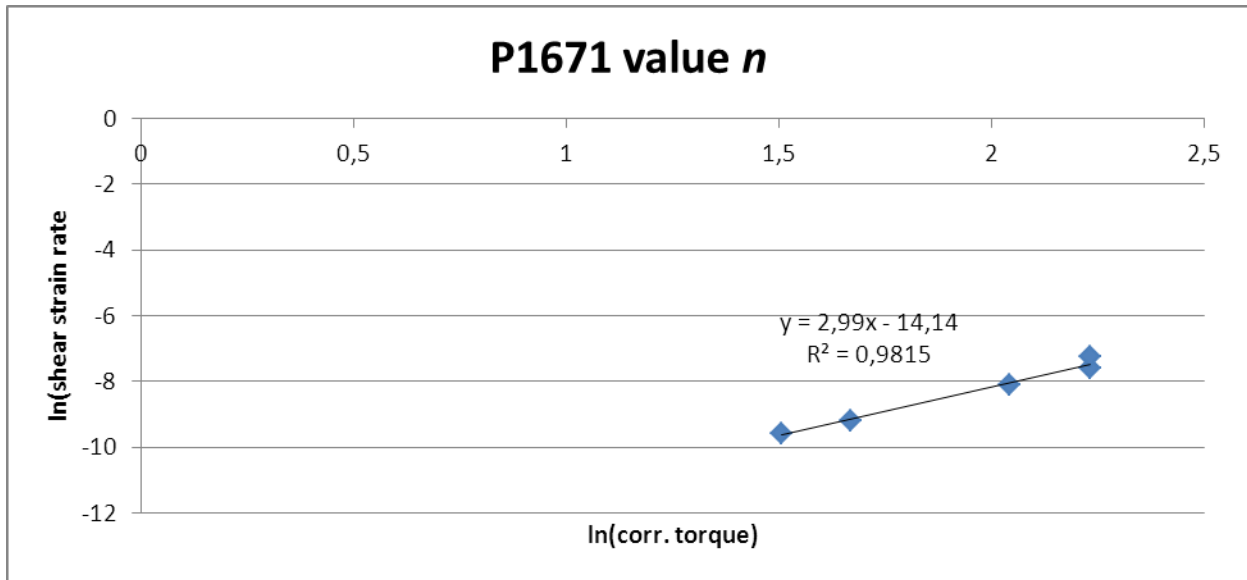


Figure C.4 Graph representing data for n value experiment P1671

C.1.2 Experiment P1672

Experiment P1672 $\gamma \sim 3$

| Strain Rate (1/s) | Internal Torque uncorrected | Torque Corrected for zero (19.40) | \ln (Corrected Internal Torque) | \ln (shear strain rate) |
|-------------------|-----------------------------|-----------------------------------|-----------------------------------|---------------------------|
| 5.00E-05 | 23 | 3.6 | 1.280933845 | -9.903487553 |
| 7.00E-05 | 24.7 | 5.3 | 1.667706821 | -9.567015316 |
| 1.00E-04 | 26.9 | 7.5 | 2.014903021 | -9.210340372 |
| 3.00E-04 | 31.9 | 12.5 | 2.525728644 | -8.111728083 |

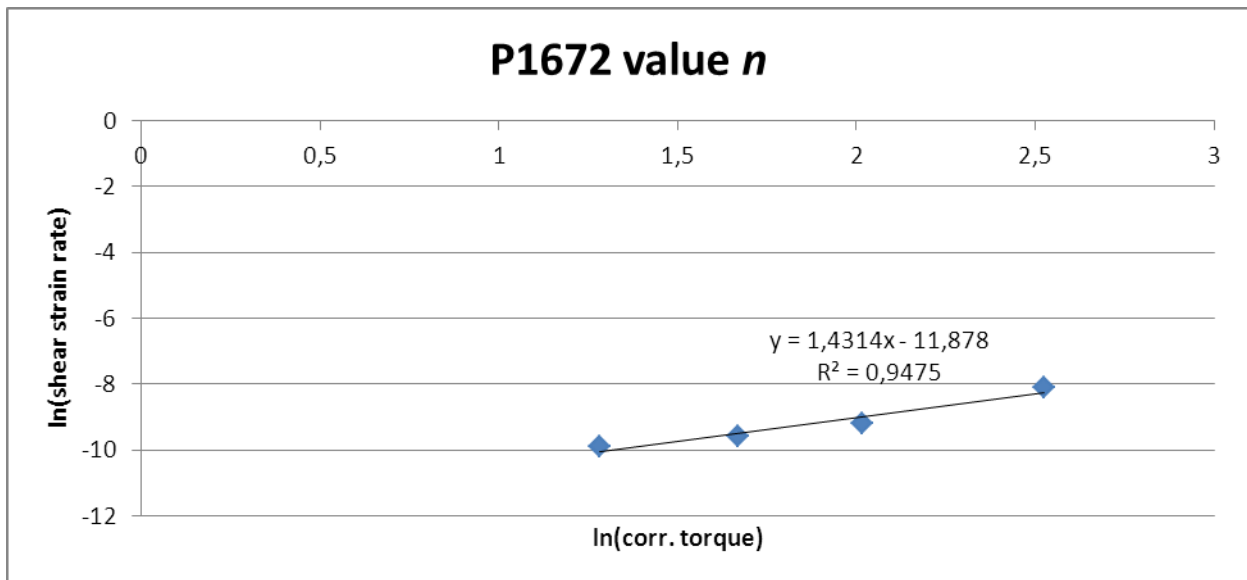


Figure C.5 Graph representing data for n value experiment P1672

C.2 SSR of Sample 16 Quartz:Muscovite 30:70

C.2.1 Experiment P1668

Experiment P1668 $\gamma \sim 1$

| Strain Rate (1/s) | Internal Torque uncorrected | Torque | Corrected for zero Torque (12.3) | In (Corrected Internal Torque) | In (shear strain rate) |
|-------------------|-----------------------------|--------|----------------------------------|--------------------------------|------------------------|
| 5.00E-05 | 13.8 | | 1.5 | 0.405465108 | -9.903487553 |
| 1.00E-04 | 14.3 | | 2 | 0.693147181 | -9.210340372 |
| 3.00E-04 | 18 | | 5.7 | 1.740466175 | -8.111728083 |

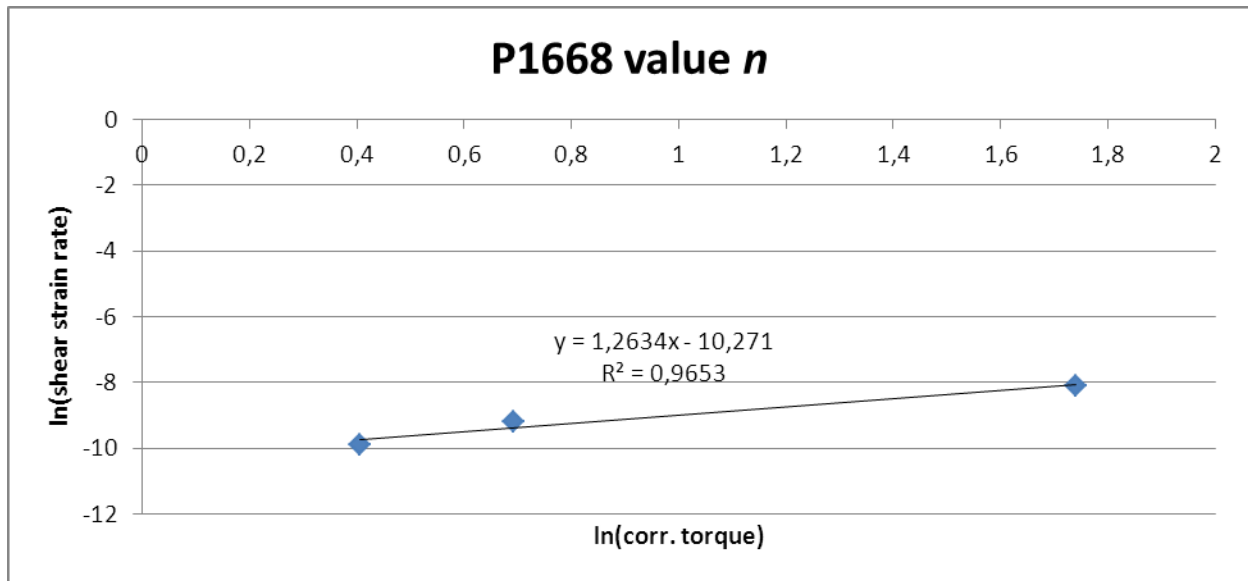


Figure C.6 Graph representing data for n value experiment P1668

C.2.2 Experiment P1670

Experiment P1670 $\gamma \sim 3$

| Strain Rate (1/s) | Internal Torque uncorrected | Torque | Corrected for zero Torque (12.9) | In (Corrected Internal Torque) | In (shear strain rate) |
|-------------------|-----------------------------|--------|----------------------------------|--------------------------------|------------------------|
| 0.0001 | 14.1 | | 1.2 | 0.182321557 | -9.210340372 |
| 0.0003 | 14.3 | | 1.4 | 0.336472237 | -8.111728083 |
| 0.0005 | 14.6 | | 1.7 | 0.530628251 | -7.60090246 |
| 0.0007 | 14.7 | | 1.8 | 0.587786665 | -7.264430223 |

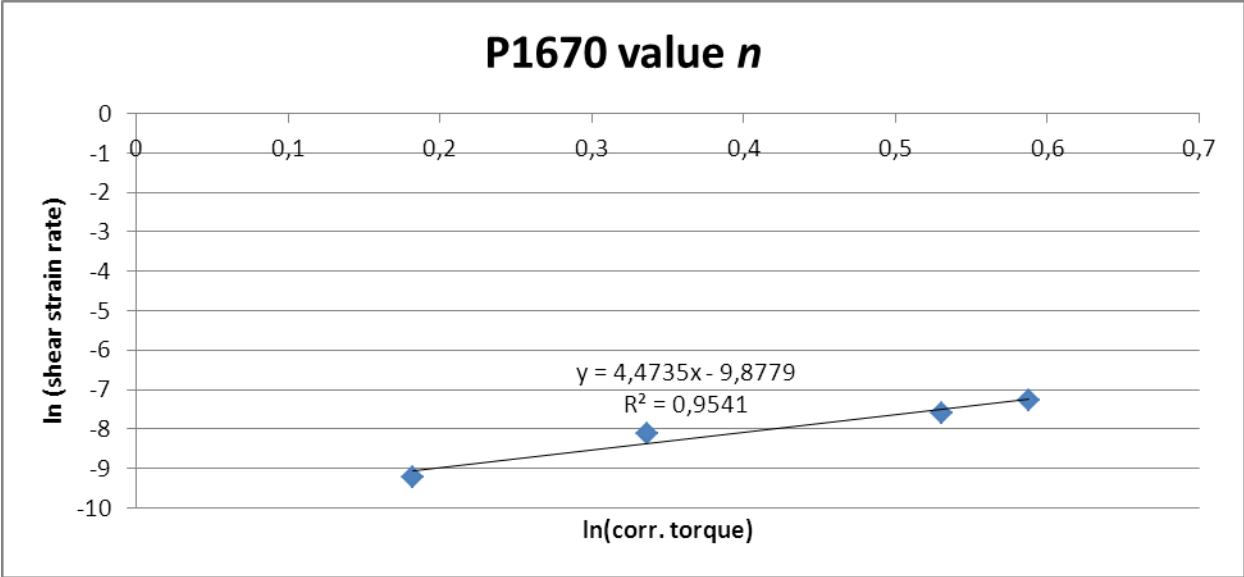


Figure C.7 Graph representing data for n value experiment P1670

Appendix D Microprobe

In this appendix the data of the analyses of the line measurements (D.1, D.2) and melt measurements (D.3) are given.

D.1 Quartz-rich, high strain rate high finite strain (P1672)

In this sample highly deformed bands with crushed grains and intergranular melt were visualized with SEM. The melt layers were too small to measure as a point measurement with the probe beam and therefore a line transect through a “melt” band was taken. The step size of the transect through the shear bands is 2 μm . A representative image of such a band is displayed in Figure 3.4. The subsequent oxide percentage signal is visible in Figure 3.5. This displays a pattern of different minerals and melt. Because these units are smaller than the beam size it is not possible to distinguish any further. There is an inverse correlation between the SiO_2 and Al_2O_3 content but it cannot be determined whether this is due to muscovite or melt. Low totals and higher Al_2O_3 content point to aluminosilicates as the EMPA does not measure water content. Higher totals and high SiO_2 point to quartz grains. Overall no unique phase was distinguishable due to the beam size.

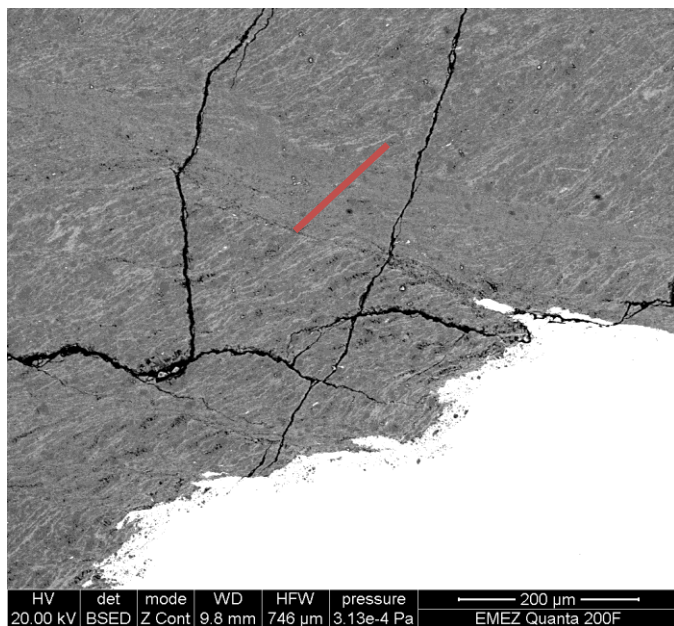


Figure D.1 Representative image of P1672 in SEM BSE. The red line indicates a representative line for a transect done by the EMPA. Light grey refers to muscovite, dark gray to quartz and the randomly orientated black fractures are filled by glue resin. The white is part of the plastic capsule the sample was a part of.

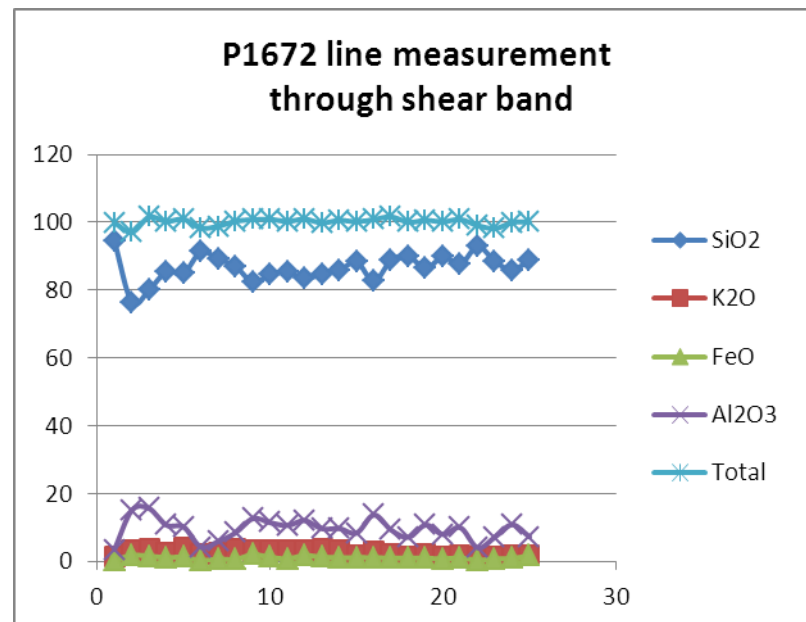


Figure D.2 P1672 line measurement through wide shear band in P1672. Due to the beam size of 2 μm the measurements generally do not represent one phase. It is visible that quartz, muscovite and a possible intermediate alternate.

D.2 Muscovite-rich, high strain rate, high finite strain (P1129)

From SEM imaging it became clear that the shear bands are considerably thinner than P1670, hence causing resolution problems with the 2 μm beam size of the electron microprobe. Therefore line measurements were taken analogous to P1672. The data in Figure 3.17 shows that there are different phases but the points are not distinct enough to be able to conclude something about melt composition.

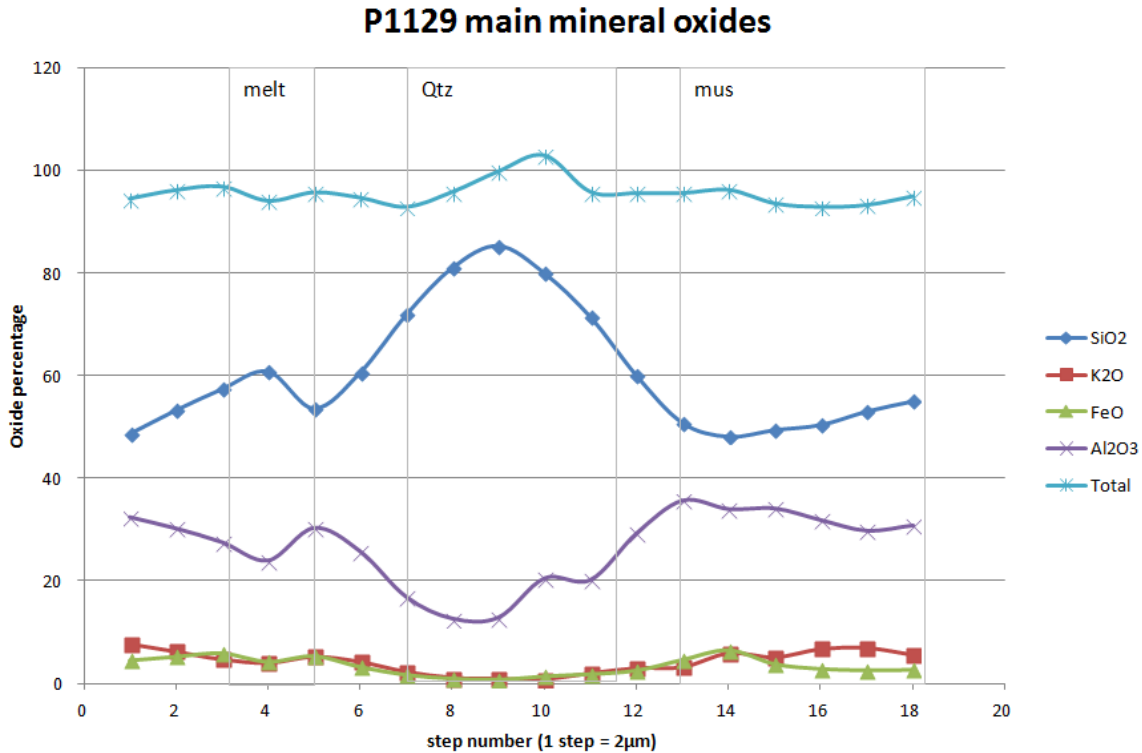


Figure D.3 P1129 main mineral oxides line transect.

D.3 Melt measurements Microprobe

| | 1,00 | 2,00 | 3,00 | 4,00 | 5,00 | 6,00 | 7,00 | 8,00 | 9,00 | 10,00 | |
|------------------|-----------------|-----------------|-----------------|------------------|------------------|------------------|------------------|------------------|------------------|------------------|--------------------|
| | P1670_1 Melt | P1670_2 Melt | P1670_9 Melt | P1670_11 Melt | P1670_12 Melt | P1670_13 Melt | P1670_14 Melt | P1670_15 Melt | P1670_18 Melt | P1670_19 Melt | Average Mus |
| X | 0,68 | 0,68 | 0,69 | 0,70 | 0,73 | 0,65 | 0,70 | 0,69 | 0,72 | 0,63 | 0,69 |
| Y | 0,22 | 0,21 | 0,19 | 0,19 | 0,16 | 0,28 | 0,20 | 0,20 | 0,18 | 0,29 | 0,14 |
| Z | 0,10 | 0,11 | 0,12 | 0,11 | 0,11 | 0,08 | 0,10 | 0,11 | 0,10 | 0,09 | 0,17 |
| SUM | 1,00 | 1,00 | 1,00 | 1,00 | 1,00 | 1,00 | 1,00 | 1,00 | 1,00 | 1,00 | 1,00 |
| X(Norm%) | 67,97 | 68,08 | 69,43 | 69,62 | 73,30 | 64,79 | 70,27 | 68,97 | 72,07 | 62,73 | 68,60 |
| Y(Norm%) | 21,92 | 21,08 | 18,85 | 19,17 | 15,79 | 27,64 | 19,60 | 19,97 | 18,01 | 28,70 | 14,43 |
| Z(Norm%) | 10,11 | 10,83 | 11,72 | 11,22 | 10,91 | 7,57 | 10,13 | 11,06 | 9,93 | 8,57 | 16,96 |
| SUM100 | 100,00 | 100,00 | 100,00 | 100,00 | 100,00 | 100,00 | 100,00 | 100,00 | 100,00 | 100,00 | 100,00 |
| H: | 58,86 | 58,96 | 60,13 | 60,29 | 63,48 | 56,11 | 60,86 | 59,73 | 62,41 | 54,33 | 59,41 |
| Z (Horiz) | 44,10 | 44,88 | 46,43 | 46,03 | 47,56 | 39,96 | 45,27 | 45,55 | 45,96 | 39,93 | 51,26 |

Table D.2.1 Point measurements melt pockets, X, Y and Z stand for Al₂O₃, K₂O and FeO₂. Values have been corrected for molar proportions.

